Astronomy Unit

Department of Physics and Astronomy

Queen Mary University of London

The study of main-sequence star super-flare frequency, peculiar super-flares and empirical relations between stellar activity and rotation periods

Ahdab Khalid Althukair

August 2023

Supervised by David Tsiklauri and David Burgess

Submitted in partial fulfillment of the requirements of the Degree of Doctor of Philosophy

Declaration

I, Ahdab Khalid Althukair, confirm that the research included within this thesis is my own work or that where it has been carried out in collaboration with, or supported by others, that this is duly acknowledged below and my contribution indicated. Previously published material is also acknowledged below.

I attest that I have exercised reasonable care to ensure that the work is original, and does not to the best of my knowledge break any UK law, infringe any third party's copyright or other Intellectual Property Right, or contain any confidential material.

I accept that the College has the right to use plagiarism detection software to check the electronic version of the thesis.

I confirm that this thesis has not been previously submitted for the award of a degree by this or any other university. The copyright of this thesis rests with the author and no quotation from it or information derived from it may be published without the prior written consent of the author.

Signature: Ahdab Khalid Althukair
Date: 01/08/2023

Publications

The work presented in this thesis is based on the following peer-reviewed journal articles.

A refereed journal paper which has been published:

- Althukair, A.K., Tsiklauri, D. 2023, *Main-sequence star super-flare frequency based on entire Kepler data*, Res. Astron. Astrophys, Volume 23, 085017, doi: 10.1088/1674-4527/acdc09

- Althukair, A.K., Tsiklauri, D. 2023, *New Cases of Super-flares on Slowly Rotating Solar-type Stars and Large Amplitude Super-flares in G- and M-type Main-sequence Stars*, Res. Astron. Astrophys, Volume 23, 105010, doi: 10.1088/1674-4527/acee51

- Althukair, A.K., Tsiklauri, D. 2023, *Prediction of Short Stellar Activity Cycles using Derived and Established Empirical Relations between Activity and Rotation Periods*, Res. Astron. Astrophys, Volume 23, 115015, doi: 10.1088/1674-4527/acf6b2

The research and findings provided in this thesis have been presented at the following meetings and conferences:

- Royal Astronomical Society Specialist Discussion Meeting 2019 (Talk).

- Royal Astronomical Society Specialist Discussion Meeting 2023 (Poster).

- Royal Astronomical Society National Astronomy Meeting 2023 (Poster).

Abstract

Stellar flares are unpredictable, explosive phenomena defined as sudden, intense brightening on the surface of a star caused by the release of magnetic energy during the reconnection of twisted magnetic fields in the outer atmospheres of stars. During a stellar flare, a sizable fraction of the energy is released as electromagnetic radiation with a wide range of wavelengths, from radio waves to gamma rays. The observations of the brightness increase across different wavelengths, especially in X-rays and UV, are frequently used to detect stellar flares. Most flares are observed on young, active stars or magnetically active stars like our Sun. Stellar flares have a significant impact on the environment, including the planetary system of the star. Additionally, flares can cause disturbances in the star's magnetic field, leading to stellar storms and coronal mass ejections that may adversely affect life on nearby planets. Studying stellar flares helps us understand magnetic fields, stellar activity, and the interaction of stars and their planetary systems.

This thesis provides observations and statistical analysis of stellar flares found by an automated flare detection Python script, written for this purpose, that was used to search for super-flares on main sequence stars of types A, F, G, K, and M based on the entire Kepler's long-cadence data. 4637 super-flares on 1896 G-type dwarfs were found, and it was determined that a super-flare on G-type dwarfs of energy of 10^{35} erg occurs on a star once every 4360 years. Furthermore, 321, 1125, 4538 and 5445 super-flares were found on 136, 522, 770 and 312 dwarfs of types A, F, K and M, respectively. Moreover, the statistical properties of the occurrence rate of super-flares were studied and confirmed that the occurrence rate (dN/dE) of super-flares versus flare energy, E, follows a power-law distribution with $dN/dE \propto E^{-\alpha}$, where $\alpha \simeq 2.0$ to 2.1 for the spectral types ranging from F-type to M-type stars. However, for A-type stars, the value of α is approximately 1.3. This indicates that A-type stars' flare conditions differ from those of other spectral types.

In addition, the thesis presents new results of the occurrences of super-flares on slowly rotating Sun-like stars with rotation periods ranging from 24.5 to 44 days. This finding further supports previous, controversial results that the Sun may experience a surprise super-flare. Furthermore, the thesis describes newly found unusually large amplitude super-flares detected on G- and M-type main-sequence stars. A preliminary examination of these cases was provided, and the link between e-folding decay time, τ vs flare amplitude and flare energy was studied. The results show that for Sun-like stars with a slow rotation period, low τ values are associated with high flare energies, and high τ values are

associated with low flare energies. Similarly, τ is large for small flare amplitudes and τ is small for large amplitudes considered. However, there is no clear relation between these parameters for large amplitude super-flares in the main sequence G- and M-type stars, as we could not establish clear functional dependence between the parameters.

Previous studies have revealed short activity cycles in F-type and G-type stars, and the question investigated was whether or not short-term activity cycles are a common phenomenon in these stars. Also, extensive studies establish an empirical connection between a star's activity cycle and rotation periods. Therefore, 138 Kepler IDs of F and G types main sequence stars with rotation periods less than a day ($P_{\mathrm{rot}} < 1$ d) were collected using Kepler data and Gaia parameters to derive, as well as use plausible, established empirical relations between P_{cyc} and P_{rot} to provide predictions for very short $5.09 \leq P_{\mathrm{cyc}} \leq 38.46$ d cases in a tabular form. Also, an alternative method for measuring very short P_{cyc}, using flare-detection algorithms applied to future space mission data has been proposed.

Acknowledgements

First of all, I would like to express my sincere thanks and gratitude to my primary supervisor and mentor, Dr David Tsiklauri, for his guidance, motivation, continued support and overall assistance during the course of my doctoral studies and writing this thesis.

I would also like to thank Dr. David Burgess, my current supervisor, for his assistance and continued support.

Also, I would like to express my appreciation and gratitude to my dear husband, who spared no effort in helping, supporting and encouraging me during my PhD study.

I am also grateful to my wonderful family, my dear parents, my brothers and my sister for their endless support while writing this thesis and in my life in general.

List of Figures

List of Figures

List of Tables

Contents

Contents

1 Introduction

Investigating the Sun and other celestial bodies, especially stars, carries immense significance in advancing our understanding of the universe. The Sun, the nearest star to our planet, presents a distinctive prospect for conducting research in the field of solar physics and gaining insights into the fundamental processes and mechanisms that govern stars (Curto, 2020). Studying the Sun allows scientists to explore various aspects of solar physics, including solar structure, activity, and energy production. Moreover, it enables scientists to investigate various solar phenomena that can profoundly impact space weather, such as solar flares, coronal mass ejections, and solar wind (Abed et al., 2021). However, investigating other stars goes beyond the limitations of studying just one star. It enables a more comprehensive investigation of stellar phenomena such as nuclear fusion, stellar dynamics, and the interaction of magnetic fields, radiation, and gravity.

1.1 The Sun

The Sun is a G-type main-sequence star that was formed roughly 4.6 billion years ago (Bonanno et al., 2002; Connelly et al., 2012), when a cloud of dust and gas collapsed, causing matter to condense into a blazing ball of gas. The nuclear fusion reactions at its core produce an incandescent ball of hot plasma. This energy is emitted by the Sun primarily as visible light, ultraviolet, and infrared radiation (Bhatia, 2014). It has a surface temperature of $T_{\text{eff}} = 5778$ K, a radius of $R_\odot = 6.960 \times 10^8$ m and a mass of $M_\odot = 1.989 \times 10^{30}$ kg (Severino, 2017). Approximately 73% of the Sun's mass is composed of hydrogen, with the remainder primarily consisting of helium 25% and 2% heavier elements such as oxygen, carbon, neon, and iron (Basu & Antia, 2008). The Sun can be categorized into two primary domains, namely the solar interior and the solar atmosphere.

1.1.1 The Solar Interior

The solar interior is divided into four distinct regions due to the various processes that occur there, namely the core, the radiative zone, the tachocline, and the convection zone.

Figure 1.1 shows the sun's interior, depicting these layers and their corresponding densities and temperatures.
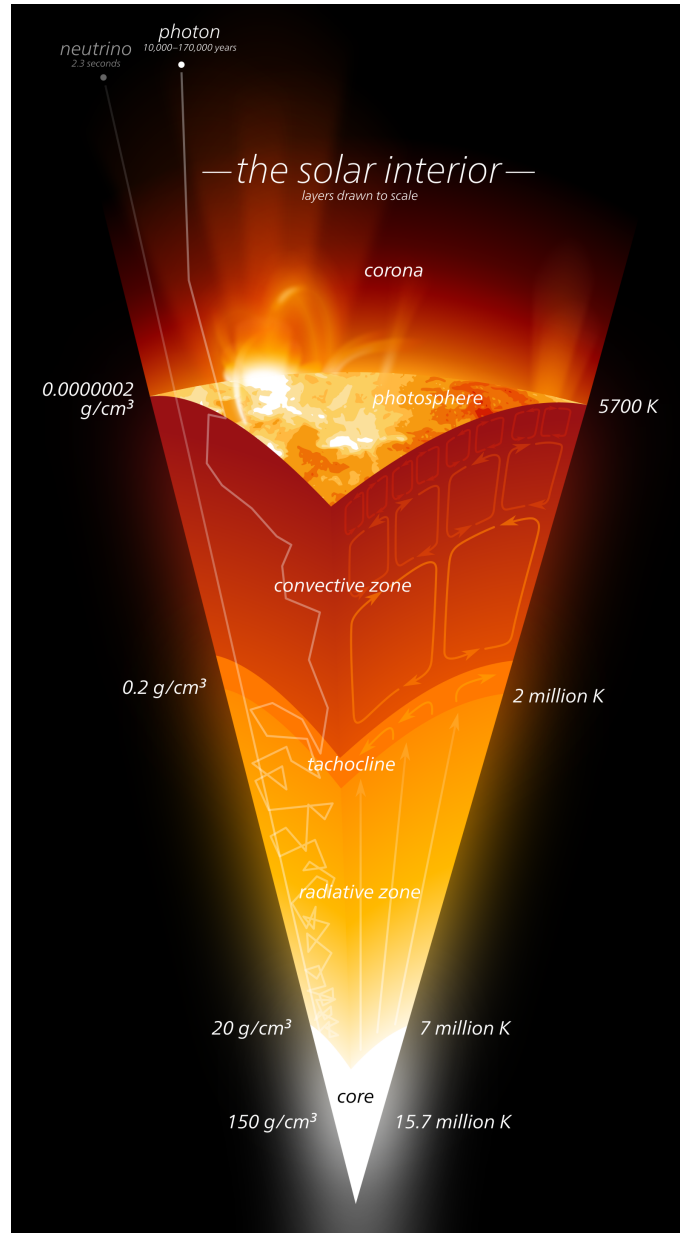
Figure 1.1: A schematic showing the solar interior. On the left are the densities of the different layers, and the corresponding temperatures are shown on the right. The arrows on the left side of the image show the paths of neutrinos and photons as they travel away from the core, along with estimates of how long it takes for each to leave the Sun. Plasma flows inside the Sun are shown by the arrows on the image's right side. Image Credit: Kelvin Ma, Wikimedia Commons.

The core is a compact volume made of hot, dense plasma under the pressure of $2.342 \times$

10^{16} N m^{-2}, with a temperature of 1.570×10^7 K and a density of 1.527×10^5 kg m^{-3} (Carroll & Ostlie, 2017). It is located at the center of the Sun and extends outward to a distance $\sim 0.2 - 0.25$R$_\odot$ (García et al., 2007). In this region, nuclear fusion occurs, leading to the conversion of hydrogen atoms into helium (Broggini, 2003). The fusion process releases a significant amount of energy in the form of thermal radiation and electromagnetic radiation. Two different reactions can lead to one helium nucleus from four hydrogen nuclei. These are the proton–proton chain (PP-chain) reaction, which releases most of the Sun's energy, and the CNO cycle. In less massive stars like the Sun, where the temperature and pressure in the core are relatively low, the PP-chain reaction is the dominant mechanism for converting hydrogen into helium and releasing energy (Borexino Collaboration et al., 2018). An illustration of this chain is shown in Figure 1.2. The basic idea behind this reaction is that two protons collide and form a deuterium nucleus (or ^{2}H), a positron (e^+), and a neutrino (ν_e). The deuterium nucleus is then collided with by a proton, forming a helium-3 nucleus and a gamma ray (γ). The two helium-3 nuclei then combine to form a helium-4 nucleus, releasing two protons. The freed protons can then take part in additional reactions, extending the chain (Salpeter, 1952).

$$^1\text{H} + {}^1\text{H} \longrightarrow {}^2\text{D} + \text{e}^+ + \nu_\text{e} \tag{1.1}$$

$$^2\text{D} + {}^1\text{H} \longrightarrow {}^3\text{He} + \gamma \tag{1.2}$$

$$^3\text{He} + {}^3\text{He} \longrightarrow {}^4\text{He} + 2{}^1\text{H} \tag{1.3}$$

The overall reaction is:

$$4{}^1\text{H} \longrightarrow {}^4\text{He} + 2\text{e}^+ + \nu_\text{e} \tag{1.4}$$

emitting a total of 26.73 MeV of energy.

Core pressures, as well as temperatures, increase for stars with masses that are greater than 1.3 times the Sun's mass. Under such conditions, the CNO cycle becomes more effective than the PP-chain reaction (Salaris & Cassisi, 2005). Presently, just 1.2% of the Sun's energy is generated by the CNO cycle (Stix, 2002), but this percentage is expected to rise as the Sun ages and becomes more luminous (Borexino Collaboration et al., 2020). The CNO cycle is an alternate method of producing energy from hydrogen. The fusion of hydrogen nuclei is facilitated by catalytic reactions in which carbon, nitrogen, and oxygen serve as catalysts.

Above the core is the **radiative zone**, which is responsible for transferring the energy produced within the core. The radiative zone extends from the core to ~ 0.7R$_\odot$. The temperature and density fall in it with increasing distance from the core from about $7 - 2 \times 10^6$ K and $20 - 0.2$ g/cm^3, respectively. The predominant process of energy transport in the
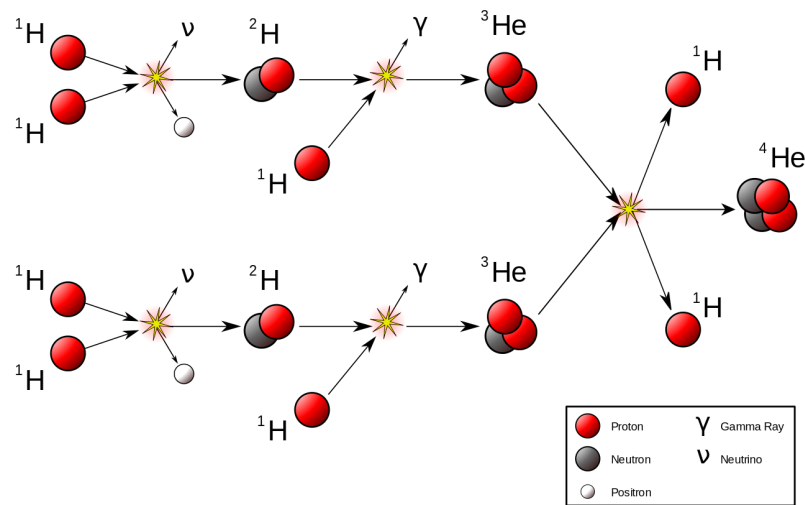
Figure 1.2: The proton–proton chain reaction for converting hydrogen atoms into helium in the Sun's core. Image Credit: Doctor C, Wikimedia Commons.

radiative zone is radiation (Koupelis, 2012). Photons produced from nuclear fusion in the core are in a perpetual interaction state with the plasma. During their transit through the radiative zone, photons experience scattering due to the interaction between photons and charged particles, ions and electrons, that are present within the plasma. This scattering causes photons to change their path randomly, resulting in a zigzag pattern. The frequent scattering events within the radiative zone can impede the progress of photons. As a result, the average time it takes a photon to travel through the Sun's exterior layers is hundreds of thousands of years.

The tachocline is a thin transition layer at the interface between the radiative and convective zones. The sudden transition from uniform rotation in the radiative zone to differential rotation in the convection zones creates strong shear flows in this area as the rotation rate changes rapidly (Tobias, 2005). The tachocline is believed to be closely associated with the dynamo process that generates the Sun's magnetic field (Gilman, 2005).

The outer layer of the solar interior, which is referred to as the **convection zone**, spans from the tachocline at roughly $0.7R_{\odot}$ to the visible surface of the Sun. In this layer, the plasma of the sun is neither dense nor hot enough to radiate the interior's heat energy. Instead, convection is responsible for transporting the energy. As the hot plasma rise from the tachocline towards the surface, it undergoes a cooling process as it emits energy in the form of thermal and electromagnetic radiation and subsequently experiences an increase in density. The relatively cooler plasma descends back to the interior, where it once again absorbs heat from the top of the radiative zone, thereby continuing the convective cycle. The convective motion plays a role in generating magnetic fields that impact solar phenomena, including but not limited to sunspots and solar flares.

1.1.2 The Solar Atmosphere

The solar atmosphere comprises of four layers, namely the photosphere, chromosphere, transition region, and corona. Figure 1.3 provides an illustration of the Sun's structure.
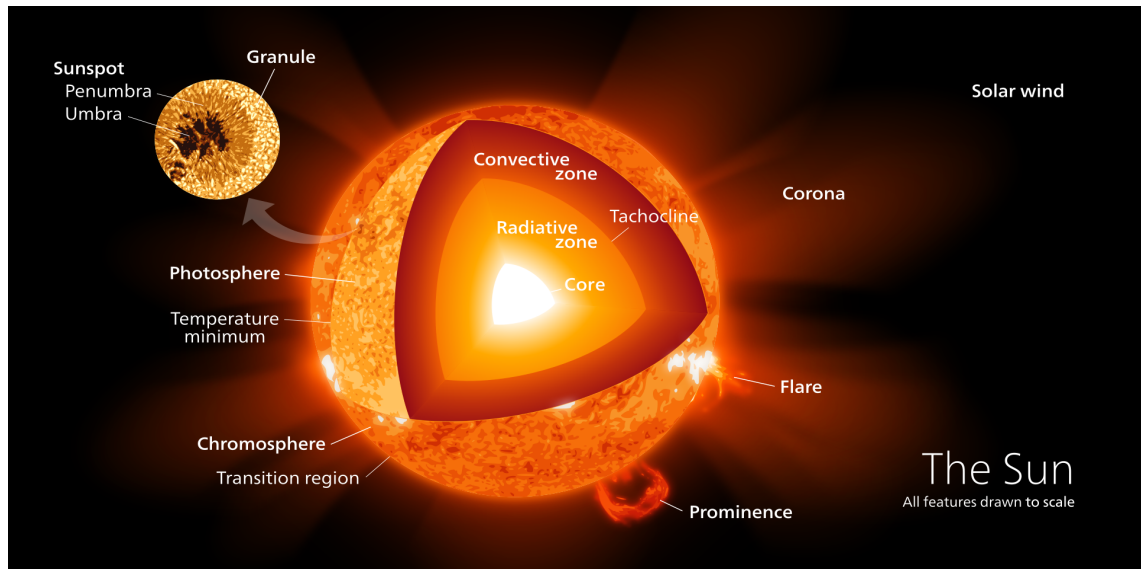
Figure 1.3: The Solar structure. Image Credit: Wikimedia Commons.

The photosphere is the visible surface of the Sun and emits most of its light. Approximately 99% of the solar energy is released in the photosphere. This layer has a temperature of 5800 K to 6000 K and is 500 km thick (Green & Jones, 2015). Because the upper layer of the photosphere is cooler than the lower layer, the edges of the photosphere are darker than the centre. This gradual decrease in brightness is referred to as limb darkening (Green & Jones, 2015). The photosphere is characterized by luminous bright areas surrounded by darker paths, as shown in Figure1.4, known as granules due to convective motion beneath its surface. Also, it is characterized by the appearance of sunspots, regions that exhibit lower temperatures and reduced brightness. These areas are closely linked to heightened magnetic activity and are significant signs of solar activity (Green & Jones, 2015).

The chromosphere is a relatively narrow layer of about 2000 km thick situated directly above the photosphere, dominated by a spectrum of emission lines specifically Hα line and Ca II H&K lines, and identified by a reddish hue visible during solar eclipses (Green & Jones, 2015), as shown in Figure 1.5. Electromagnetic emissions in the Hα spectral line give the chromosphere its signature red colour (Jess et al., 2015). The chromosphere displays intricate configuration and showcases dynamic characteristics, including spicules, which are slender and towering plasma jets that project upwards towards the solar corona with lifetimes between 1 minute and 15 minutes (de Pontieu et al., 2007; Scullion et al.,
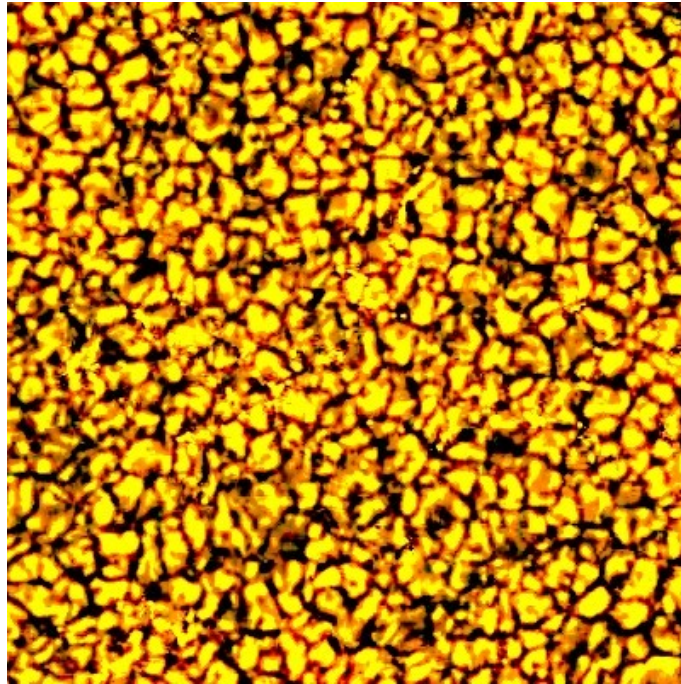
Figure 1.4: The Solar granules on the Sun's surface result from convective motions inside the convection zone. Image Credit: NASA.

2009). The temperature in the chromosphere increases with height, reaching a value of around 20000 K in the upper chromosphere (Iwai et al., 2017). The chromosphere is a significant zone for investigating the magnetic behaviour of the Sun.

The transition region is a thin layer approximately 100 km thick between the chromosphere and the corona. This region is characterized by a sharp rise in plasma temperature and an accompanying decrease in density. The temperature in the transition region rapidly increases from 20000 K in the upper chromosphere to approximately 1000000 K in the corona (Erdélyi & Ballai, 2007).

The corona is the outermost layer of the solar atmosphere that extends into space for millions of kilometres and can be observed as a luminous halo encircling the Sun in white light during a complete solar eclipse as shown in Figure 1.6. This region exhibits an exceptionally high-temperature range of 1000000 K to several million K (Erdélyi & Ballai, 2007). It is widely postulated that the corona's high temperature can be attributed primarily to the dissipation of magnetic energy, which occurs through various mechanisms, including magnetic reconnection (Erdélyi & Ballai, 2007; Browning et al., 2008) and/or MHD wave dissipation (Heyvaerts & Priest, 1983; Browning & Priest, 1984; Nakariakov et al., 1999). The corona generates the solar wind, an unceasing flow of electrically charged particles that emanates from the Sun and extends throughout the solar system.
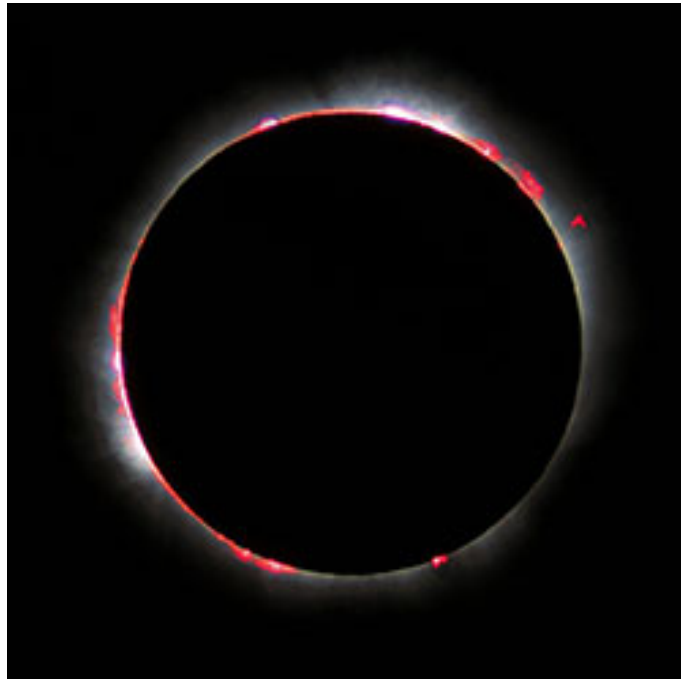
Figure 1.5: The reddish Solar chromosphere during a total solar eclipse in 1999. Image Credit: Luc Viatour/ HAO.

Figure 1.6: The white halo of the Solar corona during a total solar eclipse. Image Credit: NASA/Aubrey Gemignani.

1.1.3 The Solar Dynamo

The solar dynamo mechanism is the process by which the Sun produces and sustains its magnetic field. The complex and dynamic magnetic phenomena observed on the surface of the Sun, including sunspots, solar flares, and coronal mass ejections, are attributed to this mechanism. The solar dynamo is commonly described as an alpha-omega ($\alpha\Omega$) dynamo model, in which the magnetic field of the Sun is generated and amplified by the interaction of two components: the α effect and the Ω effect. A poloidal field runs through the photosphere in this model, while the toroidal field is created in the subsurface layers (Cameron et al., 2017). The Sun's convective motions produce a turbulent and helical flow, known as the α effect, which generates poloidal magnetic fields, which rise to the surface, forming a magnetic loop that runs across the photosphere. This alpha effect causes the groups of sunspots on the Sun surface. The Ω effect is characterised by generating toroidal magnetic fields via differential rotation where different latitudes on the Sun rotate at different speeds (Schmitt, 1987) see Figure 1.7. This difference in rotation causes a shear in the plasma, which stretches and amplifies the poloidal magnetic field, changing it to a toroidal magnetic field in east-west direction. The 11-year solar cycle and other phenomena in solar activity result from the interaction between the Sun's toroidal and poloidal magnetic fields, which leads to the regeneration and amplification of the magnetic field.
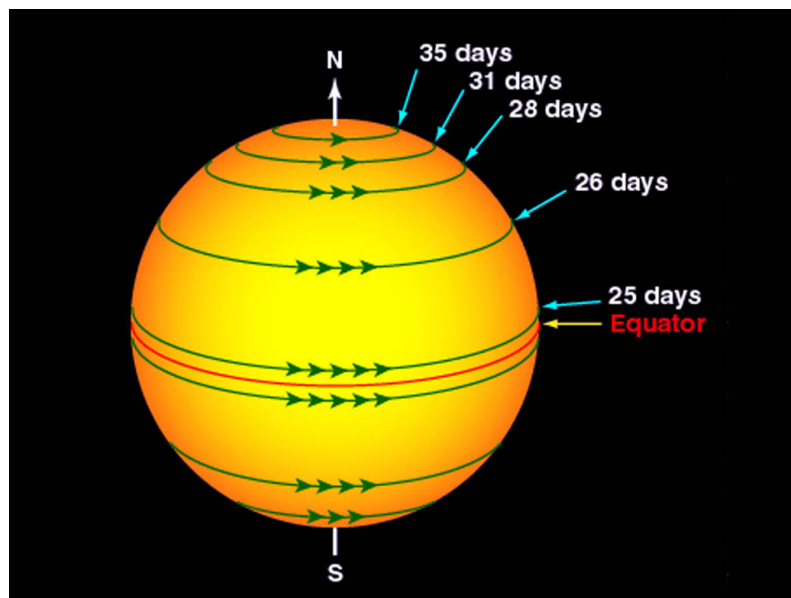
Figure 1.7: Different latitudes on the Sun rotate at different rates due to the Sun's differential rotation. The image shows that the equator of the Sun rotates faster, about 25 days, than the poles, which take more than 30 days to complete one rotation. Image Credit: NASA.
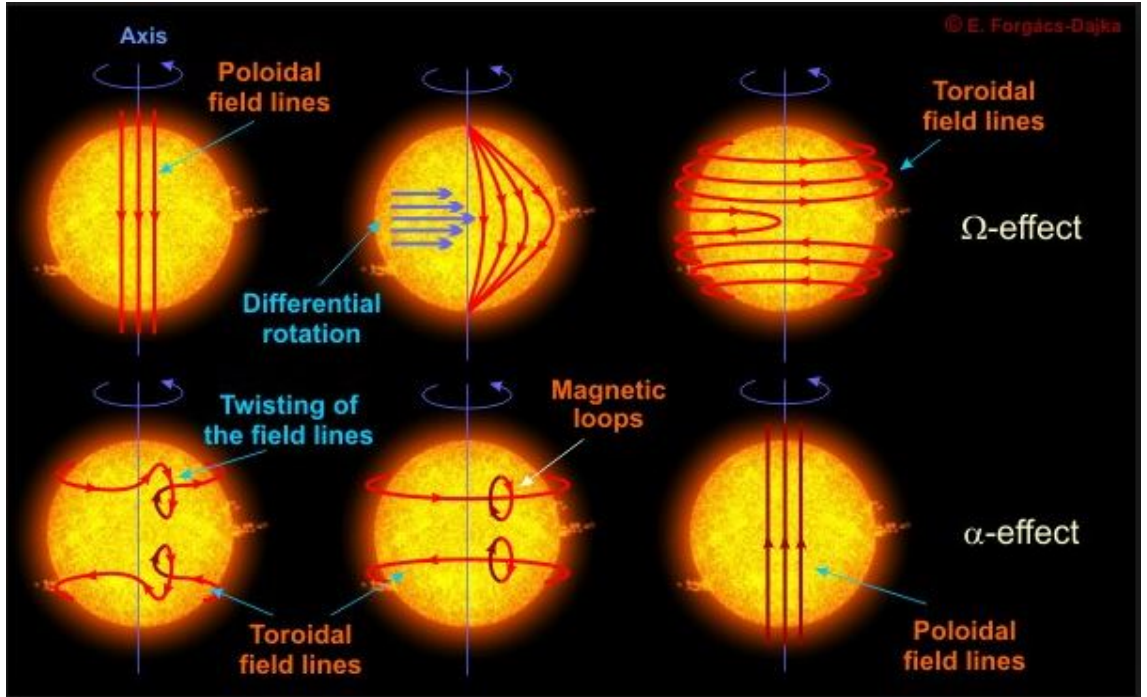
Figure 1.8: The (α) and (Ω) effects on the magnetic field structure in the Sun.
Image by E. F. Dajka.

For a dynamo to function, it requires a fluid medium that can conduct electricity, such as highly ionised gas (plasma), rotation motion that helps to promote the fluid's convective motions and a source of internal energy that drives the convective fluid motions (Pallé, 2010). The induction equation describes how the Sun's magnetic field is generated. Magnetohydrodynamics (MHD) combines fluid dynamics and electromagnetism to investigate the behaviour of electrically conducting fluids, such as plasmas, in magnetic fields, and the induction equation is a fundamental partial differential equation in this field and it is given by

$$\frac{\partial \mathbf{B}}{\partial t} = \eta \nabla^2 \mathbf{B} + \nabla \times (\mathbf{u} \times \mathbf{B}) \tag{1.5}$$

where $\mathbf{B}$ is the magnetic field vector, t is time, $\mathbf{u}$ is the velocity (fluid flow) vector and $\eta = 1/(\sigma\mu)$ is the magnetic diffusivity, a parameter indicating how easily magnetic fields can diffuse through a medium, where σ is the electrical conductivity and μ is the permeability of free space.

The first term in the induction equation 1.5 vanishes when the magnetic diffusivity (η) approaches zero. In this case, the induction equation for the magnetic field in the ideal conductive fluid becomes:

$$\frac{\partial \mathbf{B}}{\partial t} = \nabla \times (\mathbf{u} \times \mathbf{B}) \tag{1.6}$$

This is equivalent to having an infinitely conducting fluid. The fluid in this situation

is called perfect or ideal conductive fluid. Equation 1.6 describes the evolution of the magnetic field over time due to the motion of the conducting fluid. If the velocity field $\mathbf{u}$ and the initial magnetic field $\mathbf{B}$ are such that $\mathbf{u} \times \mathbf{B}$ results in a positive $\partial|\mathbf{B}|/\partial t$, it implies an increase in the magnitude of the magnetic field vector $|\vec{B}|$ over time. This growth of the magnitude of the magnetic field vector generated by the motion of the fluid is what is referred to as a dynamo.

In dynamo theory, the MHD approximation of an ideal conductive fluid is crucial for understanding the formation and development of magnetic fields. The magnetic field produced by the Sun is caused by the convective motion of the plasma in its interior, which functions as an electrically conductive fluid. This motion, combined with the Sun's differential rotation, generates the solar magnetic field, which is important in various solar phenomena such as sunspots, solar flares, and coronal mass ejections.

1.1.4 Solar Activity

Sunspots and Active Regions

Sunspots are dark regions of decreased temperature that appear on the solar surface for several days to a few months. Strong magnetic fields generated by the Sun's internal dynamo are often accompanied by the appearance of sunspots. Sunspots are created when these magnetic fields emerge and interact with the plasma on the Sun's surface (Charbonneau, 2014). As they are regions of intense magnetic fields that impede the convective flow of the plasma, sunspots are much cooler than the surrounding photosphere, with temperatures between 3500 K and 4550 K, giving them a darker appearance. Sunspots are characterized by two main structures, a dark central region called the umbra and a lighter surrounding region called the penumbra (Mathew et al., 2003; Schlichenmaier et al., 2010), see Figure 1.9. The diameter of a sunspot can range from a few hundred to tens of thousands of kilometres. Larger sunspots are typically less frequent than smaller ones (Bogdan et al., 1988). The 11-year solar cycle and solar activity are both closely associated with the presence of sunspots. Sunspots are frequently found in groups or clusters, and as the solar cycle progresses, their number and distribution vary over time. The study of sunspots reveals important information about the Sun's magnetic field, solar flares, and other phenomena associated with solar activity.

Active regions (ARs) are defined as regions on the surface of the Sun that display intense magnetic activity, frequently linked to the existence of sunspots. The active regions exhibit intricate magnetic configurations and have the potential to generate solar flares, coronal mass ejections (CMEs), and other high-energy phenomena.
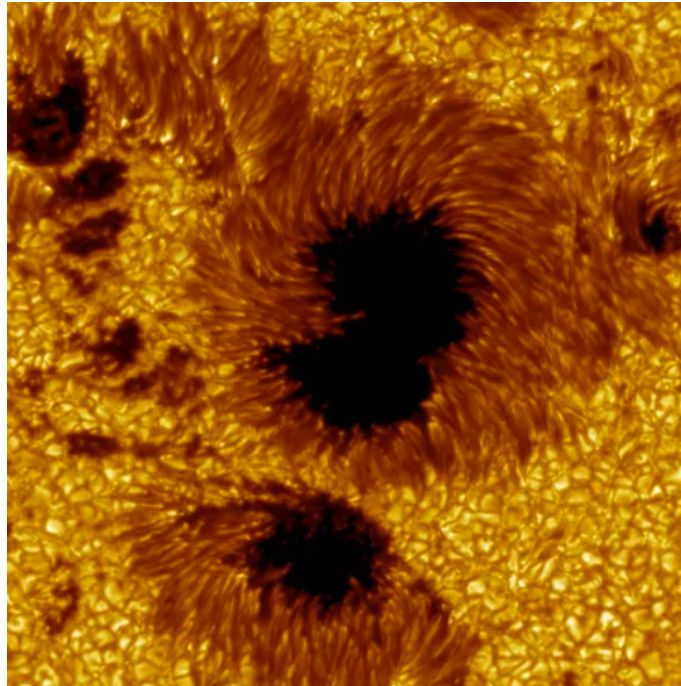
Figure 1.9: Sunspots on the surface of the Sun show the darker umbra regions circled by the lighter penumbra regions. Image Credit: NASA/Royal Swedish Academy of Sciences.

Solar Prominence

Solar prominences, also called filaments, are large-scale structures with elongated curved shapes that project from the surface of the Sun into the corona (Gunár et al., 2023). Figure 1.10 displays an image of a solar prominence. In contrast to the hotter more tenuous corona, prominences are primarily composed of cool, dense plasma. Solar prominences can reach up to several thousands of kilometers into space and persist for a considerable amount of time, ranging from days to months. Most prominence eruptions are associated with the emission of a coronal mass ejection (Gopalswamy et al., 2003). Prominences when seen on the limb of the Sun are emission features, but when they are seen on the disk of the Sun they are absorption features and called filaments, which have dark stripe appearance.

Solar Flares

Flares are high-energy outbursts that take place on the surface of the Sun. They are caused by the sudden release of magnetic energy via the reconnection of the magnetic fields stored in the Sun's atmosphere (Walkowicz et al., 2011). Figure 1.11 shows an image of a solar flare. A significant quantity of electromagnetic radiation in all wave-
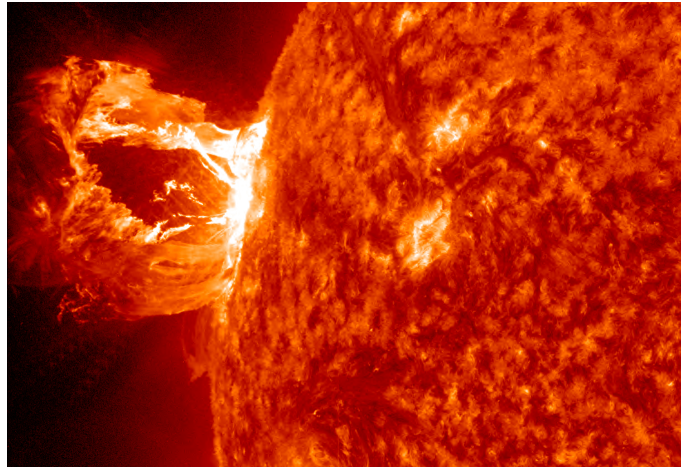
Figure 1.10: Giant prominence eruption. Image Credit: NASA/SDO/AIA.

lengths, particles, and plasma is emitted into space by flares (Shibata & Magara, 2011). The radiation that is released can potentially cause substantial effects on the upper atmosphere and ionosphere of Earth, leading to disturbances in satellite operations and radio communications. Solar flares are closely associated with the Sun's magnetic field and are often detected in regions with high activity levels, such as those with sunspots and strong magnetic phenomena. Since the main topic of this thesis is related to flares, solar and stellar flares are discussed separately in section 1.3.2.
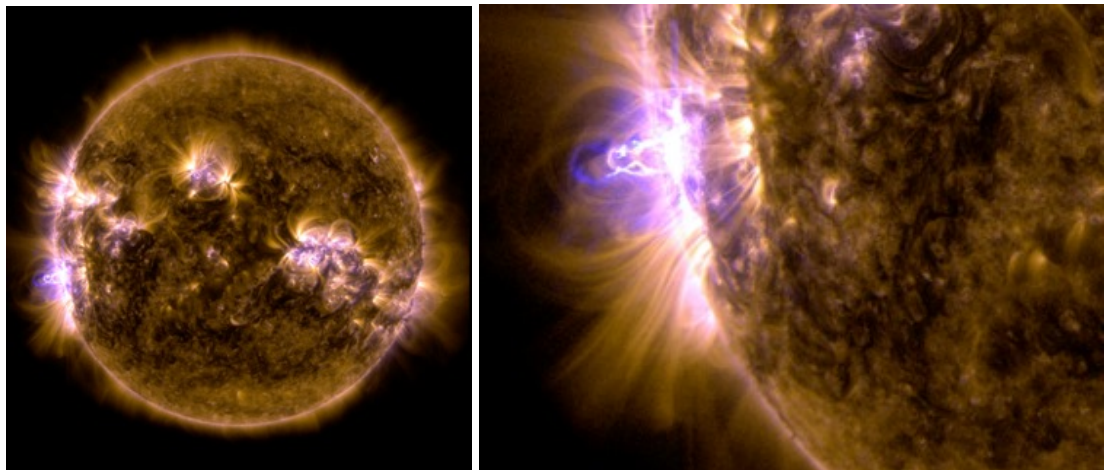
Figure 1.11: The sun in ultraviolet light shows a solar flare eruption on the left side. Image Credit: NASA/SDO.

Coronal Mass Ejections (CMEs)

Coronal Mass Ejections (CMEs) refer to the enormous ejections of magnetic field and plasma mass from the Sun's corona into surrounding space. An image of CME is shown

in Figure 1.12. CME is often accompanied by the release of magnetic fields that have been twisted and stressed in the corona of the Sun. Several processes, including magnetic reconnection, flux emergence, and the emergence of twisted magnetic structures from below the solar surface, can cause these magnetic fields to become unstable. When magnetic energy is released, the plasma quickly expands and is ejected (Forbes, 2000). CMEs move farther from the Sun at various speeds, between 250 km/s to approximately 3000 km/s (Chen, 2011). Therefore, CMEs take from about 18 hours to several days to reach Earth. When a coronal mass ejection reaches interplanetary space, it is called an interplanetary coronal mass ejection (ICME). Interactions between ICME and Earth's magnetosphere can result in geomagnetic storms, aurora events, and disturbances with electrical power grids and satellite communications (Tsurutani & Lakhina, 2014).
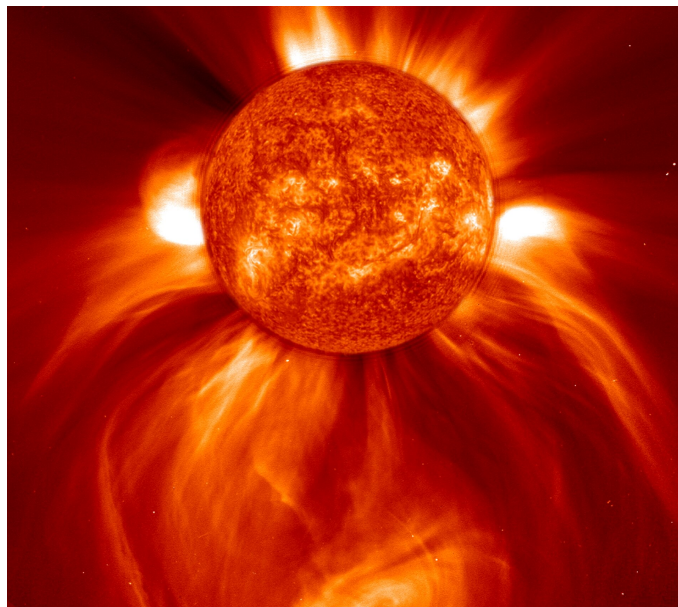
Figure 1.12: Coronal mass ejections (CMEs). Image Credit: ESA/NASA/SOHO.

Magnetic Reconnection

The process of magnetic reconnection is crucial in plasma and is key in many astrophysical phenomena, such as solar flares and coronal mass ejections (CMEs). Magnetic reconnection occurs in extremely conducting plasma where the magnetic topology is changed, and magnetic energy is transformed into kinetic energy, thermal energy, and particle acceleration. During magnetic reconnection, magnetic field lines with opposite orientations and polarities approach merge and reconnect in a region called *diffusion region*, resulting in a reorganisation of the magnetic field's topology. This process releases magnetic energy stored in the magnetic fields and converts it into thermal and kinetic energy (Ya-

mada et al., 2010). A diagram of the magnetic reconnection is shown in Figure 1.13. The released energy fuels explosive events, such as solar flares and CMEs, in which massive amounts of energy are rapidly released through electromagnetic radiation, high-energy particles, and plasma ejections.
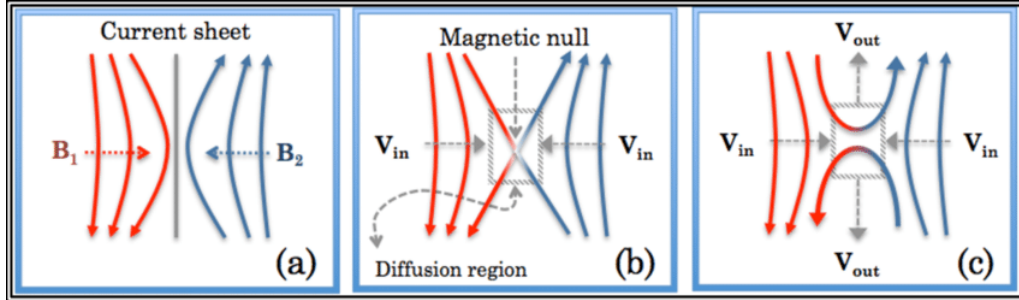
Figure 1.13: The figure illustrates the magnetic reconnection process. (a) shows two magnetic fields are brought together at the edges of a current sheet. (b) Displays the reconnection of the two magnetic field lines in the diffusion region.. (c) The plasma is being convected away by the newly reconnected magnetic field lines. Image Credit: Genestreti et al. (2012)

Several theoretical models have been developed to understand and describe the complicated process of magnetic reconnection. The Sweet-Parker model is a theoretical model that describes the magnetic reconnection process in a plasma Sweet (1958). In this model, magnetic reconnection happens when oppositely directed magnetic field lines are brought together in a thin, long current sheet. Due to the limited resistance of the plasma inside the current sheet, magnetic field lines can diffuse and reconnect, converting magnetic energy into kinetic and thermal energy. The reconnection rate predicted by the Sweet-Parker model is slow, resulting from the limited diffusion of magnetic fields across the narrow long current sheet and is given by:

$$V_i \approx \frac{\upsilon_A}{R_m^{1/2}} \tag{1.7}$$

where υ_A is the Alfvén speed of the medium and R_m is the magnetic Reynold's number. From equation 1.7, the reconnection inflow speed V_i which prescribes the reconnection rate is considerably lower than Alfvén speed because the magnetic Reynold's number is much larger than one. However, observational evidence shows that reconnection occurs much faster than predicted by the Sweet-Parker model in many cases. For example solar flare, in coronal conditions the magnetic Reynold's number is very large $R_m = 10^8 - 10^{12}$ (Aschwanden, 2005) and the Alfvén speed $\upsilon_A = 10^5$ m/s. This would give a time scale of 10 days, however the time required for a solar flare to release its energy ranges from minutes to hours. This difference prompted the development of alternative models, such

as the Petschek model.

Petschek (1964) proposed a model for faster reconnection in which the diffusion region is much smaller and shorter than the Sweet Parker current sheet. As the length of the current sheet decreases, the amount of time needed to propagate through the diffusion region reduces, speeding up the reconnection process (Aschwanden, 2005). The model suggests the formation of stationary slow-mode shocks in the inflow regions, which divides the inflow and outflow regions leading to accelerating the plasma flow and the reconnection rate (Petschek, 1964). The Petschek reconnection inflow speed in Alfvén speed units is given by

$$V_i \approx \frac{\upsilon_{in}}{\upsilon_A} \approx \frac{\pi}{8 \ln R_m} \tag{1.8}$$

where υ_{in} is the inflow speed. Petschek reconnection model predicts a considerably faster reconnection rate than Sweet-Parker, and it can account for some observations of fast reconnection astrophysical phenomena like solar flares. The difference between the Sweet Parker and Petschek models is shown in Figure 1.14

The Solar Cycle

The Sun's magnetic field goes through an 11-year cycle called the solar cycle. Defined as the periodic fluctuation in the Sun's magnetic activity and the number and area of sunspots within roughly 11 years (Hathaway, 2015). The solar cycle is characterised by two primary phases: the maximum and minimum. During the solar cycle, solar radiation levels, the number and size of sunspots, flares, and coronal mass ejections fluctuate synchronously from the period of minimum activity to the period of maximum activity and back again to the period of minimum activity. An image of the solar cycle can be seen in Figure 1.15. Throughout the solar maximum, the Sun undergoes heightened magnetic activity, leading to a rise in the number of sunspots, solar flares, and coronal mass ejections. While the solar minimum refers to the stage characterised by the lowest amount of solar activity as the number of sunspots decreases, which leads to a decrease in the rate of solar flares and coronal mass ejections. During each solar cycle, the Sun's magnetic field flips nearly at the solar maximum (Hathaway, 2015). Different solar cycles exhibit varying levels of solar activity, with some cycles showing a higher frequency of sunspots and others showing comparatively less activity.
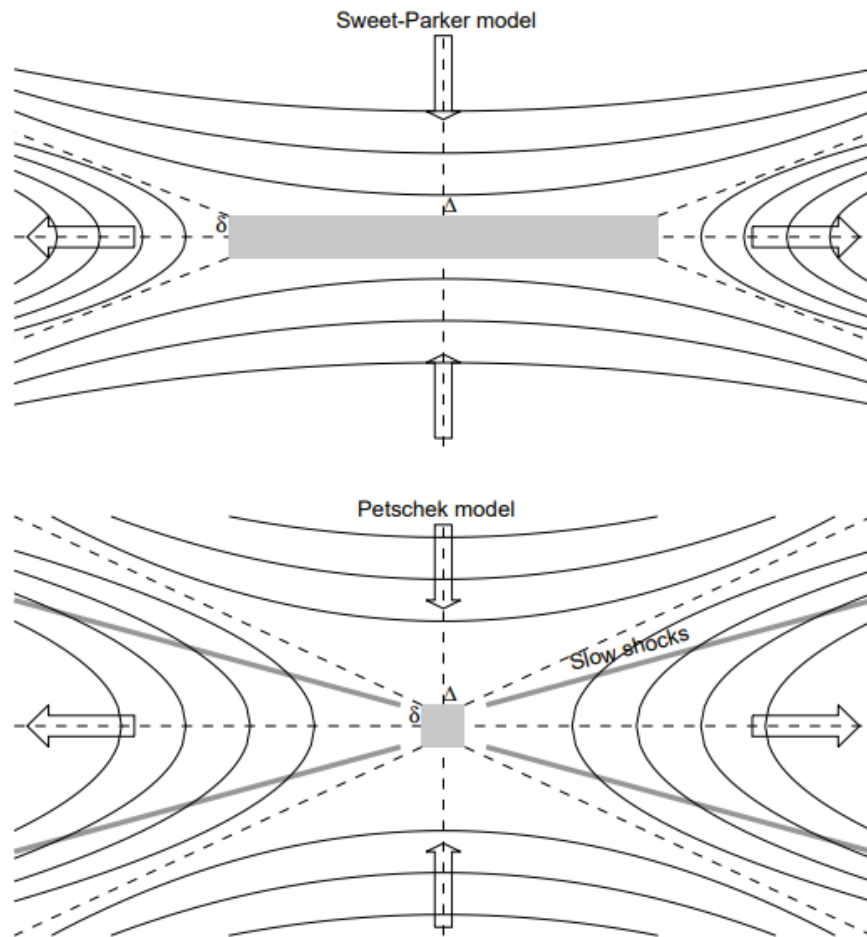
Figure 1.14: The figure illustrates the Sweet-Parker reconnection model (top) and the Petschek reconnection model (bottom). The diffusion region (grey box) in the Sweet-Parker model is characterised by a thin long sheet $\Delta \gg \delta$, while in the Petschek model, the diffusion region appears to be considerably more compact ($\Delta \approx \delta$). The Petschek model includes slow-mode shocks within the outflow region. Image Credit: Aschwanden (2005)
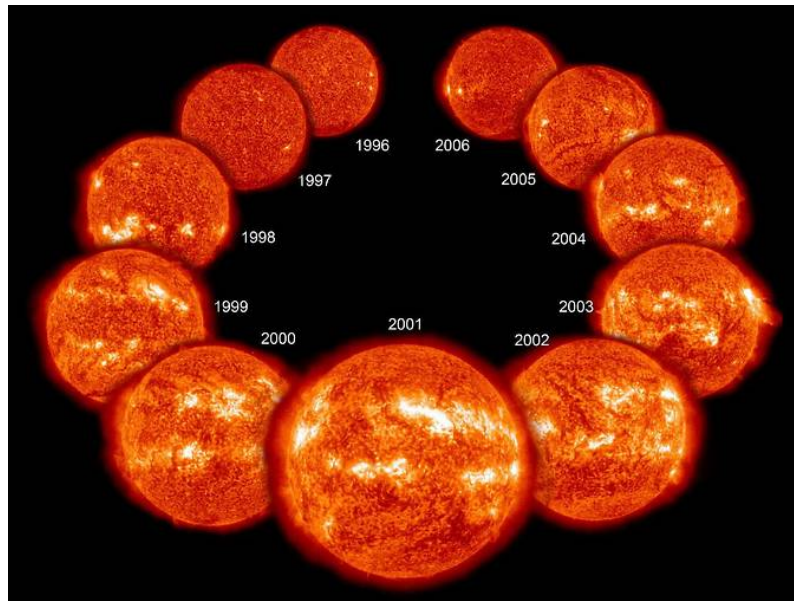
Figure 1.15: The Sun during the solar cycle 23. The cycle starts from the solar minimum on the upper left to the solar maximum and then back again to the solar minimum on the upper right. Image Credit: NASA

1.2 Other Stars and Their Activity

1.2.1 Classification of Stars

The classification of stars based on their spectral properties is known as stellar classification, and it reveals significant information regarding their characteristics, developmental phase, and conduct. A star's electromagnetic radiation is analysed into a spectrum that comprises distinct spectral lines. These lines signify the presence of particular molecules or chemical elements in the stellar atmosphere. According to the abundance of the corresponding chemical element in the star, the strength of the spectral lines varies, with strong lines indicating higher concentrations and weak lines indicating lower concentrations. The intensity of the spectral lines varies with temperature, allowing to deduce the photosphere temperature of the star.

Spectral classes are a system for categorising stars based on their spectra, specifically the photosphere's temperature. The Harvard Spectral Classification is the most widely used method for classifying stars based on the strength of absorption lines present in their spectra (Green & Jones, 2015). It uses a series of letters (O, B, A, F, G, K, and M) to denote distinct spectral classes to represent different temperature ranges ranging from the hottest (O-type stars) to the coolest (M-type stars). For the classification of cooler stars, additional spectral classes have been added. The classes L, T, and Y are part of the extended spectral classification system, particularly for brown dwarfs and other cool

objects (Kirkpatrick, 2005; Kirkpatrick et al., 2012). Each spectral class corresponds to a specific temperature range. Then each spectral class has been further subdivided into ten categories numbered, from 0 (the hottest) to 9 (the coolest), known as spectral types Koupelis (2012). For example, the Sun is a G2 star with a surface temperature of about 5778 K (Severino, 2017). O-type stars, the hottest stars in the observable universe, have a blue-violet colour and are characterized by their high temperature and mass, with surface temperatures that surpass 30,000 K. B-type stars, which are blue-white in colour, have a high surface temperature, ranging from 10000 K to 30000 K. A-type stars exhibit a relatively lower temperature ranging from 7500 K to 10000 K and a characteristic white colour, whereas F-type stars exhibit a comparatively cooler temperature between 6000 K and 7500 K and manifest a yellowish-white appearance. Yellow G-type stars, such as the Sun, exhibit a surface temperature from 5200 K to 6000 K. K-type stars exhibit lower surface temperatures between 3700 K and 5200 K, resulting in an orange colour, while M-type stars display the lowest surface temperatures, from 2400 K to 3700 K and exhibiting a red appearance (Koupelis, 2012).

Stars sometimes are grouped into three distinct categories based on their mass. Stars with masses of less than approximately $2M_\odot$ are classified as low-mass stars (Torres et al., 2010). These stars, such as red dwarfs and brown dwarfs, exhibit lower temperatures and luminosity compared to their higher-mass counterparts, resulting in extended lifetimes. Stars with masses ranging from $2M_\odot$ to $8M_\odot$ are classified as intermediate-mass stars. These stars exhibit higher temperatures, greater luminosity, and possess varying lifespans spanning from several million to several billion years. In contrast, stars with masses exceeding $8M_\odot$ are classified as high-mass stars. These stars exhibit a marked increase in temperature and luminosity, yet possess comparatively abbreviated lifespans, typically spanning from several million to several tens of millions of years.

1.2.2 The Hertzsprung-Russell Diagram

The Hertzsprung-Russell Diagram is a chart that plots the surface temperature or spectral class (x-axis) of stars against their luminosity or absolute magnitude (y-axis) see Figure 1.16. It was independently developed by astronomers Ejnar Hertzsprung and Henry Norris Russell in the early 20th century (Russell, 1914).

The Main Sequence dominates the Hertzsprung-Russell diagram and forms a curved, diagonal band that extends from the upper left, which is occupied by high-temperature blue stars with high luminosity, to the lower right, which is occupied by low-temperature red stars with low luminosity. Stars in this band are undergoing the process of hydrogen fusion within their cores to form helium. The star maintains hydrostatic equilibrium dur-
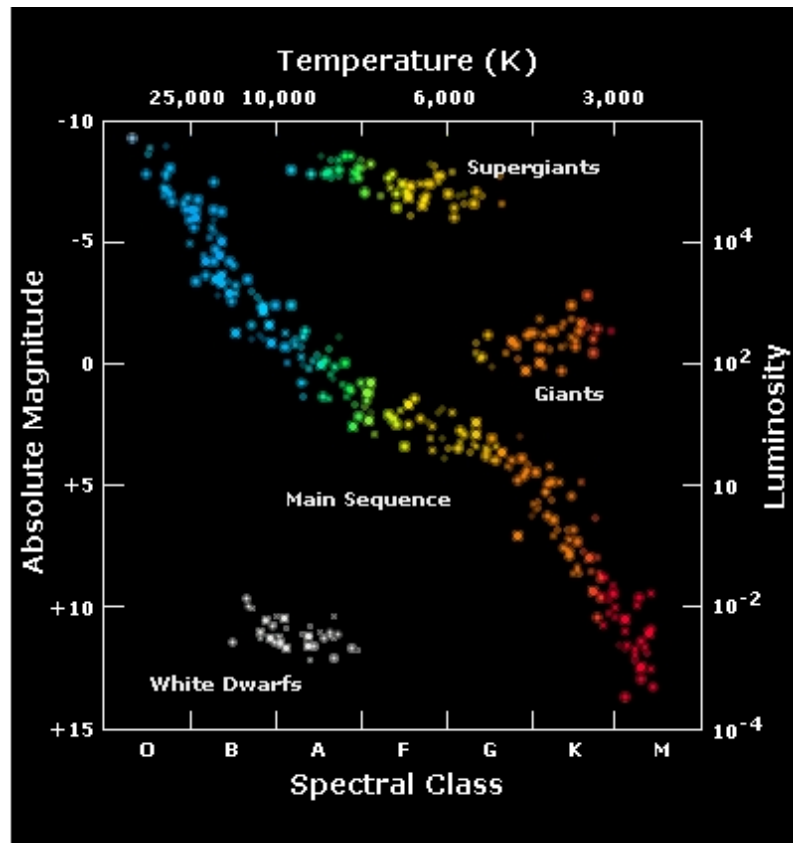
Figure 1.16: The Hertzsprung–Russell diagram illustrates the relationship between spectral class and luminosity, absolute magnitude, and surface temperature. The main sequence runs from bright, hot stars in the upper left to cooler, dimmer ones in the lower right. White dwarfs are located below the main sequence, while giants and super-giants stars are found above it. Image Credit: ESA

ing the main sequence, with the gravitational force being balanced by the pressure of the surrounding gas and radiation (Kippenhahn et al., 2013; Green & Jones, 2015). Stars that are classified as giant or supergiant are in a more advanced stage of stellar evolution, having consumed their core hydrogen. These stars can be observed above the main sequence band, and are more luminous than those in the main sequence, and cooler. However, their massive size ensures that they stay very bright. The lower left of the Hertzsprung-Russell diagram is occupied by the White Dwarfs. They are high-temperature stars, although having lower luminosity relative to main-sequence stars with comparable temperatures. This is because their radius are small but contain a lot of mass. The location of a star on the HR diagram is determined by Stefan-Boltzmann law as applied to a star given by:

$$L = 4\pi R^2 \sigma T^4 \tag{1.9}$$

where L is the star luminosity, σ is the Stefan–Boltzmann constant, R is the star radius and T is the star effective temperature.

1.3 Solar and Stellar Flares

1.3.1 The Standard 2D Flare Model

The CSHKP flare model, which is named after its principal contributors who proposed and developed the model Carmichael (1964); Sturrock (1966); Hirayama (1974); Kopp & Pneuman (1976), is a prevalent standard 2D model that explains the process of solar flares. This model assumes that solar flares are initiated by the sudden reconnection of magnetic field lines within the Sun's atmosphere. The model demonstrates how that magnetic reconnection releases accumulated magnetic potential energy and the consequent eruption of matter. During the magnetic reconnection process, magnetic field lines within a plasma, generating from distinct areas and with opposing orientations, undergo collision and reconnection resulting in a reconfiguration of the magnetic field lines. The reconnection process occurs in a region known as the diffusion region, characterized by a notable decrease in magnetic field intensity and the presence of plasma flow along the region. An illustration of the CSHKP model is shown in Figure 1.17.

In this model, the flare process begins when a prominence rises above the neutral line and stretches the magnetic field lines, creating an electric current sheet where the current flows parallel to the neutral line. This current sheet is prone to undergo either Sweet-Parker or Petschek magnetic reconnection, which makes the magnetic field lines collapse in the current sheet on both sides following the prominence's eruption. A lateral inflow
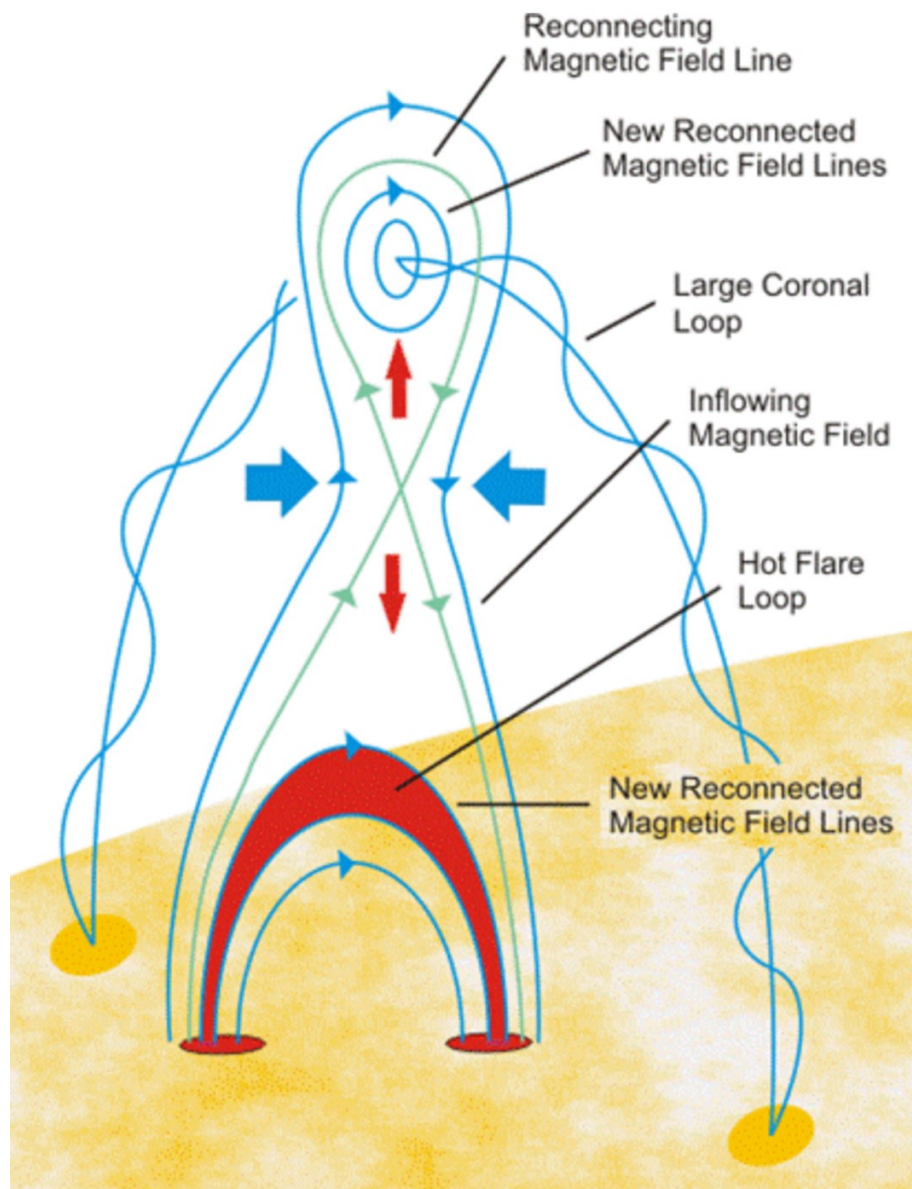
Figure 1.17: The Standard 2D Flare Model. Image Credit: NASA

of plasma into the opposing sides of the current sheet occurs concurrently with the magnetic collapse (Aschwanden, 2005). Magnetic reconnection occurs in the diffusion region, where magnetic energy dissipates and converts into thermal energy and accelerates nonthermal particles (electrons and ions) to high velocities. The energy released during magnetic reconnection heats the local coronal plasma, raising its temperature significantly. This process creates thermal conduction fronts that propagate outward from the diffusion region. The thermal conduction fronts and precipitating nonthermal particles heat the chromospheric footpoints of the recently reconnected magnetic field lines. This can lead to enhanced heating and brightening of the chromospheric material at those locations (Aschwanden, 2005). The intense heating of the chromosphere causes the plasma in that region to evaporate rapidly from the lower layers and rise into the corona. This heated and overdense plasma fills the newly reconnected magnetic field lines, leading to the formation of loops of hot, ionized plasma in the solar corona. These loops are visible in soft X-rays, and their temperatures range from $10 - 40 \times 10^6$ K. As the hot plasma in the flare loops cools to $1 - 2 \times 10^6$ K, it emits radiation in the extreme ultraviolet (EUV) wavelength range. As the plasma continues to cool further to temperatures of $10^4 - 10^5$ K, it becomes visible in the Hα wavelength range (Aschwanden, 2005).

1.3.2 Solar and Stellar Flares

Solar flares are sudden and intense brightening caused by magnetic reconnection events in the Sun's atmosphere. During these events, the twisted magnetic field lines realign, releasing large amounts of energy. This energy accelerates charged particles, such as electrons and protons into space, and emits a wide range of electromagnetic radiation at all electromagnetic spectrum wavelengths, from radio waves to gamma rays (Davenport, 2016). The magnetic energy needed to accelerate particles and heat plasma is thought to come from active regions. Solar flares are commonly observed in or around areas characterized by high levels of magnetic activity, such as active regions and sunspots, where strong magnetic fields lines break through the photosphere and connect the solar interior to the solar corona (Walkowicz et al., 2011; Jiang et al., 2012). The duration of solar flares is related to the amount of energy released and the particular physical processes driving the flare. In general, solar flares duration varies from a few minutes to several hours (Grieder, 2001; Reep & Knizhnik, 2019). Solar flares that last longer than 30 minutes are classified as Long Duration Events (LDEs) (Grieder, 2001).

Flares go through different phases, each of which can last for a different amount of time, from a few minutes to a few hours. Figure 1.18 shows the duration and different phases of the same flare, observed at different wavelengths. The *preflare phase*, charac-

Table 1.1: Solar flares classification scheme showing the peak of X-ray flux in (W/m^2) with wavelengths of 1–8 Å.

Class	peak of X-ray flux (W/m^2)
A	$< 10^{-7}$
B	$10^{-7} - 10^{-6}$
C	$10^{-6} - 10^{-5}$
M	$10^{-5} - 10^{-4}$
X	$> 10^{-4}$

terised by the slow heating of coronal plasma, can be observed at soft X-rays and EUV wavelengths. At times, non-thermal emissions are detected before the main flare phase (Benz, 2017). Subsequently, the *impulsive phase*, characterised by the initial release of magnetic energy, is followed by the acceleration of many energetic electrons and ions. Hard X-ray footpoint sources are detected at lower altitudes (Hoyng et al., 1981), and intense radio emissions are observed caused by trapped high-energy particles. The *peak phase (flash phase)* occurs after the impulsive phase, characterised by maximum intensity of thermal emissions like soft X-rays and Hα, along with rapid rises in Hα intensity and line width. This period considerably overlaps with the impulsive phase. The *decay phase* occurs when the coronal plasma reverts to its initial state, accompanied by magnetic re-configuration, plasma ejections, and shockwaves in the high corona. Metre wave radio bursts and interplanetary particle events occur during this time (Benz, 2017).

Solar flares are classified based on their X-ray brightness, specifically the peak X-ray flux measured in the X-ray wavelength range (1 to 8 Å). The classification system for solar flares is known as GOES (Geostationary Operational Environmental Satellites) flare classification. The GOES classification system consists of two parts, class and magnitude. The class is represented by a letter (A, B, C, M, and X) based on the maximum X-ray flux it produced, from the lowest to the highest. The magnitude is represented by a number ranging from 1 to 9, indicating the strength of the flare relative to others in the same class, from the weakest to the strongest. An illustration of the classification system is shown in Table 1.1. Solar flares are extremely energetic events that can release energy between 10^{29} and 10^{32} ergs (Shibata & Yokoyama, 2002). In this energy range, flares are among the most powerful phenomena in our solar system. The most powerful solar flare ever observed was on September 1, 1859, and is known as the Carrington event (Carrington, 1859; Hodgson, 1859). During the Carrington event, an enormous solar flare of X45 class erupted and had an energy of 4.5×10^{32} erg, which had a significant impact on Earth. Smaller solar flares tend to occur more frequently than larger ones. A correlation has been observed between the number and size of sunspots and the number and intensity of
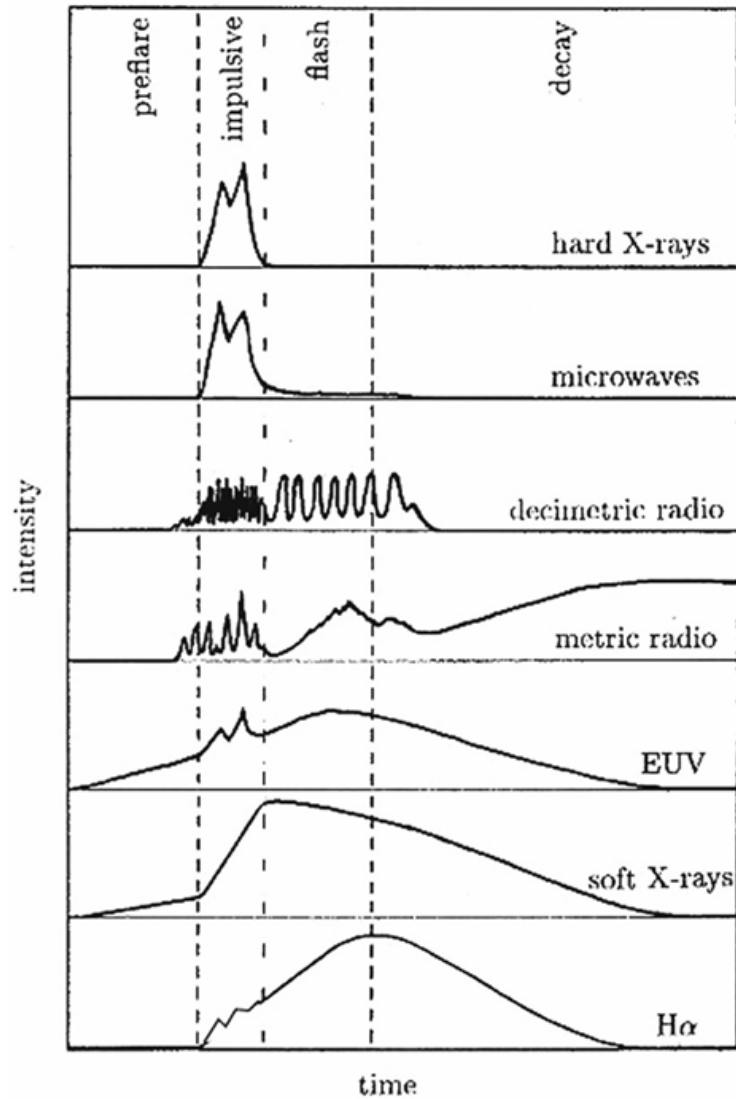
Figure 1.18: A diagram showing the intensity of a flare at various wavelengths. The different phases of a flare differ in duration. During a large event, the preflare phase usually lasts a few minutes, followed by the impulsive phase lasting 3–10 minutes, the flash phase lasting 5–20 minutes, and finally, the decay phase lasting several hours. Image Credit: Benz (2002)

flares. During periods of high solar activity, the number and size of sunspots increase. Therefore, several flare events may occur daily, while only one flare or less occurs weekly during the solar minimum (Grieder, 2001). Frequently solar flares are often associated with coronal mass ejections (CMEs). According to observations, CMEs events are more common in conjunction with high-energy solar flares (e.g. X-class) than low-energy solar flares (Gopalswamy & Webb, 2009). In addition, observations confirm a strong relation between CMEs events and slow, long-duration events (LDEs), also known as flares with the long rising phase (Bak-Steślicka et al., 2013). The emission of high-energy radiation during flares can induce ionization and thermal effects on the Earth's upper atmosphere, thereby causing disturbances in satellite operations, GPS systems, radio communications and power grids.

Impulsive brightness rises are observed in the light curves of many main sequence stars, and they are often referred to as "stellar flares." These flares are similar in nature to solar flares, but they occur on other stars. Stellar flares have the potential to occur in the majority of main sequence stars that possess external convective envelopes, encompassing both cool and hot stars (Pettersen, 1989). However, they are more frequently observed in low-mass stars, particularly M dwarfs (Walkowicz et al., 2011; Davenport, 2016). The probability of a flare occurring on a star depends on the spectral type of the star. Stars of different spectral types have different temperatures and sizes, which significantly affects magnetic activity and flare incidence. M-type red dwarf stars, which are relatively small and cool, are more susceptible to flaring than larger and hotter F- and A-type stars (Candelaresi et al., 2014). The convective zones of cooler stars, especially M-type red dwarfs, are larger and deeper than those of hotter stars, such as F- and A-types. This means that the entire volume experiences convective motion, which is crucial in generating intense and complex magnetic fields through the dynamo mechanism.

Flares from stars have been observed to be significantly more powerful than any solar flare ever recorded, with observed energies in the range of 10^{28} to 10^{32} erg. These flares with energy more than 10^{32} erg are called super-flares. Schaefer et al. (2000) were the first to report such flares on G-type stars; they identified nine superflares on solar-type stars with estimated energies between 10^{33} and 10^{38} erg. Several studies of stellar flares are discussed in Chapters 2 and 3.

1.3.3 White Light Flares

Flares with emissions observable at optical wavelengths are known as white light flares (WLFs) (Hao et al., 2017). They produce optical continuum emission over the quiescent photosphere, and are thought to be extremely rare (Fang et al., 2013). This continuous

emission can be represented by a blackbody spectrum characterised by temperatures often falling within the range of 5000 to 10000 K (Watanabe et al., 2013). During solar flares, the photospheric continuum emission is caused by several mechanisms, some of which are commonly interpreted as Hα continuum emission, hydrogen recombination emission, or both (Heinzel et al., 2017). The majority of the continuum emission from WLFs is thought to originate from the lower chromosphere down to the middle photosphere (Hao et al., 2017). Since the observation of the first WLF in 1859 (Carrington, 1859; Hodgson, 1859), very few WLFs have been recorded compared to the total number of solar flares so far (Song et al., 2018). WLFs can be categorised into two distinct types, namely Type I and Type II (Machado et al., 1986). The rising time of the WLF and the time of hard X-ray (HXR) peak and microwave radiation are tightly connected in type I WLFs. Also, the Balmer lines tend to be quite strong and wide (Fang et al., 2013). In contrast, type II WLFs exhibit none of these features (Ding et al., 1999). This classification suggests that WLFs may originate from various sources of white light emission and be driven by various heating mechanisms.

More discussion about WLFs studies is presented in chapter 2.

1.3.4 Multi Wavelength Observation of Solar and Stellar Flares

Stellar flares have been a subject of interest for researchers all over the years. They studied them not only in the visible light spectrum but across the entire electromagnetic spectrum, from gamma rays to radio frequencies.

The significance of X-ray observations of stellar flares lies in their ability to capture the emission of X-rays during the impulsive phase of the flare when energetic particles are accelerated to high speeds. Heise et al. (1975) conducted the first X-ray observations of stellar flares using the SAS-3 instrument. Their study successfully detected an X-ray flare originating from the M4.5V star YZ CMi. Chen et al. (2022) employed time-resolved X-ray spectroscopic observations conducted with the Chandra High Energy Transmission Grating Spectrometer (HETGS) to investigate the dynamics of stellar flares occurring on EV Lac. Distinct plasma flows resulting from flares in the corona of EV Lac were identified; however, none of these observations furnished substantiation for the occurrence of stellar coronal mass ejections (CMEs). The majority of solar flares exhibit a concurrent increase in the density and temperature of the coronal plasma as the plasma flow occurs.

Wu et al. (2022) conducted an analysis of spectroscopic data obtained from LAMOST DR7. The researchers successfully identified a stellar flare occurring on an M4-type star. These flares, known as Amplitude Super-flares, exhibit a distinct pattern characterised by a sudden and intense increase in the intensity of the Hα line, followed by a gradual

decrease. During the occurrence of a flare, the Hα line, which corresponds to a particular transition in the hydrogen atom, demonstrates a Voigt profile. Following a sudden and spontaneous surge in the intensity of the Hα line, a distinct augmentation was detected in the redward region of the Hα line profile. Furthermore, the approximate aggregate energy emitted via the Hα line during the flare is of the magnitude of 10^{33} erg, serving as an indication of the overall energy discharge linked to the occurrence.

1.4 Observation of White Light Stellar Flares

The term White Light refers to the part of the electromagnetic spectrum that contains visible light. In the context of solar and stellar flare measurements, White Light is often linked with electromagnetic radiation that falls between the wavelength range of around 400 to 700 nm. White Light flares are observed with a photometer telescope. A Photometers telescope is designed to be extremely light sensitive, allowing it to detect even the smallest variations in the brightness of stars. Photometer telescopes can target specific regions of the electromagnetic spectrum using various filters, enabling the study of phenomena such as exoplanet transits, stellar flares, and variable stars. Photometer telescopes frequently conduct time-series observations, constantly measuring the star's brightness over time. This continuous monitoring helps in identifying periodic light variations. Examples of photometer telescopes include the Kepler Space Telescope, which was used in the work for this thesis, the TESS Space Telescope, and a variety of ground-based observatories with photometric instruments.

1.4.1 Kepler and K2

NASA launched the Kepler spacecraft in 2009 with the primary objective of detecting Earth-sized exoplanets in the habitable zone of other stars using the transit method (Koch et al., 2010). This method involves continuously monitoring the brightness of many stars and looking for periodic, temporary decreases in brightness or transits. These transits occur when a planet passes in front of its host star. The spacecraft has a photometer with a 0.95-meter aperture, a sensitive light-gathering instrument that measures the star's brightness fluctuations. This photometer has 21 CCD modules, each of which contains two CCDs with resolutions of 2200 $\times$ 1024 pixels. Each module represents 5 degrees on the sky. The Kepler photometer has a single broad bandpass and the wavelength range of the this photometer ranging from 420 to 900 nm. Kepler has a wide field of view (FOV) of 105 deg^2 see Fig 1.19. This wide field of view allowed it to simultaneously observe a large sample size of various types of stars, including main-sequence stars, red

dwarfs, and other stellar types. The spacecraft pointed at a single region in the sky in the constellations of Cygnus, Lyra, and Draco for four years, continually monitoring around 200000 stars (Shibayama et al., 2013; Davenport, 2016; Yang & Liu, 2019a). The Kepler spacecraft had four reaction wheels to maintain stability and achieve the high pointing accuracy required for continuous observations. The spacecraft could retain its constant location and direct its telescope towards the Kepler field of view by adjusting the rotational speed and direction of the reaction wheels. The Kepler spacecraft rotated every 90 days to make its solar panels always facing the Sun. Thus Kepler data divided into a series of quarters, each lasting approximately 90 days. Kepler data products are archived at Mikulski Archive for Space Telescopes (MAST). Among these products are light curve files, target pixel data and full frame image (Thompson et al., 2016). Kepler used two different cadence modes to observe its targets. The long cadence mode (LC) provides one photometric data point every 29.4 minutes, and the short cadence mode (SC) provides one photometric data point every minute Pitkin et al. (2014). Kepler's capacity to constantly monitor the brightness of stars for an extended period made it an excellent tool for observing and studying stellar flares. The Kepler spacecraft was explicitly built to obtain high precision and long-duration light curves of several stars simultaneously. The time resolution of its observations and the high sensitivity enabled it to detect slight variations in star brightness, making it a perfect platform for researching planetary transits and for studying white-light stellar flares Davenport (2016). The Kepler light curves data were used for studying white-light stellar flares in chapters 2 and 3 of this thesis.

In August 2013, two of Kepler's reaction wheels failed, effectively ending the four-year primary mission of Kepler. K2, the second phase of Kepler's mission, began making observations in June 2014 and represents a novel approach to this problem (Howell et al., 2014). The telescope's field of view stabilised and pointed at different target areas of the sky along the ecliptic (see Figure 1.20) for shorter duration of 80 days using the solar pressure and the two remaining working wheels (Howell et al., 2014). The K2 mission lasted until the spacecraft's fuel supply ran out. On October 30, 2018, the Kepler spacecraft was retired after nearly 10 years of successful operation.

1.4.2 Transiting Exoplanet Survey Satellite (TESS)

The Transiting Exoplanet Survey Satellite (TESS) is a NASA space telescope (Ricker, 2015), Launched on April 18th, 2018 and designed specifically to detect transiting exoplanets by transit method where exoplanets periodically obscure some of their host stars' light. TESS will conduct a two-year survey of the entire sky by dividing it into 26 distinct sectors. It uses four CCD cameras, each with a 24 by 24 degree field of view, to scan
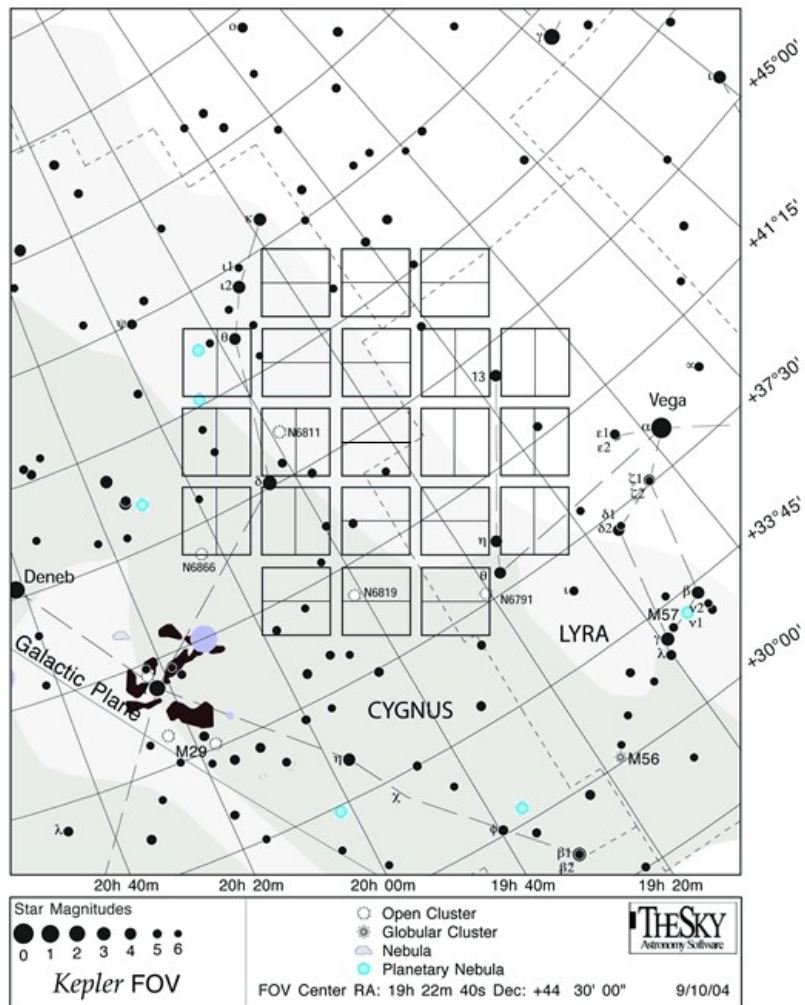
Figure 1.19: Kepler Field of View. Image Credit: NASA
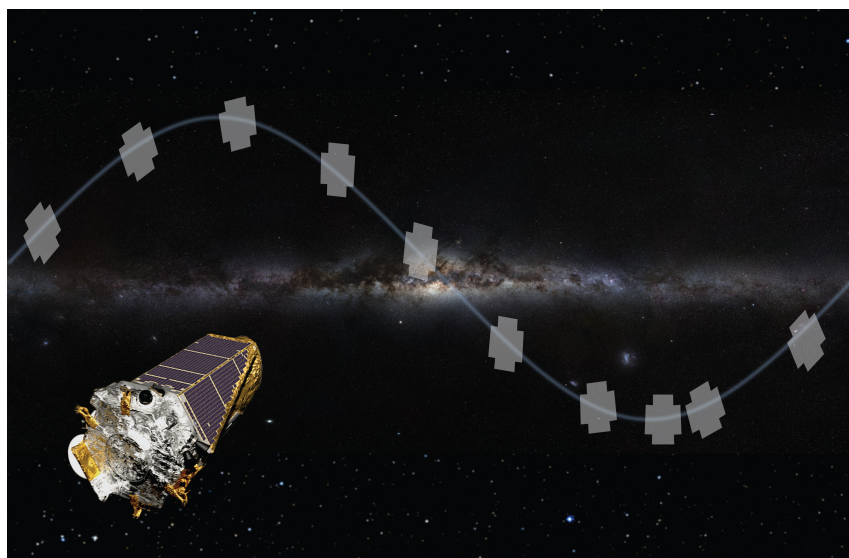
Figure 1.20: Different FOV of the K2 mission along the ecliptic , each were observed for about 80 days. Image Credit: NASA Ames/W. Stenzel.

vast portions of the sky, resulting in a total FOV of 24 by 96 degrees, covering an area approximately 400 times larger than the Kepler mission. This enables TESS to observe approximately 200,000 stars per observing sector. The spacecraft's powerful cameras observe each sector for 27.4 days, measuring the brightness of the brightest stars every two minutes using high-precision photometry. The TESS targets have been provided to the scientific community as calibrated light curves, target pixel files (TPFs) and full frame images (FFIs). TESS high-precision photometry of 2-minute cadence data has already been put to use for stellar flare research, such as Doyle et al. (2019, 2020, 2022).

1.5 Pre-Kepler flare monitoring studies

Before the Kepler space telescope, observations of stellar flares relied primarily on ground-based telescopes and data from earlier space missions. Researchers used ground-based observatories with photometers and spectrographs to monitor the activity of stars, detect transient events like flares, and study them at different wavelengths. Also, several space missions contributed to the observation and study of stellar flares across various wavelengths. Robinson et al. (1998) provided FUV observations of stellar flares and analysed medium-resolution echelle observations on the dM0e star AU Microscopii using the Space Telescope Imaging Spectrograph (STIS) aboard the Hubble Space Telescope, focusing on the physical characteristics and emission properties of the observed flare events, as well as the search for signatures of proton beams. Hawley (2000) studied the high-resolution

Hubble Space Telescope (HST) Space Telescope Imaging Spectrograph (STIS) spectra of the dMe star AD Leo to explore the process of atmosphere heating in flare stars and improve current models. Schaefer et al. (2000) detected nine occurrences of superflares, with energies ranging from 10^{33} to 10^{38} ergs, on normal solar-type stars. These findings were derived from observations conducted using different observatories and satellites. Hawley et al. (2003) presented the results of a comprehensive multiwavelength observing campaign conducted in March 2000 on the flare star AD Leonis. This campaign involved simultaneous observations from various ground- and space-based observatories, capturing data on eight significant flares. Güdel et al. (2004) conducted a detailed investigation of the nearby M dwarf star Proxima Centauri using data obtained from the XMM-Newton satellite. The study aimed to understand the X-ray emission properties and flare activity of Proxima Centauri, which is known to be a highly active star. By analyzing the X-ray data from XMM-Newton, Güdel et al. (2004) studied the variability of Proxima Centauri's coronal emission, the occurrence of flares, and the characteristics of individual flares in terms of their peak flux, duration, and spectral properties. Getman et al. (2008) presented a comprehensive analysis of pre-main-sequence (PMS) stars and their X-ray flares based on the Chandra Orion Ultradeep Project (COUP) dataset. The study analysed the shapes of flares and compared the properties of flares observed in the COUP dataset and those observed in other active X-ray stars and the Sun.

While the pre-Kepler observations lacked the precision and continuous coverage offered by more modern space missions like Kepler and TESS, they laid the foundation for understanding stellar flare characteristics, frequency, and energy release on different types of stars.

1.6 Thesis Outline

Main sequence stars can show considerable amplitude variations in their light-curves, which have been explained by the presence of large dominant starspots on the surface moving in and out of view as the star rotates. These amplitude variations in brightness represent one way of determining the star's rotation period. Furthermore, monitoring stars over long time intervals will enable the detection of flares and their energy. This is important for orbiting planets and is crucial for planetary habitability. Not only should a planet be a suitable distance from its host star, but also we need to know the star's properties. Stellar magnetic activity, and especially flare events, expose planets to a high photon flux and potentially erode their atmospheres.

Previous works of Maehara et al. (2012); Shibayama et al. (2013); Wu et al. (2015); Van Doorsselaere et al. (2017); Yang et al. (2017); Yang & Liu (2019a); Notsu et al. (2019); Okamoto et al. (2021) have focused on the statistical characteristics of superflares. However, how frequently and under what conditions superflares occur is still uncertain. Therefore, we explore a larger dataset and consider alternative methodologies using automated flare detection to study the statistical properties of stellar superflares with their energies on the on main-sequence stars of the entire Kepler data.

Each chapter in this thesis closely follows a peer-reviewed journal article by the PhD candidate with a co-author, in which three chapters have been published. In chapter 2, we examine the statistical characteristics of stellar super-flares occurring on main-sequence G-type stars using data obtained from the Kepler mission during quarters 0 to 17. Our analysis involves a comparison of our research outcomes with the findings presented by Okamoto et al. (2021). We examine the temporal evolution of flare statistics over a period of 17 quarters, and find the power law index α for the data quarters 0–6, 7–17, and 0–17. We analyse the statistical properties of stellar super-flares occurring on main-sequence stars of spectral types A, F, K, and M. We provide a Python script that enables the automated detection of super-flares, requiring only minimal manual analysis. Chapter 3 discusses the identification of 14 super-flares occurring on 13 Sun-like stars with slow rotation. Additionally, the chapter presents findings of 12 instances of high-intensity super-flares on five G-type dwarf stars, as well as seven occurrences on four M-type dwarf stars, with an analysis of these events. Chapter 4 presents predictions for instances of very short activity cycles. These predictions were based on an empirical relation and were organised in a tabular format. The purpose of this investigation was to determine if these short activity cycles in stars are a common occurrence. Chapter 5 provides a concise overview of the conclusions drawn from previous chapters.

2 Main-sequence Star Super-flare Frequency based on Entire Kepler Data

2.1 Summary of the chapter

This chapter is based on the publication of Althukair & Tsiklauri (2023b). We wrote and used an automated flare detection Python script to search for super-flares on main-sequence stars of types A, F, G, K, and M in Kepler's long-cadence data from quarter 0 to quarter 17 (Q0-Q17). We studied the statistical properties of the occurrence rate of super-flares. For the G-type data set, we compared our results with the previous results of Okamoto et al. 2021 by splitting the data set into four rotational bands. We found similar power law indices for the flare frequency distribution. Hence, we show that inclusion of high-pass filter, sample biases, gyrochronology and completeness of flare detection is of no significance, as our results are similar to Okamoto et al. 2021. We estimated that a super-flare on G-type dwarfs of energy of 10^{35} erg occurs on a star once every 4360 years. We found 4637 super-flares on 1896 G-type dwarfs. Moreover, we found 321, 1125, 4538 and 5445 super-flares on 136, 522, 770 and 312 dwarfs of types A, F, K and M, respectively. We found that the occurrence rate (dN/dE) of super-flares versus flare energy, E, shows a power-law distribution with $dN/dE \propto E^{-\alpha}$, where $\alpha \simeq 2.0$ to 2.1 for the spectral types from F-type to M-type stars. In contrast, the obtained $\alpha \simeq 1.3$ for A-type stars suggests that the flare conditions differ from the rest spectral-type stars. We note an increase in flare incidence rate in F-type to M-type stars and a decrease in A-type to F-type stars.

2.2 Introduction

Flares are unpredictable events defined as a sudden, intense brightening caused by a large burst on the stellar surface as a result of magnetic energy release during the reconnection

of magnetic fields in the outer atmosphere of stars, which are typically located above or near star-spots (Shibata & Magara, 2011; Walkowicz et al., 2011). Flares produce electromagnetic radiation with a wide range of wavelengths, from long-wavelength radio waves to short-wavelength gamma rays (Davenport, 2016).

In general the importance of Solar flares is due to their potential hazard to humankind, particularly damages to space technology such as satellites and terrestrial electrical power grids and pipelines via current surges generated by geomagnetic storms in the conductive layers of the Earth. Eastwood et al. (2017) considers an economic impact of space weather including the solar flares. Schulte in den Bäumen et al. (2014) made an estimate for a 1989 Quebec-like event, that the global economic impact would range from $2.4 - 3.4$ trillion dollars over a year.

However, the Sun is not the only star on which flares occur. Flares can arise in nearly all main sequence stars with exterior convective envelopes, including both cool and hot stars (Pettersen, 1989), although they are more common in low-mass stars such as M dwarfs (Walkowicz et al., 2011; Davenport, 2016). Stellar flares are thought to be generated by the same process by which solar flares occur through magnetic reconnection (Davenport, 2016). X-ray observations show that young stars can produce "super-flares" (Schaefer et al., 2000), described as flares with radiative energy greater than 10^{33} erg. These young stars rotate quickly, with rotational periods of only a few days. Even in their quiescent phase, fast-rotating stars are strong X-ray sources, indicating a strong magnetic field and often showing large star spots (Pevtsov et al., 2003; Cliver et al., 2022). Thus, super-flares were thought impossible on the old, slow-rotating Sun. However, Schaefer et al. (2000) found nine super-flares with energies 10^{33-38} erg in ordinary solar-type stars by analyzing previous astronomical data. White light flares are flares in the visible continuum (Namekata et al., 2017). White light emission from a solar flare was first seen in 1859 (Carrington, 1859; Pitkin et al., 2014; Namekata et al., 2017). Several studies of white-light flares observation were carried out by Mathioudakis et al. (2003, 2006)

Due to the lack of spatial resolution on stars surfaces, the study of stellar flares is limited to photometry or spectroscopy (Walkowicz et al., 2011). Therefore, the Kepler mission made it possible to study stellar flares in detail (Van Doorsselaere et al., 2017). Several studies have been conducted to analyse Kepler data and investigate stellar flares. The stellar rotation period, starspot area, and flare energy can all be estimated using Kepler photometric observations (Cliver et al., 2022).

Walkowicz et al. (2011) discovered 373 flaring stars on 23,000 cool dwarfs in the Kepler Quarter 1 long cadence data using the photometric equivalent width (EW_{phot}), which expresses the flare energy relative to the star's quiescent luminosity. Their findings suggest that M dwarfs flare more frequently but with shorter durations than K dwarfs and

emit more energy. Pitkin et al. (2014) provided a Bayesian method for identifying stellar flares in lightcurve data. The approach is based on the general premise that flares have a distinct form, in which there is a sudden increase with a half Gaussian shape accompanied by an exponential decline.

During 120 days of Kepler observations, Maehara et al. (2012) reported 365 superflares on 148 solar-type stars (G-type main sequence stars). Shibayama et al. (2013) studied statistics of stellar super-flares. These authors discovered that for Sun-like stars (with surface temperature 5600-6000 K and slowly rotating with a period longer than 10 days), the occurrence rate of super-flares with an energy of $10^{34} - 10^{35}$ erg is once in 800-5000 yr. Shibayama et al. (2013) confirmed the previous results of Maehara et al. (2012) in that the occurrence rate (dN/dE) of super-flares versus flare energy E shows a power-law distribution with $dN/dE \propto E^{-\alpha}$, where $\alpha \sim 2$. Such occurrence rate distribution versus flare energy is roughly similar to that for solar flares.

Kepler data was used to analyse 4944 super-flares observed on 77 G-type stars by Wu et al. (2015). They found that the power-law index γ of the frequency distribution of flares, as a function of their energy, is 2.04 ± 0.17, consistent with previous studies. However, eight stars that flare frequently had γ values ranging from 1.59 ± 0.06 to 2.11 ± 0.19, suggesting that these stars may have different energy release processes. Moreover, they found that stars with shorter rotation periods tend to have larger γ values. Notsu et al. (2016) searched for super-flares on G-type main sequence stars and detected more than 1500 super-flares on 279 stars using long cadence data from Q0-Q6, and 187 super-flares on 23 stars using short cadence data from Q0-Q17. Their results show that the occurrence frequency of super-flares (dN/dE) as a function of flare energy (E) follows a power-low function with an index of -1.5. According to their findings, the frequency of super-flares depends on rotation period, with the frequency showing an increase as the rotation period decreases. Yang et al. (2017) presented a study on 540 M dwarf stars that have exhibited flare events using Kepler long-cadence data. They examined the flare activity, normalized flare energy, chromosphere activity, and starspot characteristics of M dwarf stars. They identified three phases of flare activity related to rotation periods and noted a steep rise in flare activity near M4. In addition, they found a positive correlation between starspot size and flare activity, as well as the power-law relationship between flare energy and chromospheric activity.

Using LAMOST DR5, Kepler, and K2 missions, Lu et al. (2019) conducted a statistical study on M-type stars to investigate the relationship between chromospheric activity, flares, and magnetic activity in relation to rotation periods. They found that the flare frequency is consistent with chromospheric activity indicators and that the equivalent widths of Hα and Ca II H have a significant statistical correlation with the flare amplitude. In ad-

dition, they confirmed that magnetic activity and rotation period have an effect on flares. The study also determined thresholds for flare time frequency based on specific values of Hα equivalent width and rotation period. Yang & Liu (2019a) detected 162,262 flare events on 3,420 flaring stars among 200,000 Kepler targets using long cadence mode (LC) data from data release 25 (DR25).

Notsu et al. (2019) used Gaia-DR2 stellar radius estimates from Berger et al. (2018) and updated the parameters to study the statistical properties of Kepler solar-type super-flare stars first described in their previous studies (Maehara et al., 2012, 2015, 2017; Notsu et al., 2013; Shibayama et al., 2013). Their findings indicate that, more than 40% of the (279) solar-type (G-type main sequence) super-flare stars in Shibayama et al. (2013) were classified as subgiant. Old, slowly-rotating Sun-like stars experience super-flares with energies 5×10^{34} erg once every 2000 to 3000 years, while young, fast-rotating stars experience super-flares with energies up to 10^{36} erg. In addition, the maximum super-flare energy gradually decreases as the rotation period increases. Moreover, the maximum area of starspots in the early stages of a star's life is independent of the rotation period. However, as the star ages and its rotation slows, the maximum area of starspots rapidly decreases at a certain P_{rot} value. Since the flare energy can be explained by the magnetic energy stored around starspots, these two declining trends are consistent Notsu et al. (2019).

The most recent statistical analyses of super-flares on solar-type (G-type main-sequence) stars using all of the Kepler primary mission data and the Gaia Data Release 2 catalog have been reported by Okamoto et al. (2021). They developed an improved version of the flare-detection method on their previous studies (Maehara et al., 2012, 2015; Shibayama et al., 2013), which involved the application of a high-pass filter to remove rotational variations caused by starspots. In addition, the sample biases on the frequency of super-flares were investigated, taking into consideration both gyrochronology and the completeness of the flare detection. They found 2341 super-flares on 265 solar-type stars and 26 on 15 Sun-like stars. It was estimated by Okamoto et al. (2021) that Sun-like stars with slow rotation could experience solar super-flares with energies of 10^{34} erg once every ~ 6000 years.

Davenport (2016) reported the first automated search for stellar flares using the entire Kepler data set of Data Release 24, including long and short cadence data. Approximately 3,144,487 light curves were analyzed for 207,617 distinct objects. Davenport (2016) identified 851,168 flares on 4,041 stars and revealed a strong correlation between flares and the evolution of stellar dynamos as stars age by comparing the amount of activity of the flare with stellar rotation and the Rossby number. Using thresholds for the intensity increase, the increase in the running difference and the flare duration Van Doorsselaere et al.

(2017) created a new technique for automated flare detection and applied it to Kepler's long-cadence data in quarter 15. Out of the 188,837 stars in the Kepler field of view during Q15, 16,850 flares have been found on 6662 of them.

The flare frequency distribution (FFD) is used to characterize flare energy and frequency, and it follows a power-law relation denoted by $dN/dE \propto E^{-\alpha}$ Dennis (1985). The α index constrains the magnetic activity of various stars Gao et al. (2022). Flare completeness detection and precise energy calculation are crucial during fitting FFDs, as Gao et al. (2022) stated. They corrected the completeness of flare detection based on the data from Kepler and TESS, and reprocessed the light curve uniformly, correcting the detection efficiency for each star. They improved the completeness and accuracy of the energy calculation in flare detection by injection and recovery tests into each star's original light curve for each flare event.

Kepler data analysis was not only limited to manual and automated methods, several studies have used machine learning to analyze Kepler data. Vida & Roettenbacher (2018) presented a machine-learning-based code for detecting and studying flares. The code was evaluated on two targets for Kepler and Kepler's second mission (K2) long and short cadence data, respectively. The detected flares for these two targets, as well as their energy, were found to be consistent with earlier findings. Breton et al. (2021) implemented a machine learning analysis pipeline to obtain rotation periods for Kepler targets. The algorithm was used on K and M main-sequence dwarfs studied in Santos et al. (2019), the rotation periods of a sample of 21,707 stars were computed with an accuracy of 94.2%. Machine learning techniques were applied by Ofman et al. (2022) on the TESS datasets to discover exoplanet candidates, by using Kepler data of verified exoplanets as a part of the algorithm training stage and validation. Vasilyev et al. (2022) developed a new method for identifying the true flare sources using pixel-level data. It would be helpful for automated flare detection.

The physical process that adequately describes solar flares is magnetic reconnection. The latter is rapid change of connectivity of magnetic field lines, during which magnetic energy is converted into thermal energy (heating) and kinetic energy of plasma outflows. A general framework of solar flares is well accepted (Masuda et al., 1994; Shibata et al., 1995) however questions such as: (i) how frequently and (ii) under what conditions super-flares occur still remain largely un-answered.

Our motivation is four-fold:

(i) To study the statistics of stellar super-flares on main-sequence G-type stars based on Kepler data in quarters $0 - 17$, and compare our findings with those of Okamoto et al. (2021).

(ii) To examine the effect of not including (i) the high-pass filter and (ii) analysis of sample biases on the incidence rates of super-flare, (iii) gyrochronology and (iv) the completeness of the flare detection, considered by Okamoto et al. (2021) on our results.

(iii) To investigate how the flare statistics changes on the time scale of 17 quarters. i.e. what is α power-law for data quarters $0 - 6$, $7 - 17$ and $0 - 17$.

(iv) To study the statistics of stellar super-flares on main-sequence stars of other spectral types A, F, K and M.

(v) To provide a Python script which finds super-flares automatically and only minimal human-eye analysis is needed.

Section 2.3 presents the Kepler spacecraft and its data. Section 2.4 presents the method used including the targets selection, flares detection, rotation period determination and the flare energy estimation. Section 2.5 provides the main results of this chapter. In particular we first produce results for $Q0 - Q6$, $Q7 - Q17$ and $Q0 - Q17$. Then we present a comparison with Okamoto et al. (2021). Finally, we present the result of other star spectral types. Section 2.6 closes this chapter by providing the main conclusions.

2.3 Kepler data

The Kepler spacecraft was launched in 2009 by NASA to search for exoplanets using the transit photometry method (Koch et al., 2010). This spacecraft carried a photometer telescope with an aperture of a 0.95 m and 105 deg^2 field of view (FOV) and designed to stare fixedly at one patch of sky in the constellations of Cygnus, Lyra and Draco, monitoring roughly 200000 stars continuously, to detect changes in brightness caused by planets passing in front of the stellar disc (Shibayama et al., 2013; Davenport, 2016; Yang & Liu, 2019a). The Kepler mission had two stages during its lifetime. Kepler's primary mission (K1) lasted for four years from 2009 to 2013, when the spacecraft lost two wheels of the four reaction wheels on board. Thus, Kepler's second mission (K2) started in 2014 and carried out until 2018. Due to the problem with the telescope's reaction wheels, it observed around the ecliptic plane. Targets were observed by Kepler using two cadence modes: the long cadence mode (LC) which provides one photometric data point with every 29.4 min, and the short cadence mode (SC) that provides one photometric data point with every 1 min (Pitkin et al., 2014). In order to make the Kepler solar panels always to face the Sun, Kepler rotates every 90 days. Thus Kepler's data divided into

Table 2.1: The observational period T and the start and end dates of each quarter.

Quarter	T (days)	Start Date (UT)	End Date (UT)
0	9	2009-05-02	2009-05-11
1	33	2009-05-13	2009-06-15
2	88	2009-06-20	2009-09-16
3	89	2009-09-18	2009-12-16
4	90	2009-12-19	2010-03-19
5	95	2010-03-20	2010-06-23
6	90	2010-06-24	2010-09-22
7	90	2010-09-23	2010-12-22
8	67	2011-01-06	2011-03-14
9	97	2011-03-21	2011-06-26
10	93	2011-06-27	2011-09-28
11	97	2011-09-29	2012-01-04
12	83	2012-01-05	2012-03-28
13	90	2012-03-29	2012-06-27
14	97	2012-06-28	2012-10-03
15	98	2012-10-05	2013-01-11
16	86	2013-01-12	2013-04-08
17	32	2013-04-09	2013-05-11

almost 90-day quarters from quarter 0 to 17 as an abbreviation (Q0 - Q17) except for Q0, Q1, Q8 and Q17, which covers (9, 33, 67 and 32 days respectively). The observational period with the start and end date of each quarter are shown in Table 2.1.

Since the luminosity loss caused by planetary transits is usually less than one hundredth of the star's total brightness, Kepler is intended to obtain high-precision and long-period light curves of many stars (Shibayama et al., 2013). As a result, Kepler is considered as a perfect platform to analyse stellar flares due to the significant sample size, the duration of the light curves and the photometric accuracy (Davenport, 2016).

2.4 The Method

2.4.1 Targets Selection

We carried out an automated search for super-flares on main-sequence stars type (A, F, G, K, M) based on entire Kepler data, using our bespoke Python script on long cadence data of Data Release 25 (DR 25). The script can be found at Althukair & Tsiklauri (2023a), AFD.py, v1.0.0, Zenodo, doi:10.5281/zenodo.7755912, as developed on GitHub). The parameters for all targets observed by Kepler have been taken from The NASA Exo-

planet Archive. The algorithm we used is based on the method of Maehara et al. (2012); Shibayama et al. (2013). All Kepler light curve data (2.5 TBytes) were obtained as a fits files from the Mikulski Archive for Space Telescope (MAST) with kind assistance of Deborah Kenny of STScI. Only long cadence targets were selected (with time resolution of 29.4 min). Since Kepler's optical aperture has a radius of 4-7 pixels (Bryson et al., 2010), and the pixel size of the CCDs is about four arcs (Van Cleve & Caldwell, 2009), it is thus quite possible that some targets are very close to each other on CCDs, which indicates that nearby star's brightness variations may influence the target star's flux (Shibayama et al., 2013; Yang et al., 2017; Yang & Liu, 2019a). Due to this reason we calculated the angular distance between every two stars in the entire sample, which is about 200,000 stars and excluded pairs of neighbouring stars within 12 arcsec from the analysis, to avoid detecting fake flares on the target (Shibayama et al., 2013). The overall number of samples that were excluded from the study according to this condition are about 6%. The angular distance θ between two stars was calculated by the following equation:

$$\theta = \cos^{-1}[\sin \delta_1 \sin \delta_2 + \cos \delta_1 \cos \delta_2 \cos(\alpha_1 - \alpha_2)], \qquad (2.1)$$

where α_1 , α_2 , δ_1 , δ_2 are the right ascensions and the declinations of the two stars in degree respectively. We used the Harvard Spectral classification to obtain the spectral type for each target as shown in Table 2.2. Whereas the effective temperature and radius of main-sequence stars in different spectral type are as follows: $2400 \leq T_{\text{eff}} < 3700$, and radius $\leq 0.7\ R_\odot$ for M-type, $3700 \leq T_{\text{eff}} < 5200$ and radius of $0.7 - 0.96\ R_\odot$ for K-type, for G-type we used the same effective temperature of Maehara et al. (2012); Shibayama et al. (2013) which range between $5100 \leq T_{\text{eff}} < 6000\ K$ and radius of $0.9 - 1.15\ R_\odot$, F-type has $6000 \leq T_{\text{eff}} < 7500\ K$ and radius range between $1.15 - 1.4\ R_\odot$, and A-type has $7500 \leq T_{\text{eff}} < 10,000\ K$ and radius between $1.4 - 1.8\ R_\odot$ for A-type. Due to the small number of A-type main-sequence stars that fall under these conditions, which makes the statistics inaccurate, we have not implemented radius restrictions for this spectral type. The total number of main-sequence stars is 2222, 10307, 25442, 10898, 2653 for M-, K-, G-, F-, and A-type, respectively.

2.4.2 Flare Detection Method

Kepler light curves contain two kinds of flux, the Simple Aperture Photometry flux (SAP) and the Pre–searched Conditioning SAP flux (PDCSAP), which has long term trends removed (Davenport, 2016). Figure 2.1 illustrates the difference between these two types of fluxes. All light curves were analyzed using an algorithm with a similar technique to

Table 2.2: The effective temperature T_{eff}, radius and number of stars for each spectral class.

Class	T_{eff} (K)	Radius $(R_\odot)$	N_{star}
A	7500 - 10000	1.4 - 1.8	2653
F	6000 - 7500	1.15 - 1.4	10898
G	5100 - 6000	0.9 - 1.15	25442
K	3700 - 5200	0.7 - 0.96	10307
M	2400 - 3700	$\leqslant 0.7$	2222
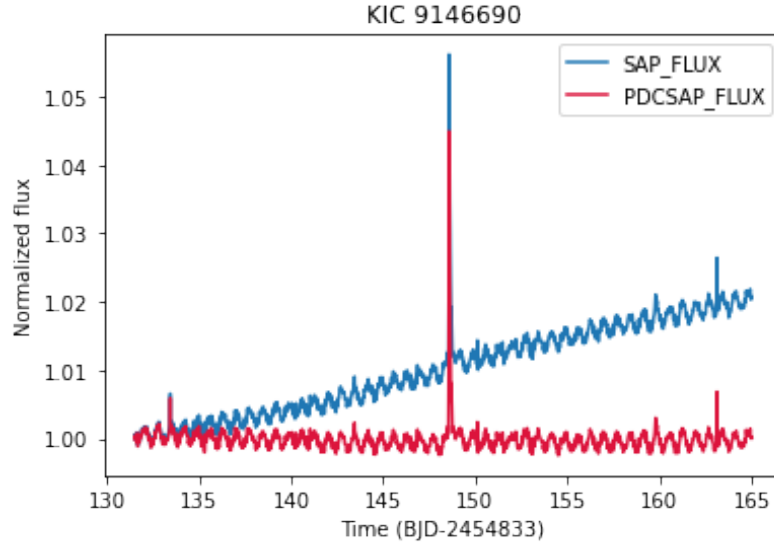
Figure 2.1: Light curve of KIC 9146690 using two types of flux. The simple aperture photometry flux SAP FLUX (blue) and the pre-searched conditioning SAP flux PDCSAP FLUX (red) which detrends the time variation.

Maehara et al. (2012); Shibayama et al. (2013).

A brief description of this method is as follows. In order to be statistically accurate, after generating light curves of all selected stars using the PDCSAP flux, we computed the distributions of brightness variation by calculating the flux difference in adjacent time intervals between every two neighbouring points of all the data points in the light curve. The purpose of this step, as clarified by Shibayama et al. (2013), is to avoid false flare detection and misdetection of short stellar brightness variation and not to overpass large flares. Then, we find such value of flux difference where the area under the distribution is equal to 1% of the entire area. This value indicates a large flux difference between two adjacent points. To enhance the the threshold, we multiplied the 1% value of the area by a factor of three. This threshold value has been chosen by Shibayama et al. (2013) based on multiple tests. Examples of some of the outputs of this method, which give the distri-

bution of brightness variations and the threshold determination, are shown in Figure 3.1. Figures 3.1(a) and 3.1(d) show light curves of KIC 4371489 at Q2 with a rotation period of 1.09 days and KIC 7354508 at Q3 with a rotation period of 17.8 days, respectively. Figures 3.1(b) and 3.1(e) show a zoom-in of these light curves, illustrating the rotational periods. Figures 3.1(c) and 3.1(f) show the distribution of brightness difference between every two neighbouring points of all the data points in the light curves of KIC 4371489 and KIC 7354508, respectively. The dashed vertical lines indicate 1% of the total area under the distribution curves. The solid vertical lines indicate the threshold values of flares detection, which is equal to three times 1% of the area under the curve. According to Shibayama et al. (2013), the detection threshold depends on the star's rotational period, and its brightness variation amplitude. For short-rotation-period stars (e.g., KIC 4371489), the distribution of brightness variations appears to extend larger than that for long-rotation-period stars (e.g., KIC 7354508). This large extension is because the difference in brightness between two successive data points is greater in stars with a short rotation periods than in stars with a long rotation periods, resulting in a greater value of flare detection threshold. Also, thresholds in stars with large brightness variation amplitudes are larger than those in stars with small brightness variation amplitudes. We defined the start time of a flare as the time when the flux difference of two consecutive points exceeds the threshold for the first time.

To determine the flare end time, we computed the three standard deviations (3σ) of the brightness variation distribution. We used the relative flux ($\Delta F / F_{\mathrm{avg}}$) as shown in Figure 2.3, where $\Delta F = F_{\mathrm{norm}}(t) - F_{\mathrm{avg}}$, with $F_{\mathrm{norm}}(t)$ being the normalized flux of the light curve, F_{avg} is the normalized flux average, and fitted a B-spline curve through three points distributed around the flare. Each of these three points is an average of five data points distributed as follows, the first average point just before the flare, the second average point around 5 hours after the flare maximum and the third average point around 8 hours after the flare maximum, see Figure 2.3 (b). The purpose of curve fitting is to remove long-term brightness variations around the flare (Shibayama et al., 2013). After subtracting the B-spline curve from the original relative flux as in Figure 2.3 (c), we define the end time of the flare as the time when the relative flux produced by the subtraction becomes less than the value of 3σ of the distribution for the first time. The flare amplitude is given by:

$$A = \frac{F_{\mathrm{max}} - F_{\mathrm{avg_2}}}{F_{\mathrm{avg}}}, \tag{2.2}$$

where F_{max} is the normalized flux at the flare peak, $F_{\mathrm{avg_2}}$ is the normalized flux average of two points distributed around the flare. The first is the average of five data points before the start of the flare and the second is the average of five data points after the end of the
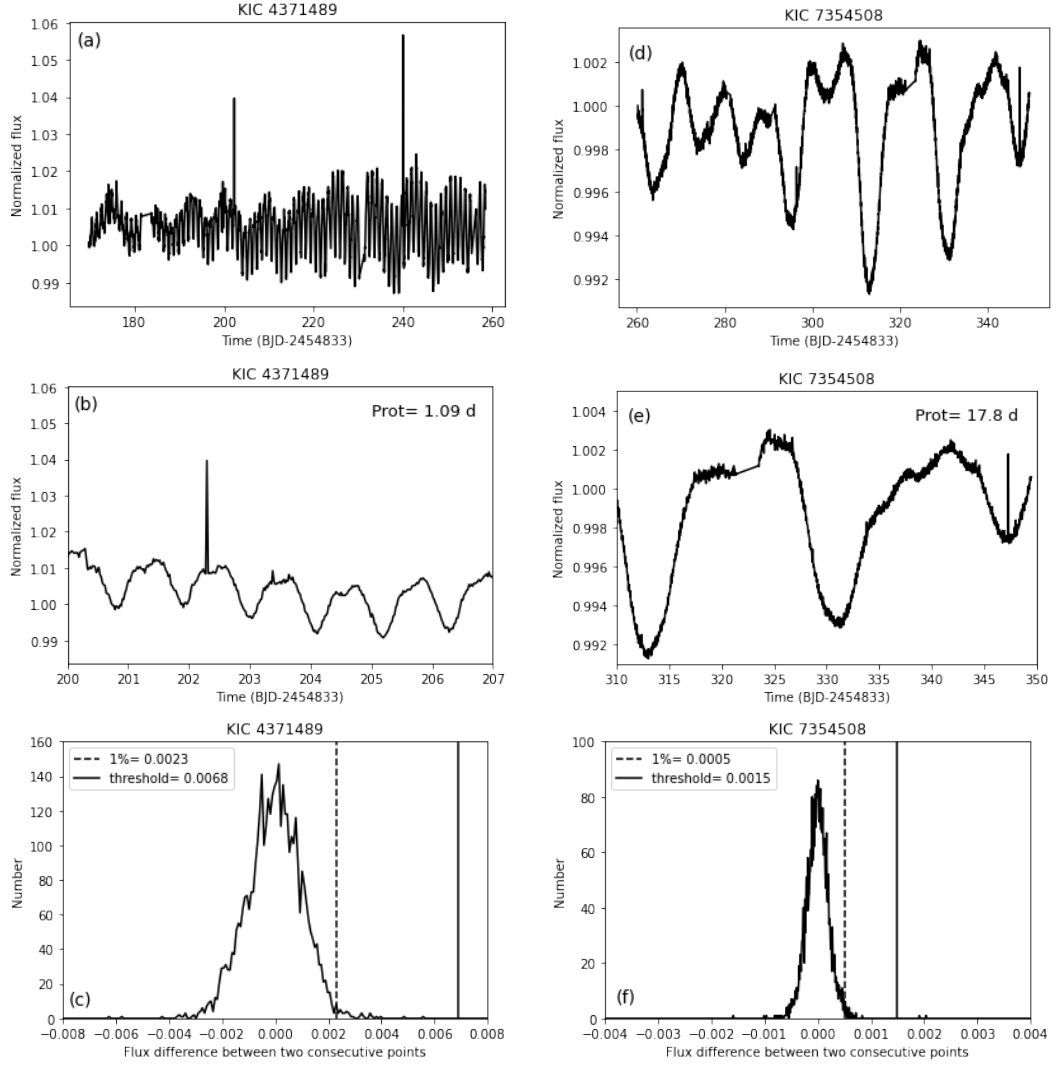
Figure 2.2: Illustrations of flares detection method used by Shibayama et al. (2013) in both fast and slowly rotating stars. (a) and (d) Show the light curve of KIC 4371489 and KIC 7354508 respectively. (b) A zoom-in into the light curve of KIC 4371489, showing a rotation period of 1.09 days. (e) A zoom-in into the light curve of KIC 7354508, showing a rotation period of 17.8 days. (c) and (f) show the distributions of brightness variation between every two neighbouring points of all the data points in the light curves of KIC 4371489 and KIC 7354508 respectively. The dashed vertical lines denote the value of 1% of the total area under the curve, and the solid vertical lines denote the flare detection threshold.

flare, F_{avg} is the normalized flux average.

After selecting the start and end time of each flare, we applied conditions to all flare candidates. These conditions are as follows: the duration of the flare should be longer than 0.05 days, which equals 72 minutes, which means at least 3 data points, and the
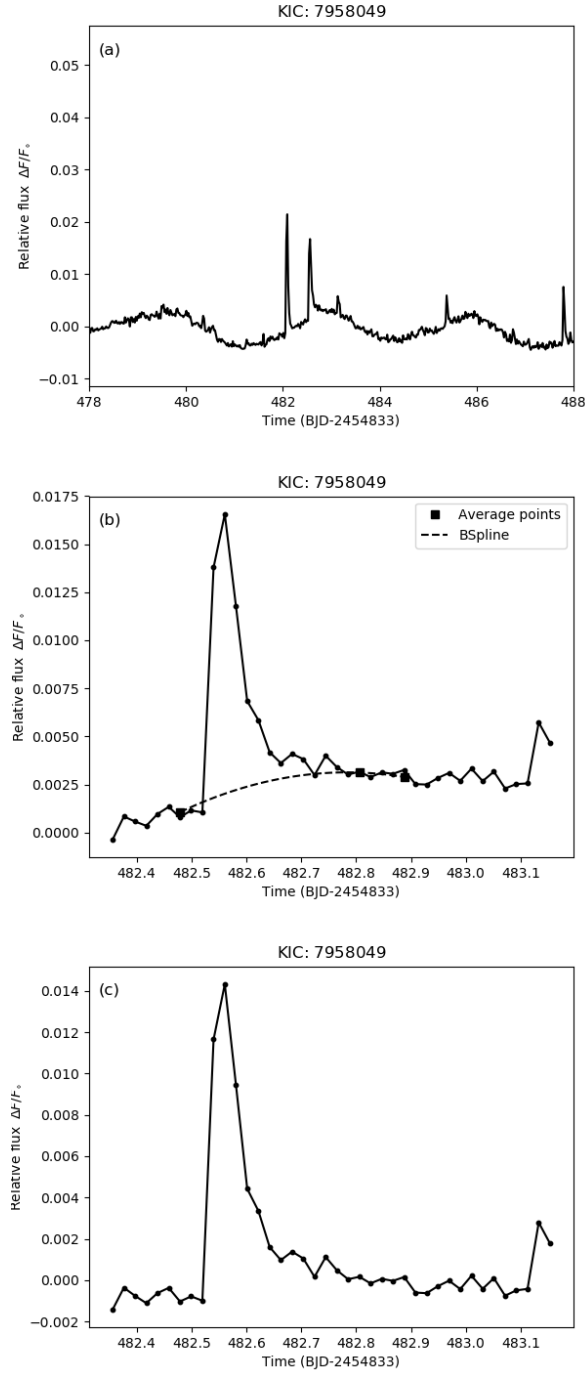
Figure 2.3: Demonstration of the removal of long-term brightness variations around the flare. (a) Part of KIC 7958049 light-curve around the flaring time (10 days of observation). (b) Fitting a B-spline curve (dashed curve) through three points around the flare (squares). The first point is an average of five data points just before the flare, the second point is an average of five data points after 5 h of the peak, and the third point is an average of five data points 8 h after the peak. All three averages are shown as squares. Note that the flux is normalized by the flux just before the flare $F_{\circ}$. (c) The produced light-curve after subtracting the B-spline curve from the relative flux.

period of the decline phase of the flare should be longer than the period of the increase phase. Only flare events that satisfy these conditions were analysed (Shibayama et al., 2013). After selecting all flares that met the conditions, we checked by eye the light curve for each flare and eliminated false flares. We have not tested the pixel level data of stars showing flares as done in Shibayama et al. (2013) for the reason of simplicity. As can be seen in our results this test omission does not alter overall findings about e.g. flare occurrence rate which us found to be similar to Shibayama et al. (2013).

2.4.3 Rotational Period Determination

We computed the brightness variation periods of light curves using the Lomb-Scargle periodogram, a common statistical method for identifying and describing periodic signals in unevenly sampled data (VanderPlas, 2018). We set the oversampling factor (number of samples per peak) in the periodogram to be five (VanderPlas, 2018) and create a Lomb-Scargle periodogram for each light curve in each quarter from Q2 to Q16 using PDCSAP flux. The light curves data of Q0, Q1 and Q17 were excluded due to their short duration similarly to McQuillan et al. (2014), as shown in Table 2.1. Further, we assigned the period corresponding to the highest power of the periodogram to be the rotation period for the Kepler ID in a certain quarter. To make the selection of star rotation period automatic rather than manual, we calculated this value with an accuracy of a day without the decimal part since fraction of a day would not significantly affect the results. For periods of less than a day, we set them to 0.5 days, and for periods of less than 0.1 days, we excluded them. According to McQuillan et al. (2014), a good sign of actual astrophysical periodicity is that it can be found in different parts of the light curve. This is because peaks caused by systematics or artefacts are less likely to appear in multiple regions of the light curve. Therefore, in order to choose the accurate rotational period, we have selected the period that is most frequent in all quarters from Q2 to Q16 for each Kepler ID. We then required that the period chosen for all quarters should be identified in at least two distinct segments, following the McQuillan et al. (2014) technique, where the segment is defined as three consecutive Kepler quarters (Q2,Q3,Q4) - (Q5,Q6,Q7) - (Q8,Q9,Q10) - (Q11,Q12,Q13) - (Q14,Q15,Q16). It is worth noting that this method has only been applied to the 1897 Kepler IDs with super-flares that will be considered in 2.5.1. Using the segments technique, we determined the rotation periods of 548 flaring stars of the Kepler sample.

In addition, we derived 222 rotation periods based on our most frequent period in all quarters. These selected periods showed significant correlation with those published in previous works. We used Excel's (CORREL) function to calculate the correlation coef-

ficient, where the correlation coefficient reaches about 0.99 for seven IDs in Yang & Liu (2019b), 0.99 for 70 IDs in Santos et al. (2021), 0.97 for 54 IDs in McQuillan et al. (2014) and 0.95 for 54 IDs in Reinhold & Gizon (2015), and 0.92 for 20 IDs in Nielsen et al. (2013).

After comparing the 770 rotation periods that we obtained from both approaches to those periods reported in McQuillan et al. (2014), we found 434 common IDs with a correlation coefficient of 0.85 between their periods. Moreover, 231 common IDs in Nielsen et al. (2013) with a correlation coefficient of 0.94 between their rotation periods. Plots of these correlations are shown in Figure 2.4, where we used *regplot* function in Seaborn Python library to plot the linear regression model fit to the data. The x-axis in both figures represents the rotation periods obtained by this chapter. The y-axis represents the periods of rotation published by McQuillan et al. (2014) in 2.4(a) and Nielsen et al. (2013) in 2.4(b). In both figures, variables change in the same direction, indicating a significant positive correlation. The rotation periods of 80 stars were obtained from other works, including 67 from McQuillan et al. (2014), 6 from Reinhold & Gizon (2015) and 7 from Santos et al. (2021), while we found that 1,047 stars have no discernible rotation period. This could be due to three reasons as mentioned by Yang et al. (2017): (i) the rotation period is longer than 90 days (a quarter), which makes it difficult (or impossible) to detect them in the star's frequency spectrum; (ii) at the accuracy level of Kepler, the light curve has a small amplitude due to the inclination angle and low activity level; (iii) fast-rotating stars have spots in the poles (Schüssler & Solanki, 1992), making detecting light variation through rotation hard. The entire results on rotational period determination can be found at https://github.com/akthukair/AFD.

2.4.4 Flare Energy Estimation

We determined the total energy of each flare from the star luminosity, flare amplitude and its duration, following Shibayama et al. (2013); Yang et al. (2017).

The star luminosity L_{star}, which is the total energy that a star produces in one second, depends on the radius of the star R and the surface temperature T_{eff}. This is given by the equation:

$$L_{\mathrm{star}} = \sigma_{\mathrm{SB}} T_{\mathrm{eff}}^4 4\pi R^2, \tag{2.3}$$

where σ_{SB} is the Stefan-Boltzmann constant, $4\pi R^2$ is the entire surface area of the star. Hawley & Fisher (1992); Kretzschmar (2011) found that the continuum emission released by white-light flare is compatible with blackbody radiation at about 9000 K. Therefore, in this chapter T_{flare} assumed to be 9000 K according to Shibayama et al. (2013); Yang et al.
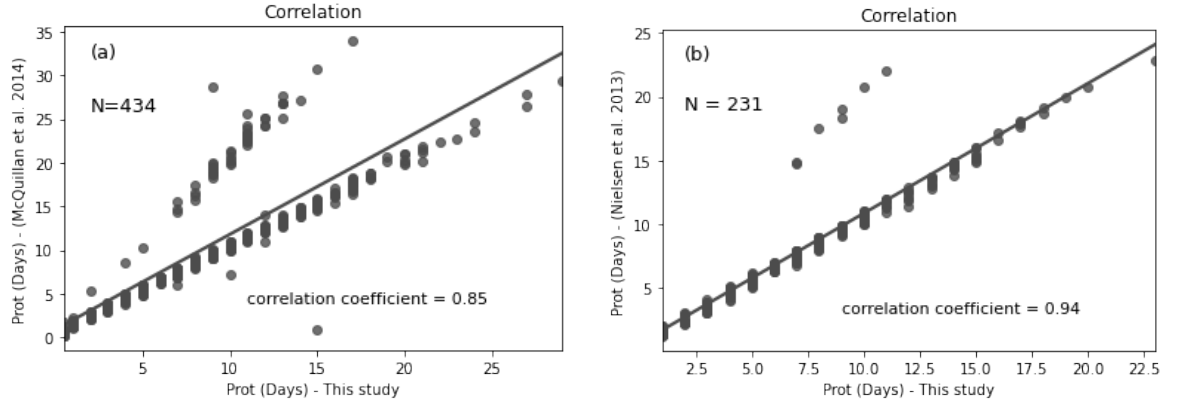
Figure 2.4: The comparisons of the periods determined in this chapter to those detected by McQuillan et al. (2014) and Nielsen et al. (2013) in (a) and (b), respectively, reveal a strong positive correlation in which both variables vary in the same direction. The x-axis shows the rotation periods found in this chapter, and the y-axis displays the rotational periods provided by McQuillan et al. (2014) and Nielsen et al. (2013). N represents the number of stars in each comparison. The correlation coefficient between our periods and McQuillan et al. (2014) is 0.85, while it is 0.94 for Nielsen et al. (2013)

(2017); Günther et al. (2020) and the luminosity for a blackbody emitting star is giving by:

$$L_{\text{flare}}(t) = \sigma_{\text{SB}} T_{\text{flare}}^4 A_{\text{flare}}, \tag{2.4}$$

where A_{flare} is the area of the flare and can be estimated by the equation:

$$A_{\text{flare}}(t) = C_{\text{flare}}(t)\pi R^2 \frac{\int R_\lambda B_\lambda(T_{\text{eff}})d\lambda}{\int R_\lambda B_\lambda(T_{\text{flare}})d\lambda}, \tag{2.5}$$

where C_{flare} is the flare amplitude for the relative flux, R_λ is the response function of Kepler instrument (Caldwell et al., 2010). The photometer in Kepler use one broad bandpass range from 420 to 900 nm. $B_\lambda(T)$ is the Plank function at a given wavelength and it is given by:

$$B_\lambda(T) = \frac{2hc^2/\lambda^5}{e^{hc/\lambda kT} - 1}, \tag{2.6}$$

where h is the Planck's constant, c is the speed of light, T is the temperature of the black body, k is the Boltzmann's constant.

L_{flare} can be calculated by substituting Equation (2.5) into (2.4). Since $C_{\text{flare}}(t)$ is a function of time, $L_{\text{flare}}(t)$ is also a function of time. Therefore, the total energy of the flare is

the integral of L_{flare} over the flare duration, and is given by :

$$E_{\text{flare}} = \int_{t_{\text{start}}}^{t_{\text{end}}} L_{\text{flare}}(t)dt. \tag{2.7}$$

2.5 The Results

This section presents the main results of this chapter.

2.5.1 Super Flares on G-type Dwarfs

Super flares on G-type dwarfs in Q0-Q6

During 494 days of continuous observation of 25,440 G-type dwarfs, searching for super-flares using Kepler long cadence data, we found 1,298 super-flares on 588 G-type dwarfs. Among them were 229 super-flares on 132 slowly rotating stars. As for the Sun-like stars, which are known as stars with a surface temperature of $5600K \leqslant T_{\text{eff}} < 6000K$, a surface gravity of $\log g > 4.0$, and a rotational period exceeding ten days (Shibayama et al., 2013), we found 151 super-flares on 93 Sun-like stars. The number of detected super-flares in this chapter is less by 16% than the 1547 super-flares found in Shibayama et al. (2013). In contrast, the number of super-flare stars in this chapter is approximately 2 times the 279 super-flare stars in Shibayama et al. (2013). Since interstellar activity varies, some stars have shown more than one super-flare, while others have shown only one. In comparison, we found that 161 stars out of 588 have more than one super-flare, while 427 stars showed only one super-flare. The number of Sun-like stars that exhibit more than one super-flare is 18 out of 93, while 75 Sun-like stars showed only one super-flare.

The most energetic super-flare found had an energy of 2.94×10^{36} erg, an amplitude of 0.35 and lasted for about 0.08 days. Figure 2.5 shows four light curves with a 30-days observation period of the most energetic super-flares that we found with their Kepler ID (left panels). The right panels display a zoom-in of these super-flares, showing their respective energy and their peak time. The black squares on the light curves indicate the data points of the super-flare from the time it starts until it ends.

In Figure 2.6 are six log-log scale histograms demonstrating the frequency distribution of super-flares in quarters 0 to 6. We estimated the error bar for each bin using the equation:

$$\text{err} = \sqrt{\sum w^2}, \tag{2.8}$$

where w represents the individual weights of the events that belong in that bin. As a result, when the number of the event in the bin is insufficient, the error bars in statistics are large (Shibayama et al., 2013).

Figure 2.6(a) represents the distribution of the number of observed super-flares per observed flare peak amplitude. The number of observed super-flares is 1298, and the measured amplitude range is approximately between 8×10^{-4} to 3×10^{-1}. Figures 2.6(b,c
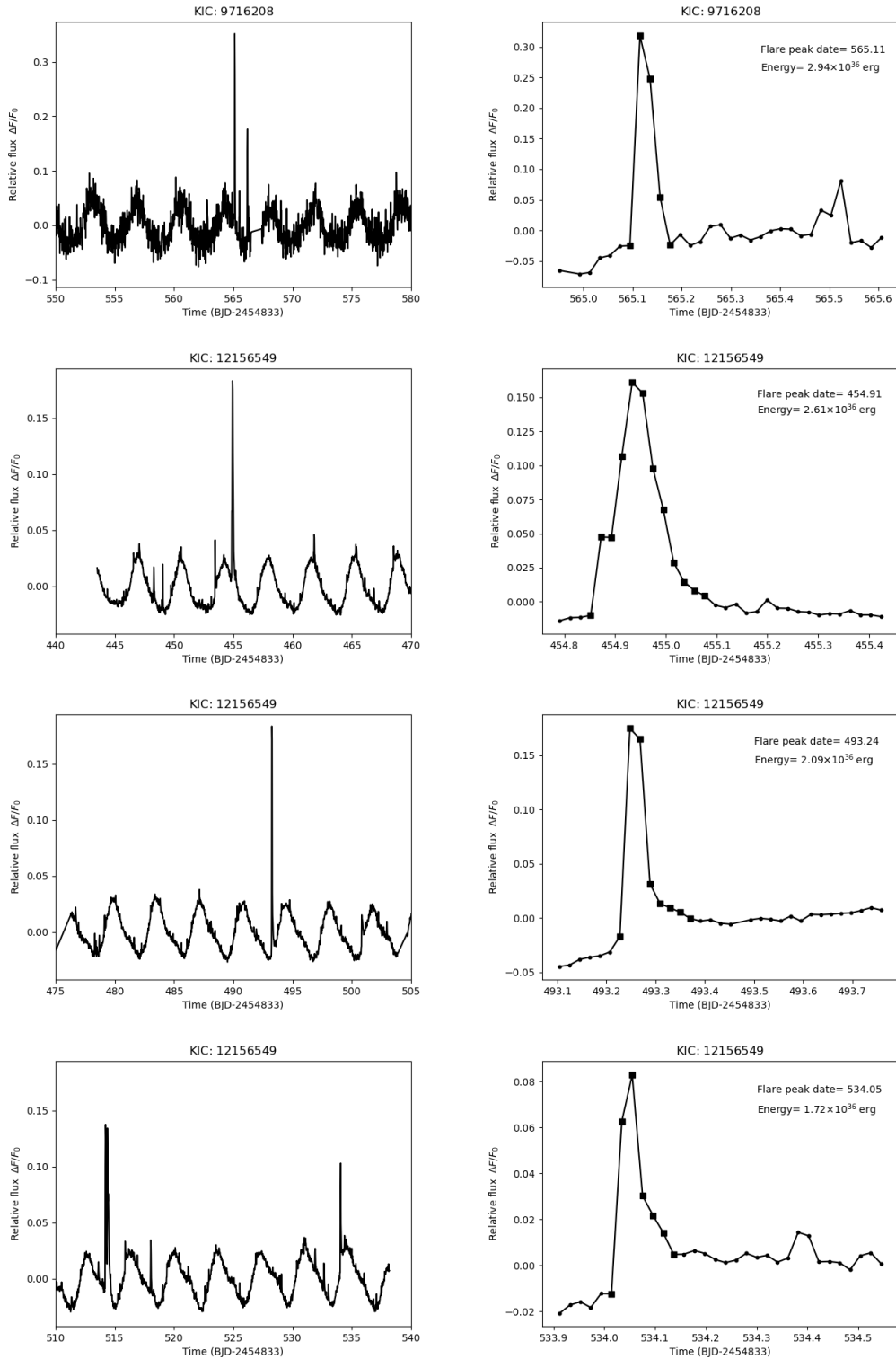
Figure 2.5: Four of the most energetic super-flares detected during quarter 0 to 6. The left panel shows the light curves of these super-flares over a period of 30 days. The super-flares that occurred on these light curves are enlarged in the right panels. The super-flare energy and peak date are displayed in the upper right corner. The black squares in the right panel correspond to the data points for the super-flares from beginning to end.
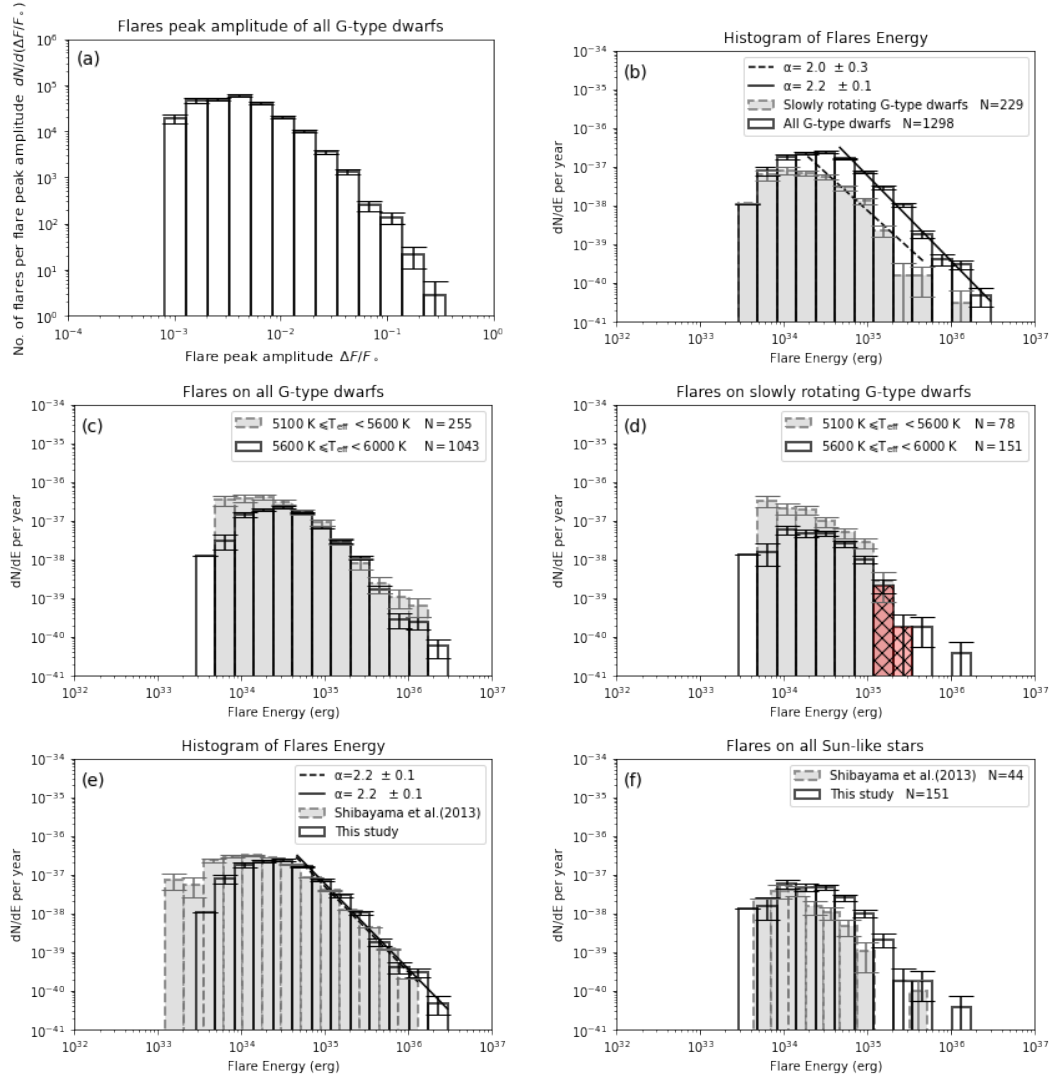
Figure 2.6: Log-log scale histograms showing the frequency distribution of super-flares on G-type dwarfs ($5100K \leq T_{\text{eff}} < 6000K$, and $\log g > 4.0$) in Q0-Q6. The error bar for each bin was calculated by taking the square root of the sum of the squared weights in that bin. (a) Distribution of the number of observed super-flares per recorded flare peak amplitude. (b) Distribution of flare frequency as a function of flare energy. The distributions of all stars and slowly rotating stars are shown by solid and dashed lines, respectively. All G-type dwarfs and slowly rotating G-type dwarfs have power-law indices of 2.2 and 2.0, respectively. (c) Distribution of flare frequency as a function of flare energy of all cool stars ($5100K \leq T_{\text{eff}} < 5600K$, grey-dashed histogram), and all hot stars ($5600K \leq T_{\text{eff}} < 6000K$ white-solid histogram). (d) The same as (c), but for flares on slowly rotating stars $P_{\text{rot}} > 10$ days. The average energy of the two red bins were used to calculate the occurrence frequency of super flares with energy of 2.11×10^{35} erg. (e) and (f) are the comparisons between the findings of this chapter and those of Shibayama et al. (2013) on all G-type dawrfs and Sun-like stars, respectively.

and d) show the super-flares frequency distributions as a function of the flare energy. However, each histogram has a different collection of super-flare stars according to the purpose of the comparison. The x-axis indicates the energy of super-flares in erg, and the y-axis represents the number of super-flares per star per year per unit energy. Figure 2.6(b) show a comparison between frequency distributions of super-flares on all G-type dwarfs (white-solid histogram) and slowly rotating G-type dwarfs with $P_{\text{rot}} > 10$ days (grey-dashed histogram). The number of detected super flares is 1298 for all G-type dwarfs and 229 for slowly rotating G-type dwarfs. Since the y-axis is the number of super-flares per star per year per unit energy, we determine the weight for each bin using:

$$w = \frac{3.16 \times 10^7}{N_{\text{os}} \times D \times E}, \tag{2.9}$$

where N_{os} is the number of observed stars, see table 2.3, D is the duration of the observation period in seconds, and E is the super-flare energy that belongs to that bin. Due to the lack of rotation period data, table 2.3 was produced based on an estimate using table 6 from Shibayama et al. (2013), where we calculated the ratio of the number of cool, slowly-rotating stars and hot, slowly-rotating stars to the number of observed stars in Shibayama et al. (2013), and similarly for the fast-rotating stars. We then applied i.e. extrapolated these ratios to our data to estimate the number of fast and slowly rotating stars relative to their effective temperature. When comparing the distribution of super-flares on all G-type dwarfs and super-flares on slowly rotating G-type dwarfs, we can confirm that the occurrence frequency of super-flares on all G-type dwarfs is higher than the occurrence frequency of super-flares on slowly rotating G-type dwarfs. Furthermore, it is evident from the two fitted straight lines, (solid line) for all G-type dwarfs and (dashed line) for all slowly rotating G-type dwarfs, that the frequency distributions of super-flares on all G-type dwarfs and slowly rotating G-type dwarfs, follow a power-law relation given by:

$$\frac{dN}{dE} \propto E^{-\alpha}, \tag{2.10}$$

where the index $\alpha \simeq 2.2 \pm 0.1$ for all G-type dwarfs and $\alpha \simeq 2.0 \pm 0.3$ for all slowly rotating G-type dwarfs. We note that this result is similar to that of Shibayama et al. (2013). Figure 2.6(c) show the distribution of super-flares as a function of energy on all cool G-type dwarf with $5100K \leqslant T_{\text{eff}} < 5600K$ (grey-dashed histogram) with 255 observed super-flares, and all hot G-type dwarfs with $5600K \leqslant T_{\text{eff}} < 6000K$ (white-solid histogram) with 1043 observed super-flares. Figure 2.6(d) the same as 2.6(c) but for slowly rotating G-type dwarfs with rotation period more than 10 days. The number of observed super-flares for cool slowly rotating G-type dwarfs is 78, and 151 for hot

Table 2.3: The number of observed G-type stars N_{os} distributed according to their effective temperature T_{eff} and rotational period P_{rot}.

T_{eff}	N_{os}	Slow	Fast
K		$P_{\mathrm{rot}} > 10$ d	$P_{\mathrm{rot}} \leq 10$ d
5100-5600	3839	3518	321
5600-6000	21603	19160	2443
Total	25442	22678	2764

slowly rotating G-type dwarfs (Sun-like stars). From the two figures, we find that the frequency of super-flares is higher in cool G-type dwarfs than in hot G-type dwarfs, again confirming the previous results of Maehara et al. (2012); Shibayama et al. (2013). Note that the difference in the occurrence rate of super-flares between the cool and hot stars in this chapter is not as large as in Maehara et al. (2012); Shibayama et al. (2013). We can explain this by noting that our sample's number of cool stars constitutes approximately 15.1% of the total number of the sample while hot stars make up 84.9% of the total number of the sample, see table 2.3. In contrast, in Shibayama et al. (2013), cool stars make up about 48.7% of the total number of the sample, and hot stars constitute 51.3% of the total number of the sample. In addition, if we compare the number of superstars relative to the observed stars, we find that this rate is higher in cool stars than in hot ones, see columns 5, 8 and 13 in table 2.4.

We calculated the occurrence frequency rate of super-flares from the number of observed super-flares N_{f}, the number of observed stars N_{os} and the observation duration D (Maehara et al., 2012; Shibayama et al., 2013). The super-flares energy distribution in Q0-Q6, which ranges from 2.84×10^{33} erg to 2.94×10^{36} erg, varies from Q7-Q17 and Q0-Q17, which ranges from 2×10^{33} erg to 1.42×10^{38} erg, resulting in a different energy bins distribution. Therefore, in order for the energy used to derive the occurrence frequency rate of super-flares to be close for each section of the analysis (Q0-Q6, Q7-Q17 and Q0-Q17), we used the average energy of the two red bins in 2.6(d), which equals 2.11×10^{35} erg and is close to the energy 2.26×10^{35} erg that used in Q7-Q17 and Q0-Q17, red bins in Figures 2.7(d) and 2.8(d). As a result, the rate of super-flares incidence with energy of 2.11×10^{35} erg is 2.46×10^{-4} flares per year per star, corresponding to a super-flare occurring on a star once every 4070 years. This result is within about 80% of the occurrence rate of super-flares with energy of 10^{35} erg found by Shibayama et al. (2013), which equals to one super-flare in 5000 years for each star. Figures 2.6(e) and 2.6(f) show a comparison between the results of this chapter (solid-white-histogram) and Shibayama et al. (2013) study (grey-dashed-histogram). Figure 2.6(e) depicts the frequency distribution of super-flares energy for all G-type dwarfs, $dN/dE \propto E^{-\alpha}$, where $\alpha \sim 2.2$ in

Table 2.4: The number of super-flares and super-flare stars on G-type dwarfs.

Quarters	T_{eff}	Slow			Fast			Unknown P_{rot}		Total		
		N_{f}	N_{fstar}	$N_{\text{f}}/N_{\text{os}}$	N_{f}	N_{fstar}	$N_{\text{f}}/N_{\text{os}}$	N_{f}	N_{fstar}	N_{f}	N_{fstar}	$N_{\text{f}}/N_{\text{os}}$
$0-6$	$5100-5600$	78	39	0.02	141	35	0.43	36	30	255	104	0.07
	$5600-6000$	151	93	0.01	698	203	0.29	194	188	1043	484	0.05
$7-17$	$5100-5600$	195	88	0.06	303	59	0.94	144	116	642	263	0.17
	$5600-6000$	288	180	0.015	1552	361	0.64	857	735	2697	1276	0.12
$0-17$	$5100-5600$	273	112	0.08	444	65	1.38	180	141	897	319	0.23
	$5600-6000$	439	243	0.023	2250	653	0.92	1051	906	3740	1578	0.17

Note: N_{f} the number of super-flares, N_{fstar} the number of super-flare stars and $N_{\text{f}}/N_{\text{os}}$ the ratio of the number of super-flares to the number of observed stars N_{os}. N_{os} can be found in table 2.3.

each of the two studies. 2.6(f) show the same comparison but for Sun-like stars with 151 super-flares in this chapter and 44 super-flares in Shibayama et al. (2013). Note from the two comparisons that the estimated energy of super-flares in this chapter is higher than that of Shibayama et al. (2013). Our justification for this is related to the differences in the Kepler Data Release between DR 9 and DR 25 used in Shibayama et al. (2013) and this chapter, respectively. Since the Kepler pipeline was updated between DR 9 and DR 25, PDC light curves for each target may also be updated. Also, the previous work may have used a slightly different parameters since the effective temperature and radius of some Kepler targets have been updated since then, resulting in different Kepler IDs for each spectral type. Another factor that may affect the energy value is that in this chapter, we used the flux difference rather than the flux to determine the start time of the flare. This can result in an extra data point between the flare's start and end times, resulting in higher energy. To find how our method affects the energy calculation results, we run the script on 279 flare stars from Shibayama et al. (2013) in order to compare the energy results drived form the script with those in Shibayama et al. (2013). We found 503 common super-flares with the same start-time of the flare between Shibayama et al. (2013) and our script result. Then we calculated correlation coefficient between the energy values and we observed an energy increase for our study, with a correlation coefficient of 0.66 between the two energies. Such small correlation coefficient points to a sizeable difference the flare energy estimates between this chapter and Shibayama et al. (2013), for the reasons listed above.

Super flares on G-type dwarfs in Q7-Q17

We detected 3339 super-flares on 1539 G-type dwarfs during the course of 930 days of continuous monitoring. 483 super-flares on 268 slowly rotating stars are among them. In the case of Sun-like stars, we found 288 super-flares on 180 of them. According to our findings, 318 G-type dwarfs out of 1539 exhibit several super-flares whereas 1221 show only one super-flare. A total of 38 out of 180 Sun-like stars have several super-flares, and 142 Sun-like stars have just one super-flare. The most powerful super-flare discov-

ered during this period had an energy of 1.42×10^{38} erg, an amplitude of 22.75, and a duration of 0.06 days. Figure 2.7 depicts four log-log scale histograms displaying the frequency distribution of super-flares in quarters 7 to 17, similar to Figure 2.6, but without the comparisons in 2.6(e) and 2.6(f). The distribution of the number of observed super-flares per observed flare peak amplitude is shown in Figure 2.7(a). The total number of super-flares detected is 3339, with amplitudes ranging from 7.5×10^{-4} to 35. Figures 2.7(b,c and d) have similar format as Figures 2.6(b,c and d). A comparison of super-flare frequency distributions on all G-type dwarfs (white-solid histogram) and slowly rotating G-type dwarfs (grey-dashed histogram) is shown in Figure 2.7(b). The power-law index for super-flare frequency distributions on all G-type dwarfs $\alpha \simeq 2.2 \pm 0.1$ and for slowly rotating G-type dwarfs $\alpha \simeq 2.1 \pm 0.4$. Figures 2.7(c) and 2.7(d) show the distribution of super-flares as a function of flare's energy according to the effective temperature of the star for all G-type dwarfs and slowly rotating G-type dwarfs respectively. where the number of detected super-flares is 642 super-flares on all cool G-type dwarf (grey-dashed histogram) and 2697 super-flares on all hot G-type dwarfs (white-solid histogram) in 2.7(c) and 195 super-flares on cool slowly rotating G-type dwarfs (grey-dashed histogram) and 288 super-flares on hot slowly rotating G-type dwarfs (white-solid histogram) in 2.7(d). The red bin in 2.7(d) shows that the occurrence frequency rate of super-flares with energy of 2.26×10^{35} erg is 1.31×10^{-4} flares per year per star, corresponding to a super-flare occurring on a star once every 7640 years. We note that this value is somewhat larger that similar results for Q0-Q6 and Q0-Q17.

Super flares on G-type dwarfs in Q0-Q17

Combining the two previous observations, we find that during 1424 days of continuous monitoring, we found 4637 super-flares on 1896 G-type dwarfs. Among them are 712 super-flares on 355 slowly rotating stars. We discovered 439 super-flares on 243 of the Sun-like stars. Our findings suggest that 397 stars out of 1896 G-type dwarfs have more than one super-flares, whereas 1499 stars have only one super-flare. A total of 55 out of 243 Sun-like stars have several super-flares, whereas 188 Sun-like stars have just one super-flare. Table 2.5 lists some super-flares stars with their parameters and the number of occurred super-flare $N_{\rm f}$. The entire results can be found at https://github.com/akthukair/AFD. Figure 2.8 similar to Figure 2.7 shows four log-log scale histograms of the frequency distribution of super-flares as a function of flare energy in quarters 0 to 17. Figure 2.8(a) shows the distribution of the number of observed super-flares per observed flare peak amplitude. The amplitude of the 4,637 detected super-flares ranges between 7.5×10^{-4} and 35.6. Figure 2.8(b, c, and d) format
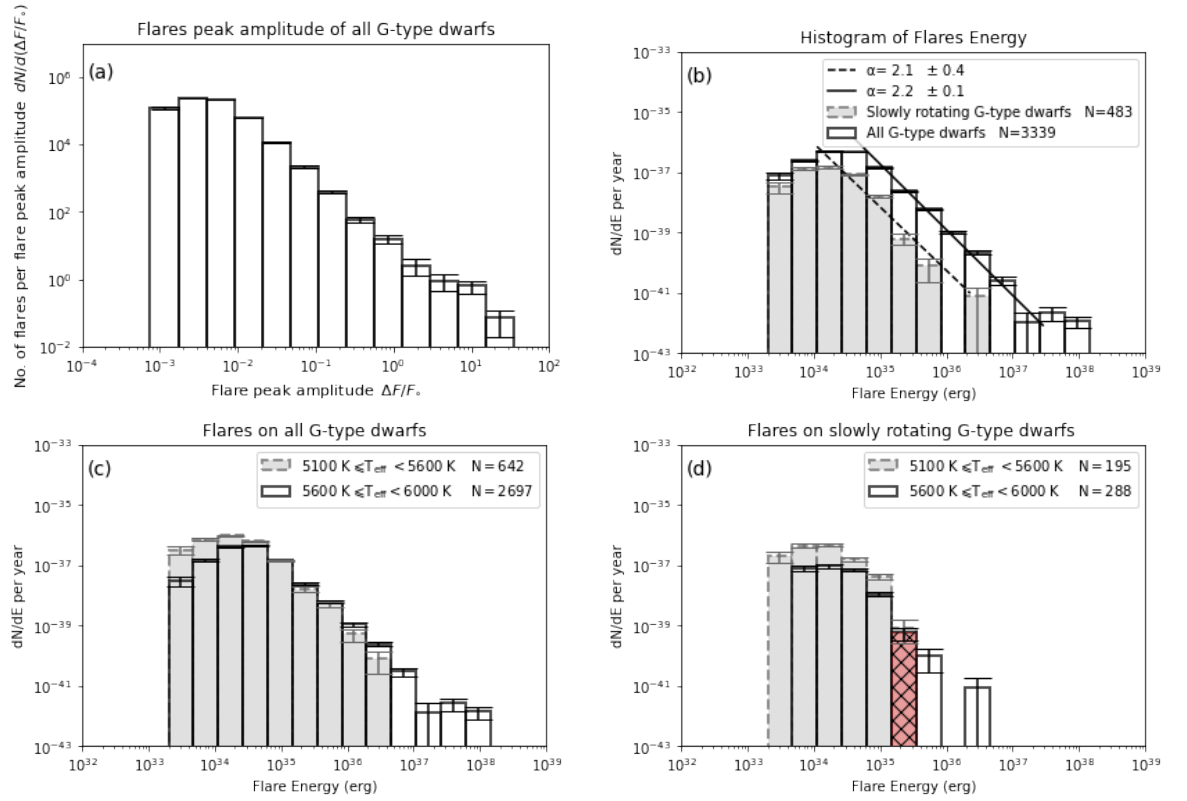
Figure 2.7: The same as in Figure 2.6 (a-d) but for Q7-Q17 data. The flare frequency distribution in (b) for all G-type dwarfs and slowly rotating G-type dwarfs have power-law indices of 2.2 and 2.1, respectively. The red bin in (d) was used to calculate the occurrence frequency of super flares with energy of 2.26×10^{35} erg.
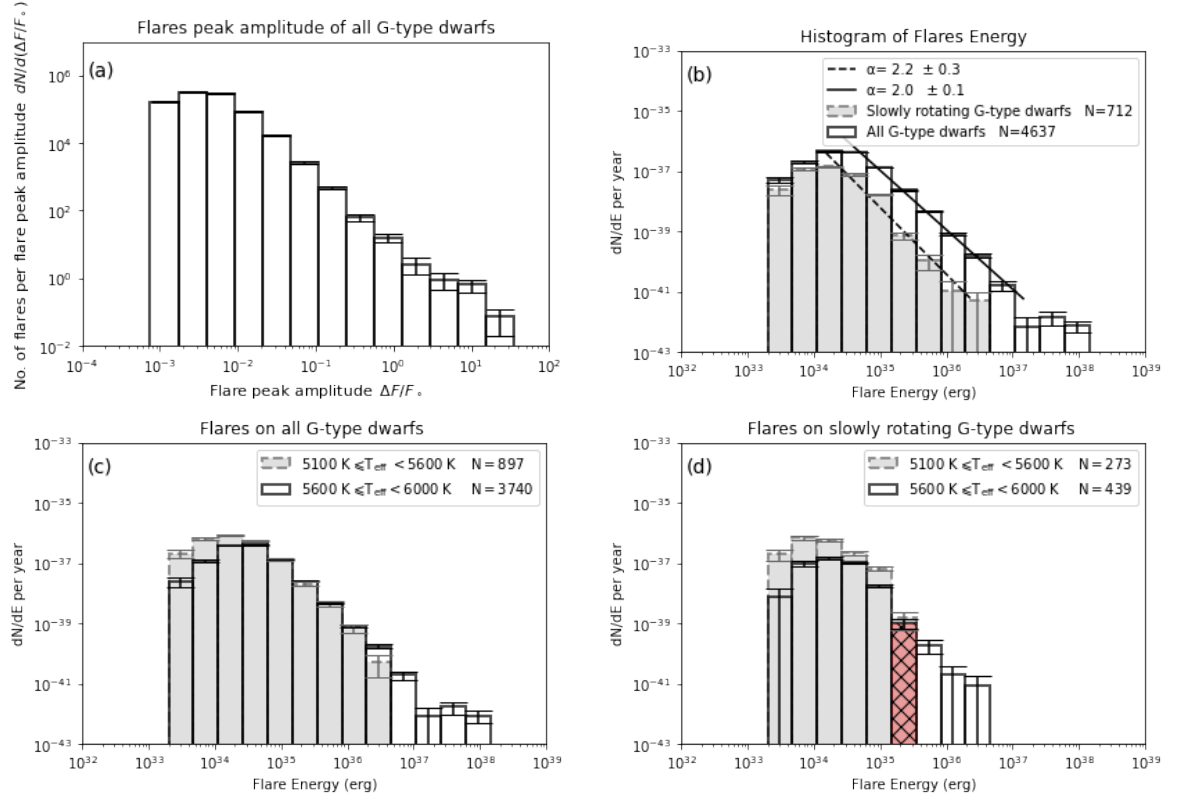
Figure 2.8: The same as in Figures 2.6 (a-d) and 2.7 but for Q0-Q17 data. The flare frequency distribution in (b) for all G-type dwarfs and slowly rotating G-type dwarfs have power-law indices of 2.0 and 2.2, respectively. The red bin in (d) was used to calculate the occurrence frequency of super flares with energy of 2.26×10^{35} erg.

is similar to Figure 2.7(b, c and d). Figure 2.8(b) compares the frequency distributions of super-flares on all G-type dwarfs (white-solid histogram) and slowly rotating G-type dwarfs (grey-dashed histogram). Super-flare frequency distributions on all G-type dwarfs have a power-law index of $\alpha \simeq 2.0 \pm 0.1$, while slowly rotating G-type dwarfs have a power-law index of $\alpha \simeq 2.2 \pm 0.3$. A comparison of the distribution of super-flares as a function of flare energy for all G-type dwarfs and slowly rotating G-type dwarfs, according to the effective temperature of the star are shown in Figures 2.8(c) and (d). In Figure 2.8(c), there are 897 super-flares on all cool G-type dwarfs (grey-dashed histogram) and 3740 super-flares on all hot G-type dwarfs (white-solid histogram), 273 super-flares on cool slowly rotating G-type dwarfs (grey-dashed histogram) and 439 super-flares on hot slowly rotating G-type dwarfs (white solid histogram) (d). The occurrence frequency rate of super-flares with energy equal to 2.26×10^{35} erg is 2.29×10^{-4} flares per year per star, corresponding to a super-flare occurring on a star once every 4360 years, as shown in the red bin in Figure 2.8(d).

Table 2.5: The parameters of super-flare stars (G-type) with the number of flares N_f.

Kepler ID	T_eff (K)	log g	Radius ($R_\odot$)	P_rot (day)	N_f
1718360	5908	4.44	1.00	2	5
2302288	5904	4.45	1.01	9	1
2308761	5780	4.44	1.00	1	25
2445975	5780	4.44	1.00	1	9
2837133	5361	4.33	1.06	23	1
3852796	5650	4.37	0.98	11	2
3858729	5780	4.44	1.00	4	11
3869649	5525	4.46	0.90	1	13
4137840	5830	4.50	0.93	2	9
4346178	5392	4.31	1.09	34	3
4749912	5734	4.26	1.13	5	12
5105805	5849	4.52	0.92	13	2
5202404	5999	4.35	1.07	4	31
6223256	5951	4.30	1.11	2	38
6780893	5462	4.40	0.93	4	15
7958049	5802	4.38	0.94	2	97
8357647	5776	4.36	0.96	5	2
9390942	5999	4.49	0.96	8	1
9827094	5790	4.28	1.09	3	21
10518610	5530	4.43	1.02	18	1
10922936	5325	4.43	0.92	15	5
11809362	5216	4.45	0.90	15	1
11913716	5875	4.48	0.98	12	1
12266582	5638	4.39	0.93	6	4
12405306	5911	4.50	0.94	10	1

Note: The full version of the table is available at https://github.com/akthukair/AFD

Comparison with Okamoto et al. (2021)

In section 2.5.1, we compared our results with those of Shibayama et al. (2013) since that section discusses the super-flares statistical analysis in (Q0-Q6) only as in Shibayama et al. (2013) study. Here we compared our findings to Okamoto et al. (2021), who used the complete Kepler primary mission data set and the Gaia Data Release 2 catalog to conduct the most recent statistical analyses of super-flares on solar-type (G-type main-sequence) stars.

(i) The sample size used to search for super-flare differs between the two studies. Okamoto et al. (2021) limit the study to 11,601 stars whose brightness variation amplitude and rotation period values were reported by McQuillan et al. (2014). In this chapter, our sample size is more than two times larger than Okamoto et al. (2021) (25442 G-type main-sequence stars).

(ii) We both used the same method used in previous studies Maehara et al. (2012, 2015); Shibayama et al. (2013) to detect super flares, except that Okamoto et al. (2021) improved the technique by developing an improved version of the flare-detection method, in which a high-pass filter was used to remove rotational variations caused by starspots. Furthermore, the sample biases on the frequency of super-flares were examined, taking both gyrochronology and the completeness of the flare detection into account. Our method does not include these improvements.

(iii) We found 4637 super-flares on 1896 G-type dwarfs. The number of super-flares and super-flare stars is ~ 2 and ~ 7 times larger than the 2341 super-flares and 265 super-flare stars in Okamoto et al. (2021), respectively. In addition, we found 439 superflares on 243 Sun-like stars based on Shibayama et al. (2013) definition for the Sun-like stars ($5600K \leqslant T_{\text{eff}} < 6000K$, $\log g > 4.0$, and $P_{\text{rot}} > 10$ days). If we consider the rotation period range in Okamoto et al. (2021) for the Sun-like stars ($P_{\text{rot}} = 20 - 40$ days), the number of flares would be reduced to 51 super-flares on 38 Sun-like stars. This is approximately twice the number of super-flares and Sun-like stars that were discovered in Okamoto et al. (2021), with 26 super-flares on 15 Sun-like stars.

(iv) Our result includes 183 flare events on 41 G-type dwarfs, similar to those observed by Okamoto et al. (2021). Table 2.7 presents a comparison of these events between the two studies. Showing the parameters for each Kepler ID, the flare peak date and its energy. This result constitute 3.95% and 7.82% of the total flares detected in our work and Okamoto et al. (2021), respectively. This low percentage in similar events

is due to the different Kepler IDs in the samples used in the two studies. Since the effective temperature and stellar radius values in Okamoto et al. (2021) were taken from Gaia-DR2 in Berger et al. (2018), resulting in different Kepler IDs for G-type main-sequence stars. We observed an increase in the flare energy estimate of our study compared to Okamoto et al. (2021), with a correlation coefficient of 0.91 between the two energies.

(v) We calculated α index for the flare frequency distributions as a function of the flare energy ($dN/dE \propto E^{-\alpha}$) for different range of P_{rot} (< 5 days, 5-10 days, 10-20 days an 20-40 days) in two effective temperatures ranges (5100-5600 K and 5600-6000 K) as shown in Figure 2.9 and compared our results with those of Okamoto et al. (2021) as shown in table 2.6. The results are very similar, with α indexes around -2, confirming Okamoto et al. (2021) previous finding, which is also aligns with earlier research on super-flares on solar-type stars (Shibata et al., 2013; Shibayama et al., 2013; Maehara et al., 2015). From this similarity, we believe that the effects applied in Okamoto et al. (2021) by applying a high-pass filter and examining the sample biases on super-flare occurrence rates considering gyrochronology and the completeness of flare detection have no significant affect on our final results.

(vi) We used a different stellar parameters catalog (q1_q17_dr25_ stellar catalog) however, we obtained similar results. Different stellar properties in the Gaia catalog, especially for radius, did not significantly affect our results, as shown in Table 2.7, as the correlation coefficient between energies in the two data sets $\simeq 0.91$.

Table 2.6: Comparison of the α index for the flare frequency distributions as a function of the flare energy ($dN/dE \propto E^{-\alpha}$) for each P_{rot} range.

P_{rot}	$T_{\text{eff}} = 5100 - 5600$		$T_{\text{eff}} = 5600 - 6000$	
	This work	Okamoto et al. (2021)	This work	Okamoto et al. (2021)
< 5 d	-1.6 ± 0.1	-1.5 ± 0.1	-1.8 ± 0.1	-1.8 ± 0.1
$5 - 10$ d	-2.3 ± 0.4	-1.9 ± 0.2	-2.0 ± 0.1	-2.1 ± 0.1
$10 - 20$ d	-2.2 ± 0.4	-2.2 ± 0.2	-2.3 ± 0.2	-2.2 ± 0.1
$20 - 40$ d	-1.9 ± 0.3	-2.1 ± 0.2	-2.4 ± 0.04	-2.7 ± 0.1

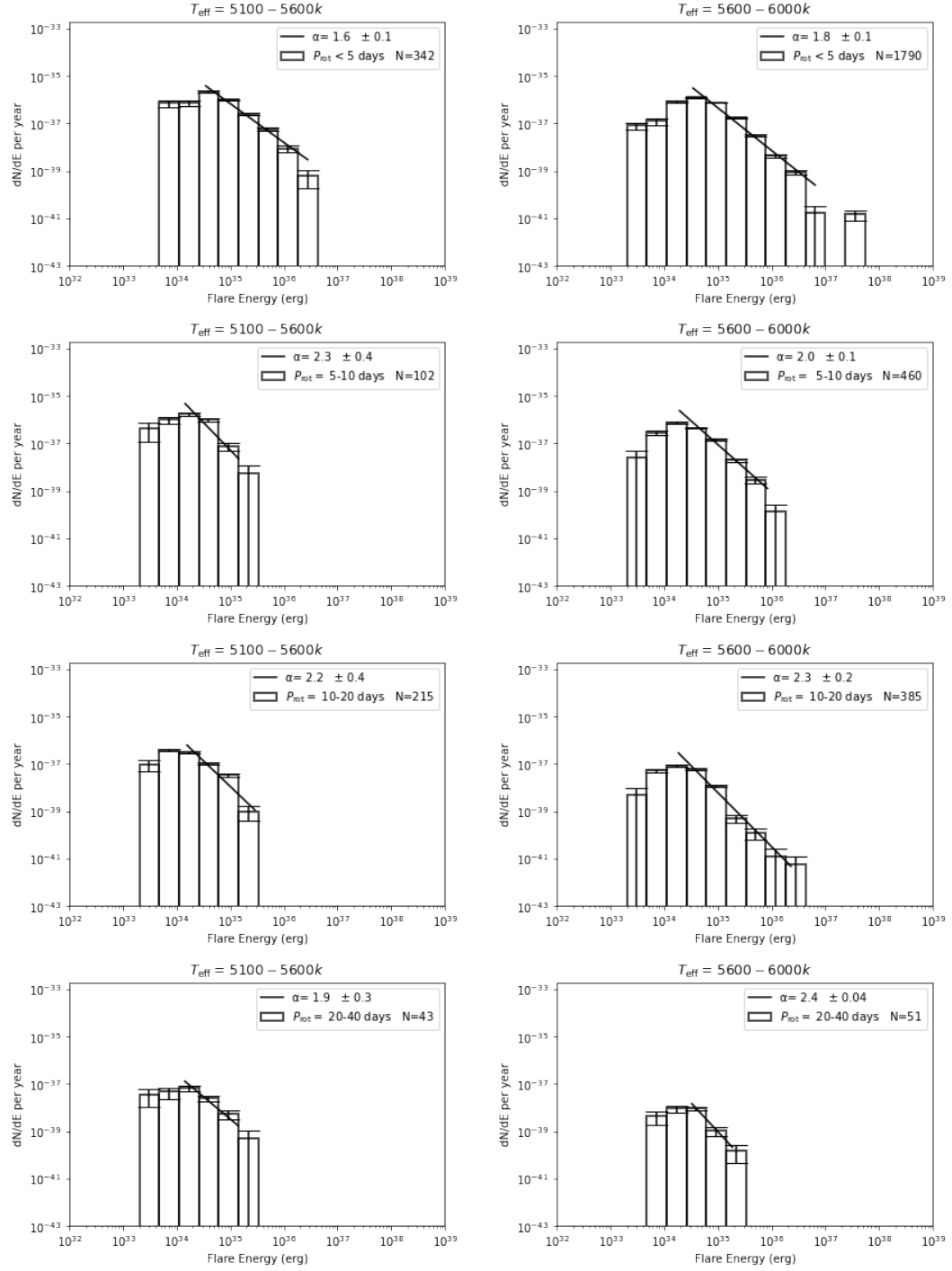Figure 2.9: The flare frequency distributions as a function of the flare energy ($dN/dE \propto E^{-\alpha}$) for different ranges of rotation periods ($P_{\rm rot}$: < 5 days, 5-10 days, 10-20 days, 20-40 days) divided by the effective temperature $T_{\rm eff}$= 5100-5600 K on the left panel and $T_{\rm eff}$= 5600-6000 K on the right panel. α is the power law index, and N is number of super-flares for each $P_{\rm rot}$.

Table 2.7: Comparison between the common flare events detected in the work of this chapter and those observed by Okamoto et al. (2021).

Kepler ID	Peak Date [a] (JD)	This work					Okamoto et al. (2021)				
		$T_{\rm eff}$ [b] (K)	Radius [b] ($R_\odot$)	$P_{\rm rot}$ (days)	Duration (day)	Energy (erg)	$T_{\rm eff}$ [c] (K)	Radius [c] ($R_\odot$)	$P_{\rm rot}$ [d] (days)	Duration (day)	Energy (erg)
3217852	55648.38	5851	0.923	16.0	0.06	9.79×10^{33}	5852	1.137	17.04	0.06	6.60×10^{33}
3217852	56021.66	5851	0.923	16.0	0.06	1.37×10^{34}	5852	1.137	17.04	0.06	7.30×10^{33}
3217852	56050.95	5851	0.923	16.0	0.08	1.76×10^{34}	5852	1.137	17.04	0.08	1.40×10^{34}
3217852	56084.25	5851	0.923	16.0	0.06	1.37×10^{34}	5852	1.137	17.04	0.08	1.70×10^{34}
3217852	56160.70	5851	0.923	16.0	0.06	1.10×10^{34}	5852	1.137	17.04	0.06	1.10×10^{34}
3853938	55197.55	5929	0.913	2.0	0.08	5.83×10^{34}	5928	1.418	2.22	0.1	9.60×10^{34}
3853938	55341.92	5929	0.913	2.0	0.06	3.58×10^{34}	5928	1.418	2.22	0.1	6.90×10^{34}
3853938	55689.27	5929	0.913	2.0	0.06	3.59×10^{34}	5928	1.418	2.22	0.06	4.80×10^{34}
3869649	55004.30	5525	0.901	1.0	0.20	2.98×10^{35}	5524	0.859	1.92	0.21	1.90×10^{35}
3869649	55061.78	5525	0.901	1.0	0.10	1.55×10^{35}	5524	0.859	1.92	0.08	5.70×10^{34}
3869649	55202.44	5525	0.901	1.0	0.08	2.21×10^{35}	5524	0.859	1.92	0.19	9.70×10^{34}
3869649	55243.90	5525	0.901	1.0	0.14	4.17×10^{35}	5524	0.859	1.92	0.21	2.70×10^{35}
3869649	55268.36	5525	0.901	1.0	0.10	2.94×10^{35}	5524	0.859	1.92	0.21	2.50×10^{35}
3869649	55348.09	5525	0.901	1.0	0.06	9.75×10^{34}	5524	0.859	1.92	0.21	7.10×10^{34}
3869649	55656.76	5525	0.901	1.0	0.14	2.53×10^{35}	5524	0.859	1.92	0.23	2.20×10^{35}
3869649	55680.83	5525	0.901	1.0	0.06	9.29×10^{34}	5524	0.859	1.92	0.1	4.00×10^{34}
3869649	55684.08	5525	0.901	1.0	0.10	1.87×10^{35}	5524	0.859	1.92	0.21	1.60×10^{35}
3869649	55732.00	5525	0.901	1.0	0.06	9.95×10^{34}	5524	0.859	1.92	0.17	6.20×10^{34}
3869649	56342.90	5525	0.901	1.0	0.06	7.01×10^{34}	5524	0.859	1.92	0.12	4.10×10^{34}
3869649	56347.33	5525	0.901	1.0	0.10	1.29×10^{35}	5524	0.859	1.92	0.21	8.40×10^{34}
4276035	55975.58	5210	0.979	23.77 [d]	0.06	2.35×10^{34}	5212	0.755	23.77	0.08	1.00×10^{34}
4276035	56260.53	5210	0.979	23.77 [d]	0.06	3.20×10^{34}	5212	0.755	23.77	0.1	1.30×10^{34}
4749912	54975.49	5734	1.127	5.0	0.08	6.57×10^{34}	5736	0.845	5.07	0.1	2.30×10^{34}
4749912	55020.65	5734	1.127	5.0	0.06	3.81×10^{34}	5736	0.845	5.07	0.06	1.00×10^{34}
4749912	55064.68	5734	1.127	5.0	0.06	3.81×10^{34}	5736	0.845	5.07	0.08	1.50×10^{34}
4749912	55100.11	5734	1.127	5.0	0.06	3.39×10^{34}	5736	0.845	5.07	0.1	1.30×10^{34}
4749912	55126.31	5734	1.127	5.0	0.06	4.94×10^{34}	5736	0.845	5.07	0.08	8.40×10^{33}
4749912	55244.51	5734	1.127	5.0	0.06	1.00×10^{35}	5736	0.845	5.07	0.15	1.80×10^{34}

Note: The full version of the table is available at https://github.com/akthukair/AFD

[a] Flare peak in Julian Date (JD).

[b] The effective temperature and stellar radius values in this chapter are derived from Data Release 25 (DR 25).

[c] The effective temperature and stellar radius values in this chapter are derived from Okamoto et al. (2021) are derived from Gaia-DR2 in Berger et al. (2018). [d] Rotation period from McQuillan et al. (2014).

2.5.2 Super Flares on Other Spectral Type Stars

We detected a total of 11438 super-flares on 1740 stars of other spectral types during 1424 days of continuous observation of dwarfs of 2653 A-type, 10898 F-type, 10307 K-type and 2222 M-type. The entire results can be found at https://github.com/akthukair/AFD.

For A-type dwarfs, we found 321 super-flares on 136 stars; 44 of these stars show more than one super-flare and 92 stars show only one super-flare. The duration of these super-flares can be up to 0.27 days, their flare maximum amplitude is 0.47. The largest flare energy we have determined is 8.91×10^{37}erg, with an amplitude of 0.28, and it lasted for 0.16 days.

As for F-type dwarfs, we discovered 1125 super-flares on 522 stars; 106 of these stars exhibit several super-flares, whereas 416 stars exhibit only one. These super-flares duration can be up to 0.57 days, and their flare amplitude can reach 0.08. Our calculations show that the highest flare energy we have found was 2.35×10^{36}erg, had an amplitude of 0.036, and lasted for 0.2 days.

Moving on to K-type dwarfs, we detected 4538 super-flares on 770 stars; 304 show several super-flares, while 466 stars show just one. The duration of these super-flares can be up to 0.3 days, and their amplitude can reach 1.04. The largest flare energy we have measured is 2.82×10^{36}erg, with an amplitude of 0.057 and a duration of 0.28 days.

For M-type dwarfs, we found 5445 super-flares on 312 stars; 256 of which have several super-flares and 56 have only one. These super-flares duration can be up to 0.82 days, and their flare amplitude varies between 0.002 to 15.1. The highest flare energy we have recorded was 1.59×10^{35}erg, has an amplitude of 15.1 and a duration of 0.18 days.

Figure 2.10 shows the flares frequency distribution on different spectral types, which follows a power-law relation ($dN/dE \propto E^{-\alpha}$). We used roughly the same energy range to obtain the best fit for α index in order to compare between the results. In order to maintain accurate statistics, we disregarded bins at the end of the histogram that contain a small number of flares (five or less).

Yang & Liu (2019a) reported a total of 162,262 flare events on 3420 flaring stars. They found that the flare frequency distribution from F-type stars to M-type stars have an index $\alpha \sim 2$, while $\alpha \sim 1$ for the flares frequency distribution of A-type stars. In our study, we found that the α index is about 2 for spectral types from F-type to M-type stars. In particular $\alpha \simeq 2.1 \pm 0.1$ for F-type stars, $\alpha \simeq 2.0 \pm 0.1$ for G-type stars, $\alpha \simeq 2.0 \pm 0.2$ for K-type stars and $\alpha \simeq 2.1 \pm 0.04$ for M-type stars. These results are consistent with the previous results of Yang & Liu (2019a). Shibata et al. (2013) found that for the Sun-like stars, the flares frequency distribution of nanoflares, microflares, solar flares
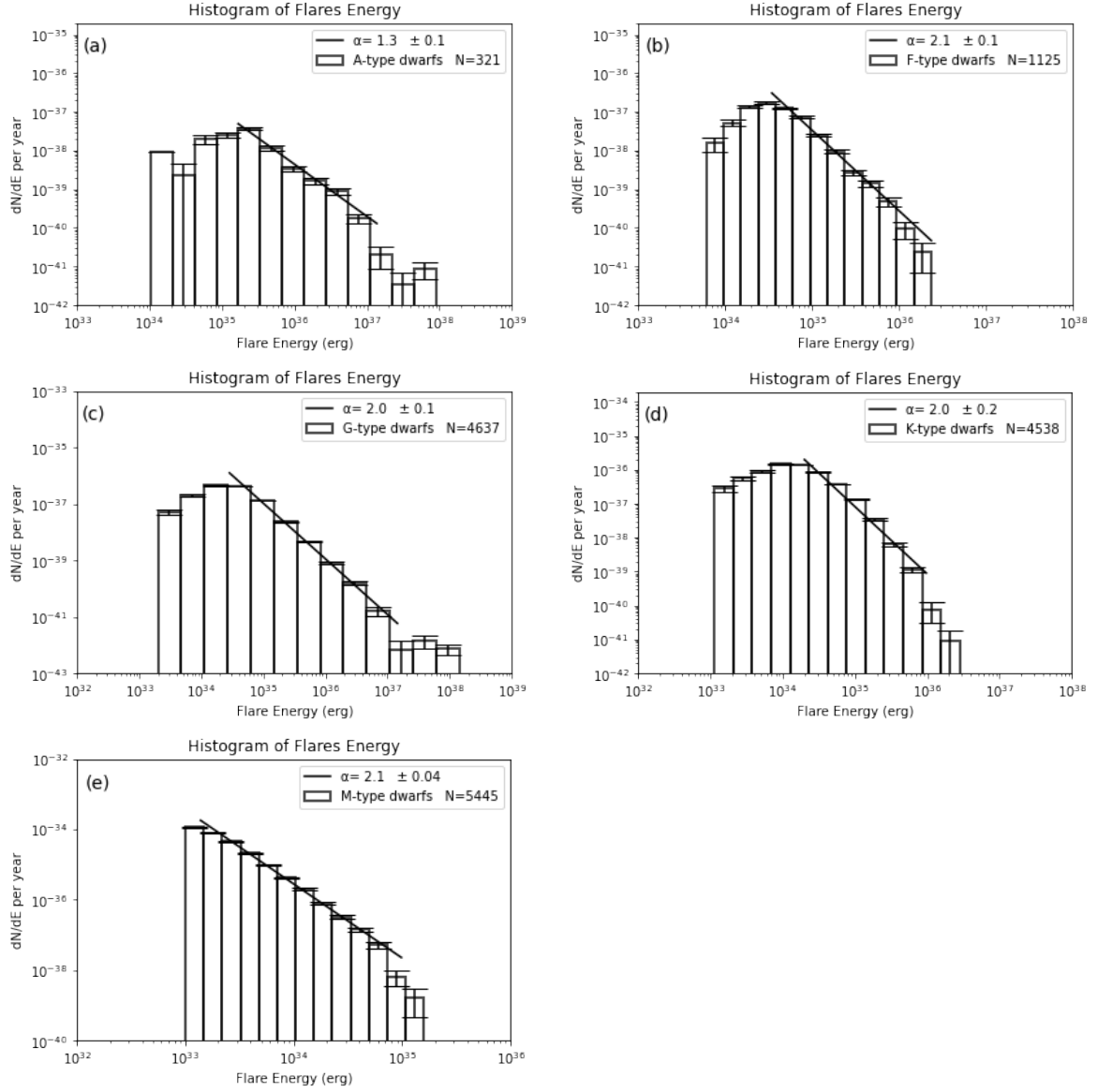
Figure 2.10: Log-log scale histograms showing the frequency distribution of super-flares organised by the stellar spectral type, with the α index of the power-law relation ($dN/dE \propto E^{-\alpha}$) and the number of super-flares for each spectral type indicated. We used approximately the same energy range for the fitting in all panels and ignored the bins towards the end of the histogram with a limited number of flares.

and superflares, follow a power-law relation with $\alpha \simeq 1.8$. It means that the underlaying mechanism which is generating these flares by magnetic reconnection occurs in similar physical conditions (Yang & Liu, 2019a; Cliver et al., 2022). It is thought that the same fundamental process that causes solar flares also causes flares in late-type stars (F-M). A convective envelope is necessary for the dynamo that generates the magnetic fields

in these stars. For magnetic fields to become strong enough to rise and emerge into the stellar atmosphere, which results in the generation of flares, this convective envelope must be sufficiently deep (Pedersen et al., 2017). The similarity of α index indicates that the process of producing flares in various spectral types from F-type to M-type stars is similar and is based on magnetic reconnection (Yang & Liu, 2019a).

However, the situation is different for A-type stars, as the α index for the flare frequency distribution differs from the rest and is $\alpha \simeq 1.3 \pm 0.1$. It is widely expected that these stars cannot have flares. For stars to produce flares, they must have a deep outer convection zone, powerful large-scale magnetic fields, or powerful winds produced by the radiation. Normal A-type stars are devoid of these characteristics. Hence they should not flare (Pedersen et al., 2017). Moreover, according to stellar evolution theories, A-type stars are unlikely to flare because of their weak magnetic fields, and their thin or nonexistent surface convection zone, preventing a magnetic dynamo from operating (Van Doorsselaere et al., 2017). However, through a visual inspection of the light curves, Balona (2012, 2013) found flare events in the light curves of 33 A-type stars. To study the origin of these flares, Pedersen et al. (2017) reported a new, detailed analysis of these 33 A-type stars and verified the existence of flares in 27 of them. Balona (2015) observed 1833 and 424 A-type stars in long cadence and short cadence modes, respectively, during Q0-Q12 using visual inspection. In the long cadence and short cadence modes, 51 and 10 A-type stars, respectively, show evidence of flare activity. Moreover, 24 new A-type stars with flaring activity have been discovered by Van Doorsselaere et al. (2017).

Table 2.8 shows the number of super-flares for each spectral type. Where $N_{\text{f (candidates)}}$ is the number of flares candidates captured by the code when the flux difference exceeded the threshold limit, $N_{\text{f (conditions)}}$ is the number of flares that met all the conditions, $N_{\text{f (check)}}$ is the number of flares we verified using visual inspection of the light curves, and $N_{\text{f (exclude)}}$ is the number of flares that we excluded due to their irregular, chaotic shape after the visual inspection of the light curves. By analyzing this table, we notice a large fraction of excluded flares are in the A-type stars compared to the M-type stars. This can be explained by the different flare conditions in the stars. One difference can be that the sizes of A-type star-spots are much larger than that of M-type, with different magnetic reconnection conditions, resulting in the flares with irregular, chaotic shapes of the light curves in A-type stars. This is possibly why A-type stars have a different α index.

Table 2.9 shows the incidence of flares for each stellar spectral type. Since our study considers main-sequence stars only, the number of stars is limited to a specific radius range for each spectral type, and therefore the number of stars in this chapter is much smaller than in other studies such as Yang & Liu (2019a). Thus the flare incidence appears in larger numbers than in those studies. The flare incidence gradually increases from F-

Table 2.8: The ratio rate of excluded flares for each spectral type.

Class	$N_{\text{f (candidates)}}$	$N_{\text{f (conditions)}}$	$N_{\text{f (check)}}$	$N_{\text{f (exclude)}}$	$N_{\text{f (exclude)}}/N_{\text{f (conditions)}}$
A	38876	953	321	632	66.32 %
F	187877	2484	1125	1359	54.71 %
G	481005	6791	4637	2154	31.72 %
K	207205	6754	4538	2216	32.81 %
M	15165	6808	5445	1363	20.02 %

Note: $N_{\text{f (candidates)}}$ represents the number of flare candidates captured by our Python code when the flux difference exceeds the threshold limit. $N_{\text{f (conditions)}}$ is the number of flares that satisfied all conditions, $N_{\text{f (check)}}$ is the number of flares that were confirmed by visual examination of the light curves. Following a visual examination of the light curves, $N_{\text{f (exclude)}}$ is the number of flares that were excluded due to their irregular, chaotic shape.

Table 2.9: The number of stars N_{star}, flare stars N_{fstar} and flare incidence for each spectral type.

Class	T_{eff} (K)	Radius ($R_\odot$)	N_{star}	N_{fstar}	incidence
A	7500 - 10000	1.4 - 1.8	2653	136	5.13 %
F	6000 - 7500	1.15 - 1.4	10898	522	4.79 %
G	5100 - 6000	0.9 - 1.15	25442	1896	7.45 %
K	3700 - 5200	0.7 - 0.96	10307	770	7.47 %
M	2400 - 3700	$\leqslant 0.7$	2222	312	14.04 %

type to M-type stars from 4.79 % to 14.04 % because of the increase of the convection zone depth (Yang & Liu, 2019a). However, the incidence of the flares in A-type stars 5.13 % is higher than in F-type stars 4.79 %, which contradicts the theoretical expectation. As from an A-type star to an F-type star, a star's outer layer changes from the radiative envelope to the convective envelope, allowing F-type stars to operate a solar-like dynamo. In contrast, A-type stars struggle to create and maintain a magnetic field (Yang & Liu, 2019a). These results are also consistent with Balona (2015); Van Doorsselaere et al. (2017); Yang & Liu (2019a), who analyzed stars of any size, not just those on the main-sequence discussed here. The deviation of the α index in A-type stars from the rest of stellar types, the rise of flare incidence rate compared to F-type stars, and the high percentage of excluded flares compared to the rest of the spectral types are all indications that A-type stars may generate flares in a different, peculiar manner.

2.6 Conclusions

Using bespoke Python script written by us, we performed an automated search for super-flares on main-sequence stars of types A, F, G, K, and M in all of Kepler's long-cadence data of DR 25 from Q0 to Q17, using Maehara et al. (2012); Shibayama et al. (2013) technique. We used the Harvard Spectral classification to determine each target's spectral type based on its effective temperature and radius. For A, F, G, K and M type stars, we studied a total of 2653, 10898, 25442, 10307, and 2222 main-sequence stars, respectively. As a result, we detected 4637 super-flares on 1896 G-type dwarfs during 1424 days of continuous observation by Kepler. Using these new data, we studied and compared the statistical properties of the occurrence frequency rate of super-flares using three distinct datasets, namely, Q0-Q6, Q6-Q17, and Q0-Q17. According to our estimates for the Q0-Q17 dataset, a super-flare on G-type dwarfs with an energy of 10^{35} erg occurs on a star once every 4360 years. By comparing three data sets (0-6, 7-17 and 0-17), the statistics of flare look very similar, which is indicative of the fact that flare occurring statistic does not change on the time scale of 17 quarters. In addition, we compared our results with those of Okamoto et al. (2021) regarding the flare frequency distribution FFD and the α index for the power-law relation. The similarity of the results supports the consistency with Okamoto et al. (2021) prior research. This suggests that the high-pass filter and analysis of sample biases on super-flare occurrence rates that Okamoto et al. (2021) performed while considering gyrochronology and the completeness of the flare detection had no appreciable impact on our final results, which is one of the motivations for our study. Also, we compared 183 similar flare events to Okamoto et al. (2021) on a case-by-case basis, as in Table 7. We noted an overestimation of the flare energy for our study compared to Okamoto et al. (2021). Despite using a different catalog of stellar parameters, available to us, we found that the results are consistent with Okamoto et al. (2021). The different stellar parameters in the Gaia catalog had no significant effect on our findings as illustrated in Table 2.7. Moreover, we detected a total of 321, 1125, 4538 and 5445 super-flares on dwarfs of 136, 522, 770 and 312 A, F, K and M type stars respectively, during 1424 days of continuous observation. We determined the distributions of super-flare occurrence rates as a function of super-flare energy. We found that for all spectral types of stars, from F-type to M-type, the flare frequency distribution as a function of flare energy follows a power-law relation with $dN/dE \propto E^{-\alpha}$ where $\alpha \simeq 2.0$ to 2.1. This demonstrates that the power-law index α is similar to those of solar flares (~ 2) (Shibayama et al., 2013). The power-law index values' similarity suggests that similar physical conditions produce the flares, by the mechanism which is thought to be magnetic reconnection. In contrast, the obtained value of α index 1.3 of the flare frequency distribution for A-type stars indicates

that their flare conditions are distinct from those of the other stellar types. We observed a general rise in the flare incidence rate from 4.79 % and 14.04 % for F-type to M-type stars. However, the flare incidence rate is higher in A-type stars 5.13 % than in F-type stars 4.79 %, contrary to the theoretical expectation (Yang & Liu, 2019a). These results are similar to those found by Balona (2015); Van Doorsselaere et al. (2017); Yang & Liu (2019a).

In general, flares with smaller amplitude tend to be more challenging to detect. Therefore, the detection completeness of flares with smaller amplitude is lower than that of larger ones, and the actual frequency of flares with smaller amplitude would be higher than the observed one. In addition, as discussed in Okamoto et al. (2021), the flare-detection threshold proposed by Maehara et al. (2012); Shibayama et al. (2013) depends on the rotation period and the amplitude of rotational modulations. In relation to the evaluation and discussion on the flare-detection completeness, which has a significant impact on the power-law slope of the flare-frequency distribution (FFD), we would like to remark that since the power law slope for G type-stars is similar to that of Shibayama et al. (2013) and for A-type stars that of Yang & Liu (2019a), we believe that a lack of dedicated analysis of flare-detection completeness has no significant impact on our results.

In relation to the contamination of flares on close neighboring stars we would like to remark that since the spatial resolution of the Kepler space telescope is not high (~ 4 arcsec/pixel), some stars have close neighbors within the photometric aperture. As pointed out by Maehara et al. (2012); Pedersen et al. (2017), flares on close neighboring stars can produce false flare signals in the target light curve. These false flares may potentially have an impact on the flare frequency. Although we excluded the stars having neighboring stars within 12-arcsec, we believe that this is sufficient despite the fact that not all faint stars are cataloged. Again our belief is backed up by the fact that the power law slope for G type-stars is similar to that of Shibayama et al. (2013) and for A-type stars that of Yang & Liu (2019a).

In relation to how we determine the flare energy range used for fitting the observed FFD to the power-law function, we would like to acknowledge the fact that the number of flares in the lower energy bins would be much smaller than the actual flare frequency. Therefore, one should choose the energy range in which the detection completeness issue can be negligible. In our case, the choice which leftmost energy range bins to ignore was done intuitively by eye, similar to Yang & Liu (2019a).

3 New Cases of Super-flares on Slowly Rotating Solar-type Stars and Large Amplitude Super-flares in G- and M-type Main-sequence Stars

3.1 Summary of the Chapter

This chapter is based on the publication of Althukair & Tsiklauri (2023c). In chapter 2, we searched for super-flares on different types of stars while focusing on G-type dwarfs using entire Kepler data to study statistical properties of the occurrence rate of super-flares. Using these new data, as a by-product, we found fourteen cases of super-flare detection on thirteen slowly rotating Sun-like stars with rotation periods of 24.5 to 44 days. This result supports the earlier conclusion by others that the Sun may possibly have a surprise super-flare. Moreover, we found twelve and seven new cases of detection of exceptionally large amplitude super-flares on six and four main-sequence stars of G- and M-type, respectively. No large-amplitude flares were detected in A, F, or K main-sequence stars. Here we present preliminary analysis of these cases. The super-flare detection, i.e. an estimation of flare energy, is based on a more accurate method compared to previous studies. We fit an exponential decay function to flare light curves and study the relation between e-folding decay time, τ, vs. flare amplitude and flare energy. We find that for slowly rotating Sun-like stars, large values of τ correspond to small flare energies and small values of τ correspond to high flare energies considered. Similarly, τ is large for small flare amplitudes and τ is small for large amplitudes considered. However, there is no clear relation between these parameters for large amplitude super-flares in the main sequence G- and M-type stars, as we could not establish clear functional dependence between the parameters via standard fitting algorithms.

3.2 Introduction

It is believed the Solar and stellar flares are powered by a physical process called magnetic reconnection, in which connectivity of magnetic field lines in the atmospheres of stars changes rapidly (Masuda et al., 1994; Shibata et al., 1995). This is accompanied by acceleration of plasma particles and release of heat. The source of this kinetic and thermal energy is the energy stored in the magnetic field. Thus, the magnetic dynamo process which is one of possible means to generate magnetic field via bulk plasma flows is of great importance for understanding of what can power and therefore be source for a flare or a super-flare. The energies of observed stellar flares lie in the wide range from 10^{28} to 10^{37} erg, while the highest energy of any observed solar flare is approximately few times 10^{32} erg. Thus, generally agreed terminology is that a super-flare should have an energy in excess of 10^{34} erg. A plausible dynamo model capable to explain the generation of magnetic energy sufficient to support super-flares has been recently suggested in Kitchatinov & Olemskoy (2016) and then further investigated in Katsova et al. (2018). In this scenario, rather than producing stellar cycles similar to the solar 11 year cycle, the dynamos in superflaring stars excite some quasi-stationary magnetic configuration with a much higher magnetic energy. Further, Kitchatinov et al. (2018) used a flux-transport model for the solar dynamo with fluctuations of the Babcock-Leighton type α-effect to generate statistics of magnetic cycles. As a result, they concluded that the statistics of the computed energies of the cycles suggest that super-flares with energies in excess of 10^{34} erg are not possible on the Sun.

Historical records suggest that no super-flares have occurred on the Sun in the last two millennia. In the past there were notable examples detection of super-flares on Sun-like stars. There are two references which support such a claim Schaefer et al. (2000) and Nogami et al. (2014).

As claimed by Schaefer et al. (2000) they identified nine cases of super-flares involving 10^{33} to 10^{38} ergs on main sequence Sun-like stars. Sun-like means that stars are on or near the main-sequence, have spectral class from F8 to G8, are single (or have a very distant binary companion). The super-flare energy estimation by Schaefer et al. (2000) was based on photometric methods.

Nogami et al. (2014) reported the results of high dispersion spectroscopy of two 'super-flare stars', KIC 9766237, and KIC 9944137 using Subaru/HDS telescope. These two stars are G-type main sequence stars, and have rotation periods of 21.8 days, and 25.3 days, respectively. Their spectroscopic results confirmed that these stars have stellar parameters similar to those of the Sun in terms of the effective temperature, surface gravity, and metallicity. By using the absorption line of Ca II 8542, the average strength of the

magnetic field on the surface of these stars was estimated to be 1-20 G. The super-flare energy estimation by Nogami et al. (2014) used a semi-empirical method based on magnetic energy density times volume of flare. These results claim that the spectroscopic properties of these super-flare stars are very close to those of the Sun, and support the hypothesis that the Sun may have a super-flare. What causes super-flares is an open issue and many theories exist to explain their origin. Karak et al. (2020) have shown that sun-like slowly rotating stars, having anti-solar differential rotation, i.e. when equatorial regions of the star rotate slower than the polar regions, can produce a very strong magnetic field and that could be a possible explanation for the superflare. It is the anti-solar differential rotation that can produce strong fields in slowly rotating stars. A study conducted by Karak et al. (2020) focuses on mean-field kinematic dynamo modeling to investigate the behaviour of large-scale magnetic fields in different stars with varying rotation periods. They specifically consider two cases: stars with rotation periods larger than 30 days, which exhibit antisolar differential rotation (DR), and stars with rotation periods shorter than 30 days, which exhibit solar-like DR. The study supports the possible existence of antisolar differential rotation in slowly rotating stars and suggests that these stars may exhibit unusually enhanced magnetic fields and potentially produce cycles that are prone to the occurrence of super-flares. In general the transition from solar to anti-solar differential rotation happens somewhere around the Rossby number of unity. For the Sun, it is obviously solar-like, but when the rotation rate decreases, one expects to have an anti-solar differential rotation. This robust transition has been seen in many numerical simulations. Karak et al. (2015), for example, using global MHD convection simulations, consistently find anti-solar differential rotation when the star rotates slowly.

Statistical study of super-flares on different stellar types has been an active area of research (Maehara et al., 2012; Shibayama et al., 2013; Wu et al., 2015; He et al., 2015, 2018; Yang et al., 2017; Van Doorsselaere et al., 2017; Lu et al., 2019; Yang & Liu, 2019a; Günther et al., 2020; Tu et al., 2020; Gao et al., 2022). Shibayama et al. (2013) studied statistics of stellar super-flares. These authors discovered that for Sun-like stars (with surface temperature 5600-6000 K and slowly rotating with periods longer than 10 days), the occurrence rate of super-flares with an energy of $10^{34} - 10^{35}$ erg is once in 800-5000 yr. Shibayama et al. (2013) confirmed the previous results of Maehara et al. (2012) in that the occurrence rate (dN/dE) of super-flares versus flare energy E shows a power-law distribution with $dN/dE \propto E^{-\alpha}$, where $\alpha \sim 2$. Such occurrence rate distribution versus flare energy is roughly similar to that for solar flares. Tu et al. (2020) identified and verified 1216 super-flares on 400 solar-type stars by analyzing 2-minute cadence data from 25,734 stars observed during the first year of the TESS mission. The results indicate a higher frequency distribution of super-flares compared to the findings from the

Kepler mission. This difference may be due to a significant portion of the TESS solar-type stars in the dataset are rapidly rotating stars. The power-law index γ of the super-flare frequency distribution was determined to be $\gamma = 2.16 \pm 0.10$, which is consistent with the results obtained from the Kepler mission. The study highlights an extraordinary star, TIC43472154, which exhibits approximately 200 super-flares per year. Tu et al. (2020) analyzed the correlation between the energy and duration of super-flares, represented as $T_{duration} \propto E^\beta$. They derived a power-law index $\beta = 0.42 \pm 0.01$ for this correlation, which is slightly larger than the value of $\beta = 1/3$ predicted by magnetic reconnection theory. Similar conclusion has been reached earlier by Maehara et al. (2015), who found that the duration of superflares, τ, scales as the flare energy, E, according to $\tau \propto E^{0.39 \pm 0.03}$. Yang et al. (2023) analyzed TESS light curves from the first 30 sectors of TESS data with a two-minute exposure time. They identified a total of 60810 flare events occurring on 13478 stars and performed a comprehensive statistical analysis focusing on the characteristics of flare events, including their amplitude, duration, and energy. We believe that the method for flare energy estimation used in Shibayama et al. (2013); Yang et al. (2017) is more accurate than one used by Schaefer et al. (2000) and Nogami et al. (2014). Therefore, we rely on the methodology proposed by Shibayama et al. (2013) and Althukair & Tsiklauri (2023b) to estimate the flare's energy.

In chapter 2, we searched for super-flares on different spectral class stars, while focusing on G-type dwarfs (solar-type stars) using Kepler data using quarters $0 - 17$ with the purpose of study the statistical properties of the occurrence rate of super-flares. Shibayama et al. (2013) studied statistics of stellar super-flares based on Kepler data in quarters $0 - 6$ ($Q0 - Q6$). In chapter 2, we investigated how the results are modified by adding more quarters, i.e. what is α power-law for data quarters $0 - 17$ and $7 - 17$. Here using the more extended Kepler data, we also found 14 cases of detection of Super-flares on 13 Slowly Rotating Sun-like starts in each of KIC 3124010, KIC 3968932, KIC 7459381, KIC 7459381, KIC 7821531, KIC 9142489, KIC 9528212, KIC 9963105, KIC 10275962, KIC 11086906, KIC 11199277, KIC 11350663 and KIC 11971032. Thus the main purpose of the present study is to present analysis of these new 14 cases. The main novelty here is that the detection is based on the Shibayama et al. (2013) method, which is more accurate, as compared to Schaefer et al. (2000) and Nogami et al. (2014) for the flare energy estimation. Our results support earlier conclusion by others (Schaefer et al. (2000) and Nogami et al. (2014)) that the Sun may have a surprise super-flare. We stress that chapter 2 has conducted a more comprehensive study of determination of stellar rotation periods based on a robust method such as used by McQuillan et al. (2014) in comparison to Shibayama et al. (2013). We believe that more accurate period determination used in chapter 2 has led to the current new results, presented in this chapter 3. In addition to

the 14 cases of of Super-flares on Slowly Rotating Sun-like starts, we detected 12 and 7 super-flares with a large amplitude on five G-type and four M-type main sequence stars, respectively.

Solar flares emit energy at all wavelengths, but their spectral distribution is still unknown. When white-light continuum emission is observed, the flares are referred to as "white-light flares" (WLFs). Kretzschmar (2011) identified and examined visible light emitted by solar flares and found that the white light is present on average during all flares and must be regarded as a continuum emission. Kretzschmar (2011) also demonstrated that this emission is consistent with a black body spectrum with temperature of 9000 K and that the energy of the continuum contains roughly 70% of the total energy emitted by the flares. WLFs are among the most intense solar flares, and it has been demonstrated that an optical continuum appears anytime the flare's EUV or soft X-ray luminosity reaches a reasonably large threshold (McIntosh & Donnelly, 1972; Neidig & Cliver, 1983). Thus, optical continuum is presumably present in all flares but only in a few cases it reaches a measurable degree of brightness. This conclusion implies that WLFs are not fundamentally different from conventional flares (Neidig, 1989). Nonetheless, WLFs are important in flare studies because they are similar to stellar flares ways (Worden, 1983) and because they represent the most extreme conditions encountered in solar optical flares (Neidig, 1989). Using observations from the Transiting Exoplanet Survey Satellite (TESS), Ilin et al. (2021) present four fully convective stars that exhibited white light flares of large size and long duration. The underlying flare amplitude as a fraction of the quiescent flux of two flares is greater than two. After the discovery of the largest amplitude flares ever recorded on the L0 dwarf, which reached $\Delta V \approx -11$ magnitude Schmidt et al. (2016), Jackman et al. (2019) detected a large amplitude white-light super-flare on the L2.5 dwarf ULAS J224940.13011236.9 with the flux $\Delta V \approx -10$ magnitude which corresponds to a relative brightness ratio of 10000. This can be demonstrated as follows:

$$\Delta V = V_{\max} - V_{\min} \approx -10, \tag{3.1}$$

where $V_{\max}$ is the apparent magnitude in the visible band corresponding to the flux at the maximum amplitude ($F_{\max}$), and $V_{\min}$ is the apparent magnitude in the visible band corresponding to the flux at the minimum state ($F_{\min}$). Using the magnitude difference calculation :

$$V_{\max} - V_{\min} = -10 = 2.5 \log_{10}(F_{\min}/F_{\max}), \tag{3.2}$$

it is clear that $F_{\max}/F_{\min} = \Delta F/F = 10000$.

Stellar superflares have been studied in multiple wavelength bands, such as X-rays and

the Hα band. It is important to mention relevant studies here: Wu et al. (2022) analyzed spectroscopic data from LAMOST DR7 and identified a stellar flare on an M4-type star that is characterized by an impulsive increase followed by a gradual decrease in the Hα line intensity. The Hα line, which corresponds to a specific transition in hydrogen, exhibits a Voigt profile during the flare. After the impulsive increase in the Hα line intensity, a clear enhancement was observed in the red wing of the Hα line profile. Additionally, the estimated total energy radiated through the Hα line during the flare is on the order of 10^{33} erg, providing an indication of the overall energy release associated with the event. Chandra/HETGS time-resolved X-ray spectroscopic observations were used by Chen et al. (2022) to study the behaviour of stellar flares on EV Lac. They discovered distinct plasma flows caused by flares in the corona of EV Lac, but none of them provided evidence for the actual occurrence of stellar CMEs. In most flares, the flow of plasma is accompanied by a rise in the density and temperature of the coronal plasma.

In this chapter, we present the detection of 14 super-flares on 13 slowly-rotating Sun-like stars, 12 and 7 cases of large amplitude super-flares on five G-type dwarfs and four M-type dwarfs respectively. Section 3.3 presents the method used including the flare detection, the flare energy estimation, and rotation period determination. Section 3.4 provides the main results of this chapter. Section 3.5 closes this chapter by providing the main conclusions.

3.3 Methods

3.3.1 Flare Detection

As done in Chapter 2, we conducted an automated search for super-flares on main-sequence stars type (A, F, G, K, M) based on entire Kepler data, using our Python script on long cadence data from Data Release 25 (DR 25) following Maehara et al. (2012); Shibayama et al. (2013) method. The target selection and method description can be found in Subsections 2.4.1 and 2.4.2, respectively.

Figure 3.1 displays typical results for the used method for KIC 9963105. The light curve of KIC 9963105 is shown in Figure 3.1(a). Figure 3.1(b) shows the distribution of the brightness difference between every two adjacent data points of the KIC 9963105 light curve. 1% of the total area under the distribution curve is represented by the green vertical line. The red vertical line represents the flare detection threshold value, equal to three times the 1% value of the area under the distribution curve. The blue vertical line is 3σ of the distribution of the brightness variation.
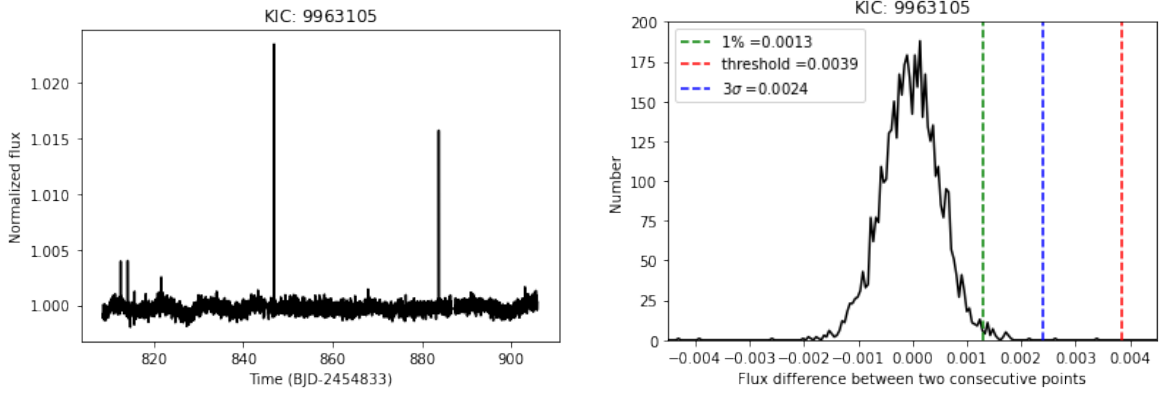
Figure 3.1: Illustrations of flares detection method used by Shibayama et al. (2013). (a) The light curve of KIC 9963105. (b) The distribution of brightness variation between each pair of adjacent data points in the light curves of KIC 9963105. The green vertical line represents the value of 1% of the total area under the curve, the red vertical lines represents the flare detection threshold and the blue vertical represents 3σ of the brightness variation distribution.

3.3.2 Energy Calculation

Schaefer et al. (2000) identified nine cases of super-fares involving $10^{33} - 10^{38}$ ergs on normal solar-type stars. Their super-flare energy estimate has a large uncertainty, e.g. Groombridge 1830 (HR 4550) total flare energy (in the blue band alone) is 10^{35} ergs with an uncertainty of a factor of a few due to having only four points on the light curve.

The possibility that super-flares can be explained by magnetic energy stored on the star's surface was considered by Nogami et al. (2014) Using the Ca ii 8542 absorption line, they estimate that the average magnetic field strength (B) of KIC 9766237 and KIC 9944137 is 1-20 Gauss, and the super-flare of these targets has a total energy of 10^{34} erg. Under the assumption that the energy released during the flare represents a fraction (f) of the magnetic energy stored around the spot area. Their flare energy (E_{flare}) was calculated as follows:

$$E_{\text{flare}} \sim f\frac{B^2}{8\pi}L^3. \tag{3.3}$$

The length of the magnetic structure causing the flare (L), has been considered to be the same size as the spotted region, i.e. $L = \sqrt{a\pi R_*^2}$ where a is the spot's area, which giving that

$$E_{\text{flare}} \sim f\frac{B^2}{8\pi}(a\pi R_*^2)^{3/2}. \tag{3.4}$$

Our energy estimation for each flare depends on the star's luminosity (L_{star}), flare amplitude (f_{amp}), and flare duration (Shibayama et al., 2013; Yang et al., 2017). L_{star}, the amount of energy that the star emits in one second, is proportional to the star's radius

R squared and its surface temperature T_{eff} to the fourth power, and is obtained from the following equation:

$$L_{\mathrm{star}} = \sigma_{\mathrm{SB}} T_{\mathrm{eff}}^4 4\pi R^2, \tag{3.5}$$

where σ_{SB} is the Stefan-Boltzmann constant, $4\pi R^2$ is the entire surface area of the star. The continuum emission from a white-light flare is consistent with blackbody radiation at around 9000 K, as suggested by Hawley & Fisher (1992); Kretzschmar (2011). Based on Shibayama et al. (2013); Yang et al. (2017); Günther et al. (2020), we set T_{flare} = 9000 K and derive the luminosity of a blackbody-emitting star as follows:

$$L_{\mathrm{flare}}(t) = \sigma_{\mathrm{SB}} T_{\mathrm{flare}}^4 A_{\mathrm{flare}}, \tag{3.6}$$

where A_{flare} is the flare's area, as determined by the formula:

$$A_{\mathrm{flare}}(t) = f_{\mathrm{amp}}(t)\pi R^2 \frac{\int R_\lambda B_\lambda(T_{\mathrm{eff}})d\lambda}{\int R_\lambda B_\lambda(T_{\mathrm{flare}})d\lambda}, \tag{3.7}$$

where f_{amp} represents the flare amplitude for the relative flux and R_λ represents the Kepler instrument's response function (Caldwell et al., 2010). The Kepler photometer covers various wavelengths, from 420 to 900 nm. The Plank function at a specific wavelength, denoted by $B_\lambda(T)$, is given by:

$$B_\lambda(T) = \frac{2hc^2/\lambda^5}{e^{hc/\lambda kT} - 1}, \tag{3.8}$$

where h represents Planck's constant, c the speed of light, T the black body temperature, and k Boltzmann's constant. By substituting Eq.(3.7) into (3.6), we calculate the total flare energy by the integral of L_{flare} over the flare duration :

$$E_{\mathrm{flare}} = \int_{t_{\mathrm{start}}}^{t_{\mathrm{end}}} L_{\mathrm{flare}}(t)dt. \tag{3.9}$$

We determine energy of the flares using Shibayama et al. (2013) energy estimation method, which assumes blackbody radiation from both the star and flare, with a fixed flare temperature of 10,000 K, to estimate the quiescent luminosity. We note that Shibayama et al. (2013) energy estimation can have an error of up to 60% and yet this is more accurate than the one used by Schaefer et al. (2000) and Nogami et al. (2014). To improve the accuracy, Davenport (2016) proposed an alternative method for estimating the quiescent luminosity of each star to determine the actual energy of the flares. They used the Equivalent Duration (ED) parameter, which represents the integral under the flare in fractional

flux units, as a relative energy measurement for each flare event without requiring flux calibration of the Kepler light curves. To calculate the actual energy of the flares emitted in the Kepler band pass (erg), the ED values (sec) are multiplied by the quiescent luminosity (erg/sec) of the respective star. This approach establishes an absolute scale for the relative flare energies, as the quiescent luminosity is individually estimated for each star.

3.3.3 Rotational Period Determination

Light curve periods were calculated using the Lomb-Scargle periodogram, a common statistical approach for detecting and characterising periodic signals in sparsely sampled data. We used an oversampling factor of five (VanderPlas, 2018), and use PDCSAP flux to generate a Lomb-Scargle periodogram for each light curve from Q2 to Q16. Furthermore, the period corresponding to the maximum power of the periodogram was allocated as the rotation period for the Kepler ID in a specific quarter. This value was estimated with an accuracy of a day without the decimal component because fractions of a day would not significantly alter the results, allowing us to automate the selection of the star's rotation period rather than manually. We set 0.5 days for periods shorter than a day and eliminated periods less than 0.1 days. Finally, for each Kepler ID, we choose the most frequent period across all quarters from Q2 to Q16. Following the McQuillan et al. (2014) technique, we required that the period chosen for all quarters be identified in at least two unique segments, with the segment defined as three consecutive Kepler quarters. (Q2,Q3,Q4), (Q5, Q6, Q7), (Q8, Q9, Q10), (Q11, Q12, Q13) and (Q14,Q15,Q16).

3.4 Results

By performing an automated search for super-flares on G-type main-sequence stars during 1442 days of Kepler observation in all of (DR 25) long-cadence data from Q0 to Q17, we found 14 super-flares on 13 slowly rotating Sun-like stars in each of (KIC 3124010, KIC 3968932, KIC 7459381, KIC 7459381, KIC 7821531, KIC 9142489, KIC 9528212, KIC 9963105, KIC 10275962, KIC 11086906, KIC 11199277, KIC 11350663 and KIC 11971032), with a surface temperature of $5600K \leqslant T_{\text{eff}} < 6000K$, a surface gravity of $\log g > 4.0$, and a rotational period P_{rot} range between 24.5 and 44 days. Figure 3.2 shows seven light curves of these events. The left panels display light curves over a 90-day of observation. The blue arrow on the left panel indicates the observed super-flare, which met all conditions. The right panels show zoomed in time light curves of super-flares. The blue squares represent the data points for a super-flare. We fitted an exponential decay function to the flare light curve to characterise the flares, shown by a

red dashed curve. This exponential decay function is given by:

$$f(t) = a \, e^{-t/\tau} + b \tag{3.10}$$

where $f(t)$ is the relative flux as a function of time, a is the flare peak height, which is approximately equal to the relative flux at the flare peak, b is the relative flux in the quiescent state and τ is the decay time of the flare, which is the time at which the relative flux is decreased to $1/e \simeq 0.3679$ of its initial value. The value of τ, a and b of the exponential decay function for each flare are shown in the right panel.

Flare parameters and their duration, amplitudes, energies and τ values are listed in Table 3.1. The rotation periods for these slowly rotating Sun-like stars were taken from McQuillan et al. (2014). Their flare energies range from $(1.9 - 9.0) \times 10^{34}$ erg. The flare amplitude of the slowly rotating Sun-like stars is relatively small, ranging between 0.002 and 0.018. We also find that the duration of flares in all of these cases is the same 0.061 days. This is probably due to the fact that flare duration of all small amplitude super-flares is two data points in time or *less*. Therefore, because one of the flare detection conditions in our code is that there must be at least two data points between the flare's peak and the end, cases with flare duration less than two points were not detected, and we end up with the same duration super-flares with the two data points. Because it appears that there are no small amplitude super-flares with duration *greater* than two data points, all flare duration end up the same. This selection effect is because we use long cadence light curve data, which has a 29.4-minute interval between each data point in time. The value of τ varies from 0.012 to 0.036 days.
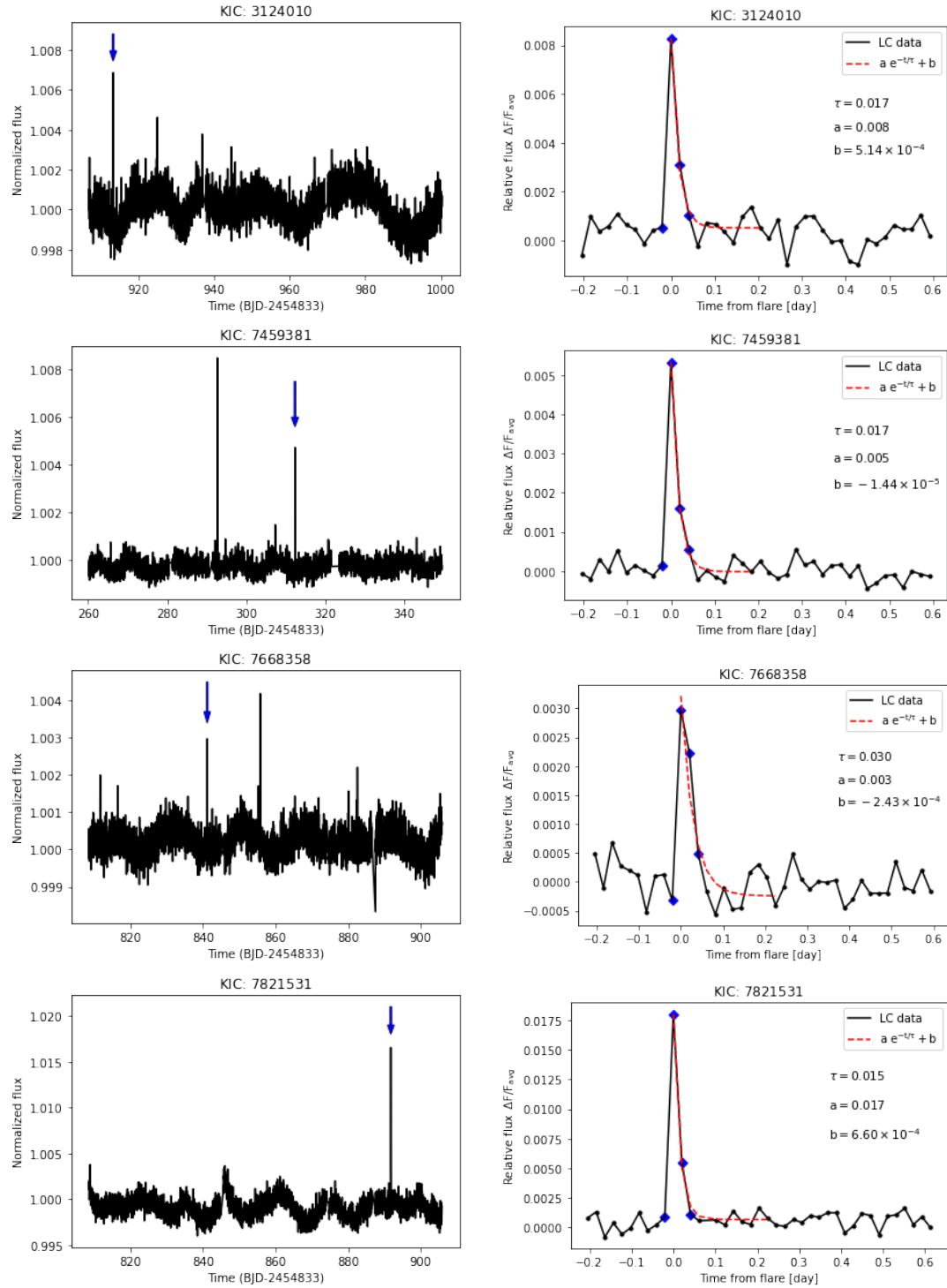
Figure 3.2: The left panel displays the light curves of super-flares. The x-axis in the left panel is the time in (BJD) and the y-axis is the normalized flux. The blue arrows indicates the occurrence of super-flares. The right panels show zoom in time of these super-flares. The x-axis in the right panel is the time from the flare peak in (day) and the y-axis is the relative flux ($\Delta F/F_{avg}$). Each data points for a super-flare is represented by blue squares in the right panel. The dashed red curve indicates an exponential fit of the decay phase. τ in the equation refers to the best fit of exponential decay time, a refers to the final value of the amplitude fit and b refers to the fitted relative flux in the quiescent state.
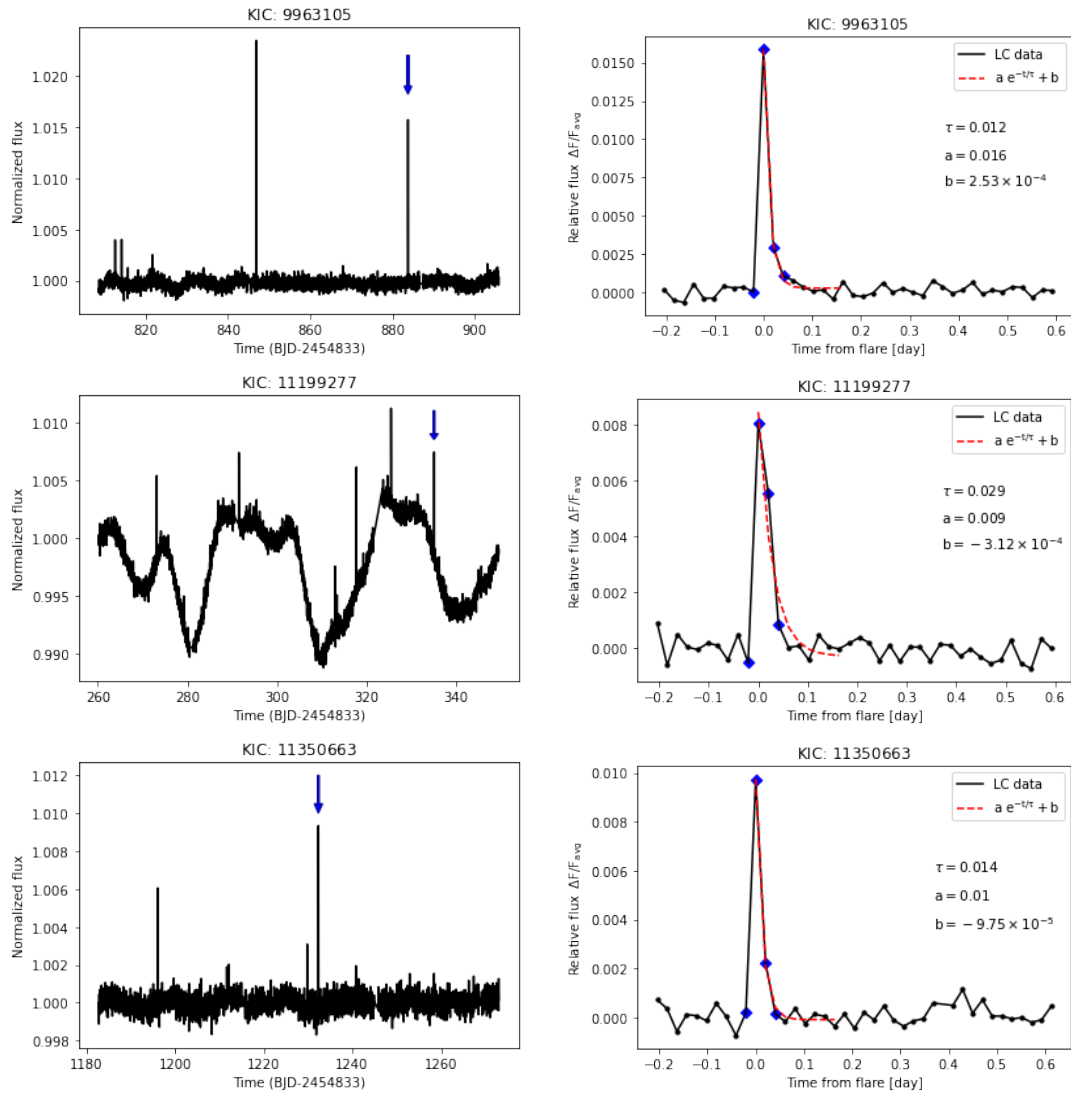
Figure 3.2: Figure 3.2 continued

Table 3.1: super-flares on slowly rotating Sun-like stars.

Kepler ID	T_{eff} (K)	log g	Radius ($R_\odot$)	P_{rot}[a] (day)	t_{start} (BJD)	t_{end} (BJD)	t_{peak} (BJD)	amp	Flare Duration (day)	τ (day)	Flare Energy (erg)
3124010	5688	4.46	1.01	25.90	913.24	913.30	913.26	0.008	0.061	0.017	4.57×10^{34}
3968932	5716	4.39	0.96	24.56	868.88	868.94	868.90	0.004	0.061	0.026	3.89×10^{34}
7459381	5635	4.27	1.11	26.19	312.31	312.37	312.33	0.005	0.061	0.017	4.89×10^{34}
7668358	5668	4.36	0.98	41.83	841.13	841.19	841.15	0.003	0.061	0.030	1.94×10^{34}
7821531	5681	4.52	0.92	32.66	891.81	891.87	891.83	0.018	0.061	0.015	8.63×10^{34}
9142489	5878	4.51	0.95	25.20	1561.13	1561.19	1561.15	0.004	0.061	0.028	2.61×10^{34}
9528212	5872	4.42	0.97	61.43	1332.34	1332.40	1332.36	0.003	0.061	0.036	2.31×10^{34}
9963105	5751	4.39	1.01	28.09	883.80	883.86	883.82	0.016	0.061	0.012	9.00×10^{34}
10275962	5782	4.51	0.91	26.12	213.21	213.27	213.23	0.007	0.061	0.035	3.71×10^{34}
10275962	5782	4.51	0.91	26.12	599.85	599.91	599.87	0.004	0.061	0.029	2.04×10^{34}
11086906	5758	4.38	1.11	29.18	1206.01	1206.07	1206.03	0.002	0.061	0.018	1.90×10^{34}
11199277	5638	4.49	0.92	29.00	325.43	325.49	325.45	0.008	0.061	0.029	3.72×10^{34}
11350663	5966	4.49	0.96	36.92	1232.31	1232.37	1232.33	0.010	0.061	0.014	5.21×10^{34}
11971032	5942	4.51	0.94	44.00	1231.92	1231.98	1231.94	0.006	0.061	0.030	3.80×10^{34}

[a] Rotation period from McQuillan et al. (2014).

We calculated the frequency distribution of the 14 super-flares on the 13 slowly rotating Sun-like stars and plotted a log scale histogram presenting this distribution as shown in Figure 3.3. The x-axis represents the flare's energy, and the y-axis represents the number of super-flares per star per year per unit of energy. Therefore, we calculated the weight for each bin using

$$w = \frac{3.16 \times 10^7}{N_{\text{os}} \times D \times E},$$ (3.11)

where N_{os} is the number of observed stars, D is the duration of the observation period in seconds, and E is the super-flare energy that belongs to that bin. From the number of stars in Table 2.3 in chapter 2, we estimated that the number of observed G-type dwarfs with $5600K \leqslant T_{\text{eff}} < 6000K$ and $P_{\text{rot}} > 10$ days is equal to 19160 stars. Since this distribution is related to slowly rotating Sun-like stars with P_{rot} between 24.5 and 44 days, we estimated the number of the observed stars to be one-third of the original sample, i.e. 5635 stars, given that the average rotation period is 34 days which is almost three times the period of 10 days. We estimated the probability of the occurrence of super-flares in slowly rotating Sun-like stars with P_{rot} of 24.5 to 44 days. We found that the rate of super-flares incidence with the energy of 4.54×10^{34} erg is 1.94×10^{-4} flares per year per star, corresponding to a super-flare occurring on a star once every 5160 years. We calculated this value by multiplying the average energy from the x-axis by the average dN/dE from the y-axis, $4.54 \times 10^{34} \times 4.27 \times 10^{-39} = 1.94 \times 10^{-4}$ flares per year per star, and by taking the reciprocal of 1.94×10^{-4}, we get 5160 which gives the number of years in which a flare occurs on a star. The frequency distribution of these 14 super-flares follows a power law relation $dN/dE \propto E^{-\alpha}$ where $\alpha = 1.9 \pm 0.2$. This is consistent with our previous result in chapter 2 for the frequency distribution of slowly rotating G-type dwarfs where $\alpha = 2.0 \pm 0.1$.

In addition to the 14 cases of of super-flares on slowly rotating Sun-like starts, we detected 12 super-flares with a large amplitude on 6 G-type dwarfs in each of KIC 5865248, KIC 6783223, KIC 7505473, KIC 10053146, KIC 10057002 and KIC 11709752. Figure 3.4 shows eight light curves of these events same as Figure 3.2. Table 3.2 shows the duration, amplitude, energy, and τ values for these super-flares with their parameters. The energy of their flares range from 1.67×10^{36} to 1.42×10^{38} erg. The rotation period of KIC 1170952 was obtained in this chapter. As for the rotation period for the other five stars, no such data is available. Even applying the method described in chapter 2 does not allow period determination in these five cases. According to Yang et al. (2017), there are three possible reasons: (i) due to the inclination angle and low activity level, the light curve has a small amplitude at the accuracy level of Kepler; (ii) fast-rotating stars have spots in the poles (Schüssler & Solanki, 1992), making it hard to detect light variation
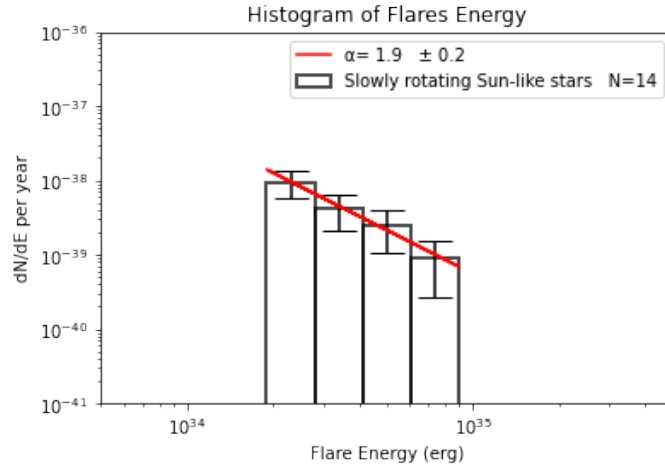
Figure 3.3: log-log scale histograms showing the distribution of flare frequency as a function of flare energy of 14 super-flares on slowly rotating Sun-like stars. The distribution follows a power-law relation $dN/dE \propto E^{-\alpha}$ where $\alpha = 1.9 \pm 0.2$

through rotation; and (iii) the rotation period is longer than 90 days (a quarter), making it difficult (or impossible) to detect them in the frequency spectrum of the star. The flare amplitude for these cases range between 4.05 and 35.60. These flares tend to last longer than flares with smaller amplitude of slowly rotating Sun-like stars as their duration varies between 0.061 and 0.143 day. The τ values of flares exhibiting large amplitude on G-type main-sequence stars are observed to be higher than those of flares occurring on slowly rotating Sun-like stars, as their values range between 0.014 and 0.058 days.
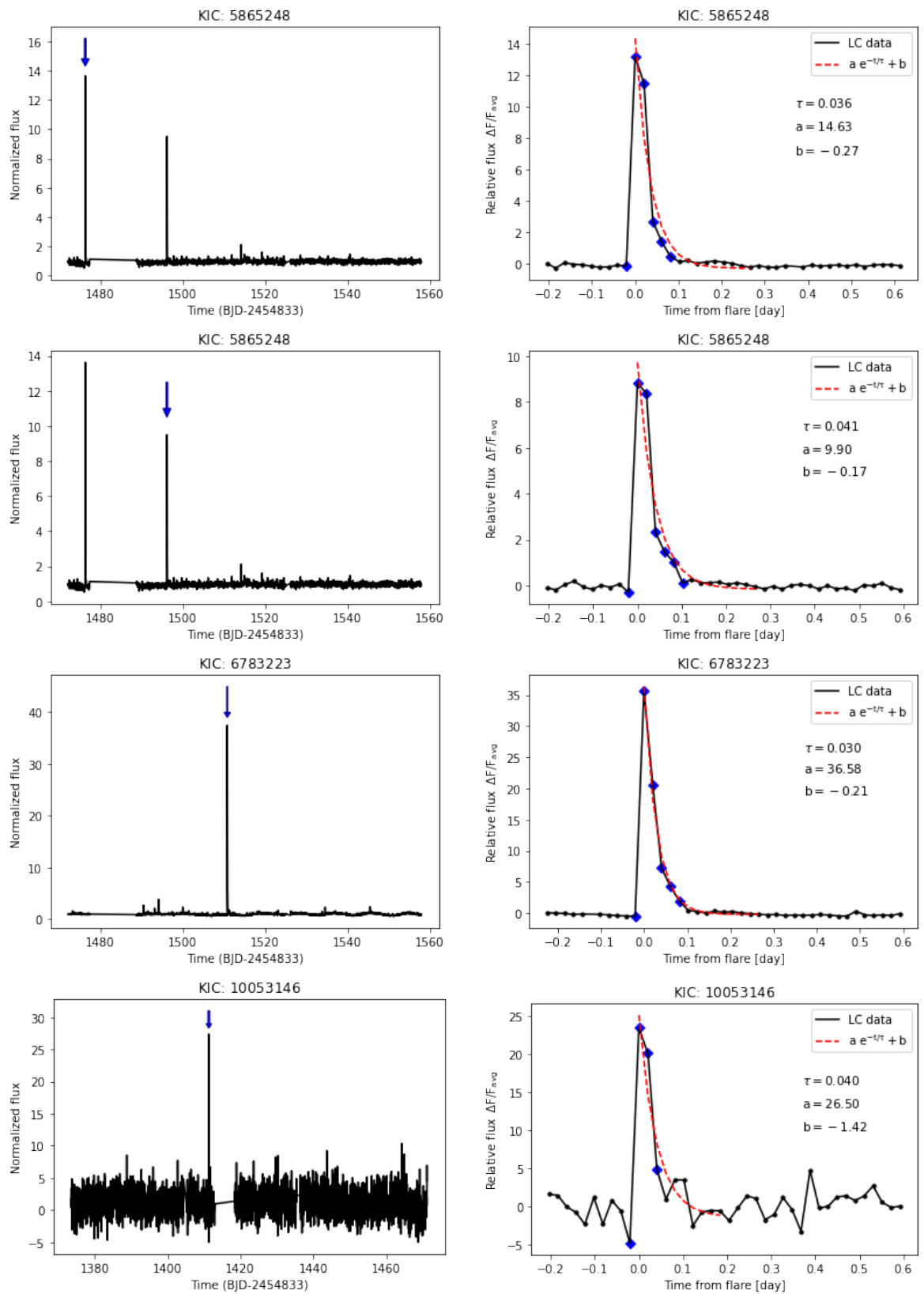
Figure 3.4: Same as Figure 3.2 but for large amplitude super-flares on G-type main-sequence stars.

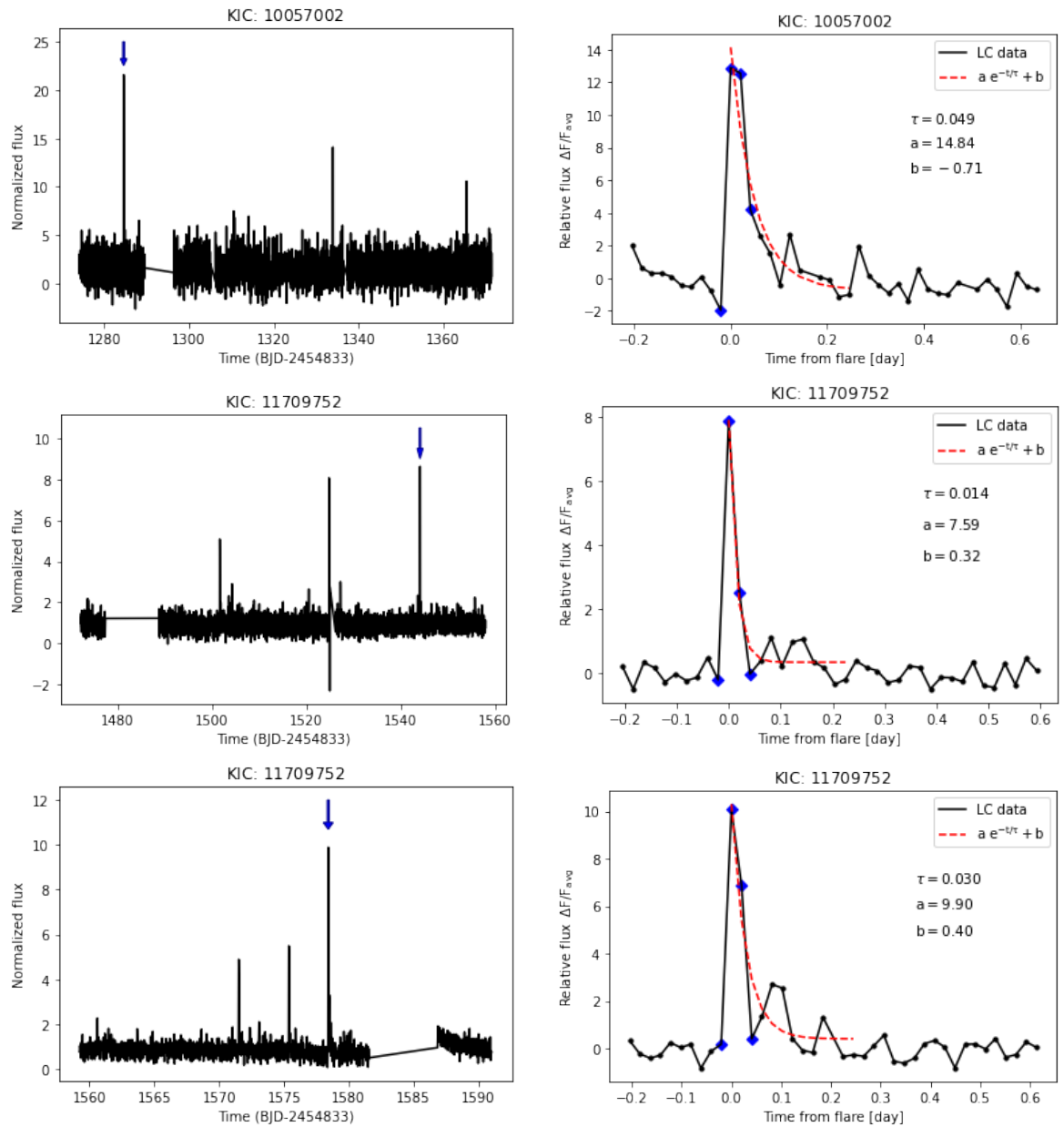Figure 3.4: Same as Figure 3.2 but for large amplitude super-flares on G-type main-sequence stars

Table 3.2: Large amplitude super-flares on G-type main-sequence stars.

Kepler ID	T_{eff} (K)	log g	Radius ($R_\odot$)	P_{rot}[a] (day)	t_{start} (BJD)	t_{end} (BJD)	t_{peak} (BJD)	amp	Flare Duration (day)	τ (day)	Flare Energy (erg)
5865248	5780	4.44	1	NA	1476.22	1476.33	1476.24	13.16	0.102	0.036	7.29×10^{37}
5865248	5780	4.44	1	NA	1496.09	1496.21	1496.11	8.78	0.123	0.041	9.56×10^{37}
5865248	5780	4.44	1	NA	1561.78	1561.86	1561.80	8.14	0.082	0.034	6.75×10^{37}
6783223	5780	4.44	1	NA	1510.76	1510.86	1510.78	35.60	0.102	0.030	8.6×10^{37}
7505473	5780	4.44	1	NA	1385.81	1385.95	1385.85	4.05	0.143	0.058	1.67×10^{36}
10053146	5780	4.44	1	NA	1411.27	1411.33	1411.29	22.75	0.061	0.040	1.42×10^{38}
10057002	5780	4.44	1	NA	1284.52	1284.58	1284.54	12.03	0.061	0.049	6.24×10^{37}
11709752	5780	4.44	1	0.5	1501.56	1501.62	1501.58	4.21	0.061	0.031	2.85×10^{37}
11709752	5780	4.44	1	0.5	1544.06	1544.13	1544.08	7.65	0.061	0.014	2.85×10^{37}
11709752	5780	4.44	1	0.5	1571.49	1571.55	1571.51	4.48	0.061	0.033	3.94×10^{37}
11709752	5780	4.44	1	0.5	1575.35	1575.43	1575.37	5.11	0.082	0.046	5.44×10^{37}
11709752	5780	4.44	1	0.5	1578.39	1578.45	1578.41	9.40	0.061	0.030	3.94×10^{37}

[a] Rotation period by Althukair & Tsiklauri (2023b).

For stars of other spectral classes, no significant flares with large amplitudes were detected on main-sequence stars of type A, F, and K. Only M-type main-sequence stars manifested seven super-flares with large amplitude on each of KIC 6580019, KIC 7123391, KIC 7341517 and KIC 9201463. Similar to Figures 3.2 and 3.4, Figure 3.5 displays the seven light curves for these events. The parameters of these super-flares, including their duration, amplitude, energy, and τ values, are displayed in Table 3.3. These flares have an energy between 3.16×10^{33} and 1.59×10^{35} erg, amplitude ranges between 3.91 and 15.14 and their duration lasts between 0.018 and 0.044 day. τ values for super-flares with large amplitude on M-type main sequence stars vary from 0.030 to 0.049 days.

Table 3.3: Large amplitude super-flares on M-type main-sequence stars.

Kepler ID	T_{eff} (K)	log g	Radius ($R_\odot$)	P_{rot}[a] (day)	t_{start} (BJD)	t_{end} (BJD)	t_{peak} (BJD)	amp	Flare Duration (day)	τ (day)	Flare Energy (erg)
6580019	2661	5.28	0.12	NA	609.97	610.09	609.99	3.91	0.123	0.044	7.04×10^{33}
6580019	2661	5.28	0.12	NA	674.45	674.60	674.47	10.30	0.143	0.041	1.25×10^{34}
7123391	3326	5.12	0.19	NA	638.53	638.59	638.55	8.07	0.061	0.038	4.76×10^{34}
7123391	3326	5.12	0.19	NA	692.09	692.19	692.13	12.38	0.102	0.018	1.23×10^{35}
7123391	3326	5.12	0.19	NA	794.54	794.72	794.56	15.14	0.184	0.049	1.59×10^{35}
7341517	2661	5.28	0.12	NA	877.95	878.12	877.99	5.27	0.163	0.041	4.82×10^{33}
9201463	3319	5.14	0.18	NA	215.11	215.27	215.15	5.51	0.163	0.030	3.16×10^{33}

We examined whether there is a dependence between τ vs. flare amplitude (f_{amp}) and τ vs. flare energy (E_{flare}). Therefore, we graphically display six panels in Figure 3.6 showing the relationship between τ and the amplitude of flares and τ and the energy of flares in slow-rotating Sun-like stars 3.6(a, b), G-type stars 3.6(c, d) and M-type stars 3.6(e, f) respectively. In 3.6(a) for slowly-rotating Sun-like stars, we find that for small amplitude, τ is large, and when the amplitude is large, τ is consistently small in the range considered. The same applies to the relation between τ and energy in Figure 3.6(b), we see that large τ values correspond to small energies and small values of τ correspond to large energies considered. On the contrary, there is no clear relation between τ vs. f_{amp} and τ vs. E_{flare} in G-type and M-type main sequence stars in Figure 3.6(c-f). However, as mentioned in the Introduction, according to Maehara et al. (2015), the duration of superflares, τ, scales as the flare energy, E, according to $\tau \propto E^{0.39\pm0.03}$. Similarly, Tu et al. (2020) found that $T_{duration} \propto E^{0.42\pm0.01}$. It broadly follows from the simple reconnection scaling arguments, that $\tau \propto E^{1/3}$. We believe that we could not deduce such scaling because of small number of data points in Figure 3.6. We tried various functions of fit using Python's *curve_fit* and Excel's *trendline*, referred to as a (line of best fit), to visualize the general trend for the data. We could not find any reliable, functional fit dependence between those parameters because *the coefficient of determination*, R^2, which shows how well the data fit the regression model, is less than 0.5 for all those cases in Figure 3.6(a to f). Hence any attemted fit has been unreliable, as only fit with $R^2 > 0.5$ can be deemed acceptable. To determine the extent to which the two variables, τ and flare amplitude, as well as τ and flare energy, are correlated, we calculated the *Pearson Correlation Coefficient* (r), which measures the strength and direction of the relationship between two variables, using IDL's built-in function $\mathrm{CORRELATE(X, Y)}$ and Python's function *scipy.stats.pearsonr*. Both IDL and Python gave the same values. The values for the Pearson correlation coefficient (r) between two datasets are listed in Table 3.4. We note that for the slowly rotating sun-like stars datasets, $r = -0.592$ and $r = -0.691$ for τ vs. f_{amp} and τ vs. E_{flare} respectively, which suggests a noticable negative correlation between the variables. For the remaining 4 cases these r values are close to zero, which indicates a weak or nonexistent correlation between the two variables. In general, r varies from -1 to 1. The extreme cases of $r = \pm 1$ mean that there is clear linear correlation/anti-correlation. $r = 0$ means that there is no linear relation between the variables.

In the context of explaining the absence of large-amplitude flares detected in A-, F-, and K-type main-sequence stars, while they are only detected in G-type and M-type stars we would like to remark the following. Using Kepler space telescope, Chang et al. (2018) studied of the light curves of the M dwarfs. They found a number of flare events with the peak flux increases $\Delta F/F \geq 1$. Magnetic fields of the M dwarfs are generated by

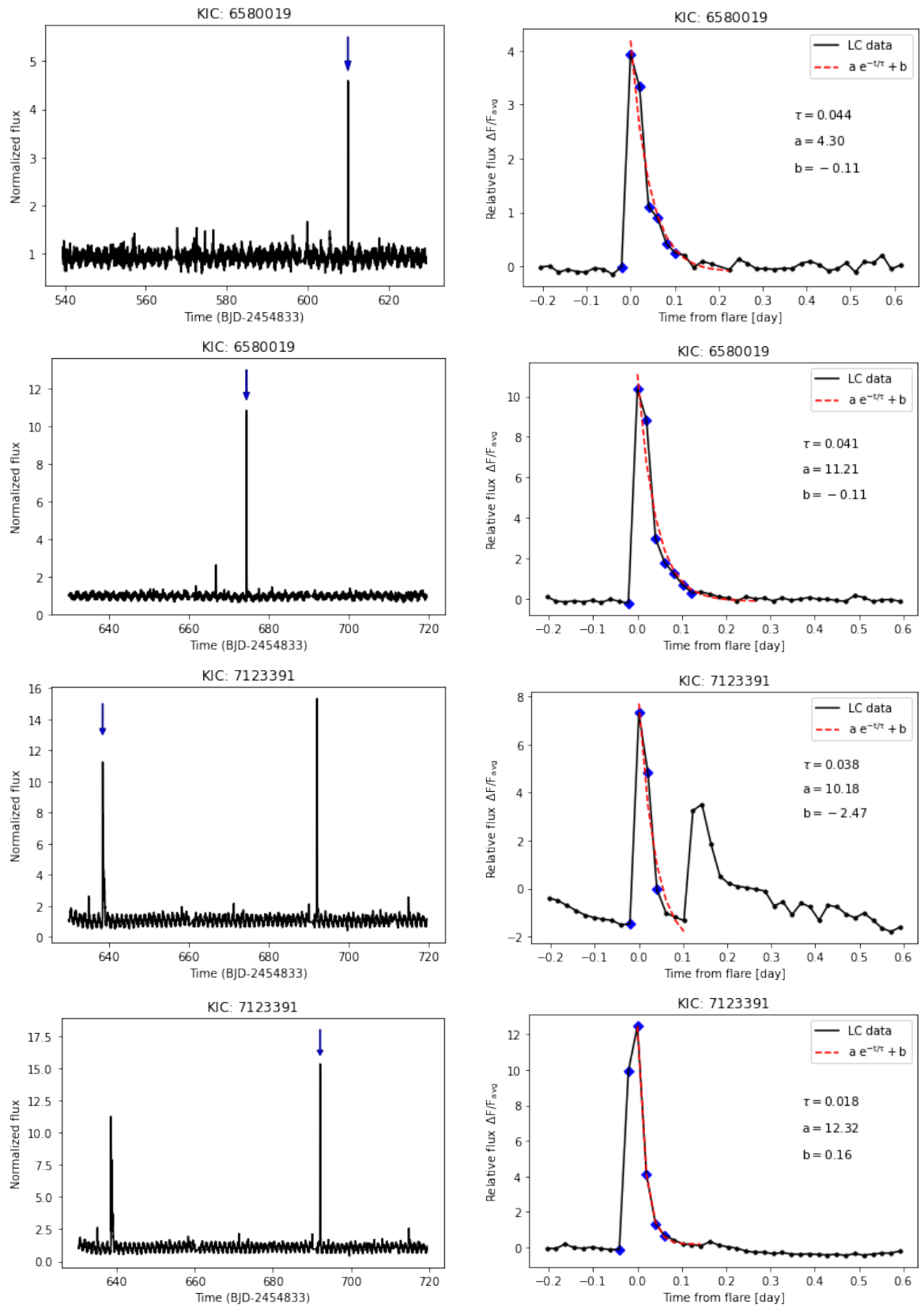Figure 3.5: Same as Figures 3.2 and 3.4 but for large amplitude super-flares on M-type main-sequence stars.
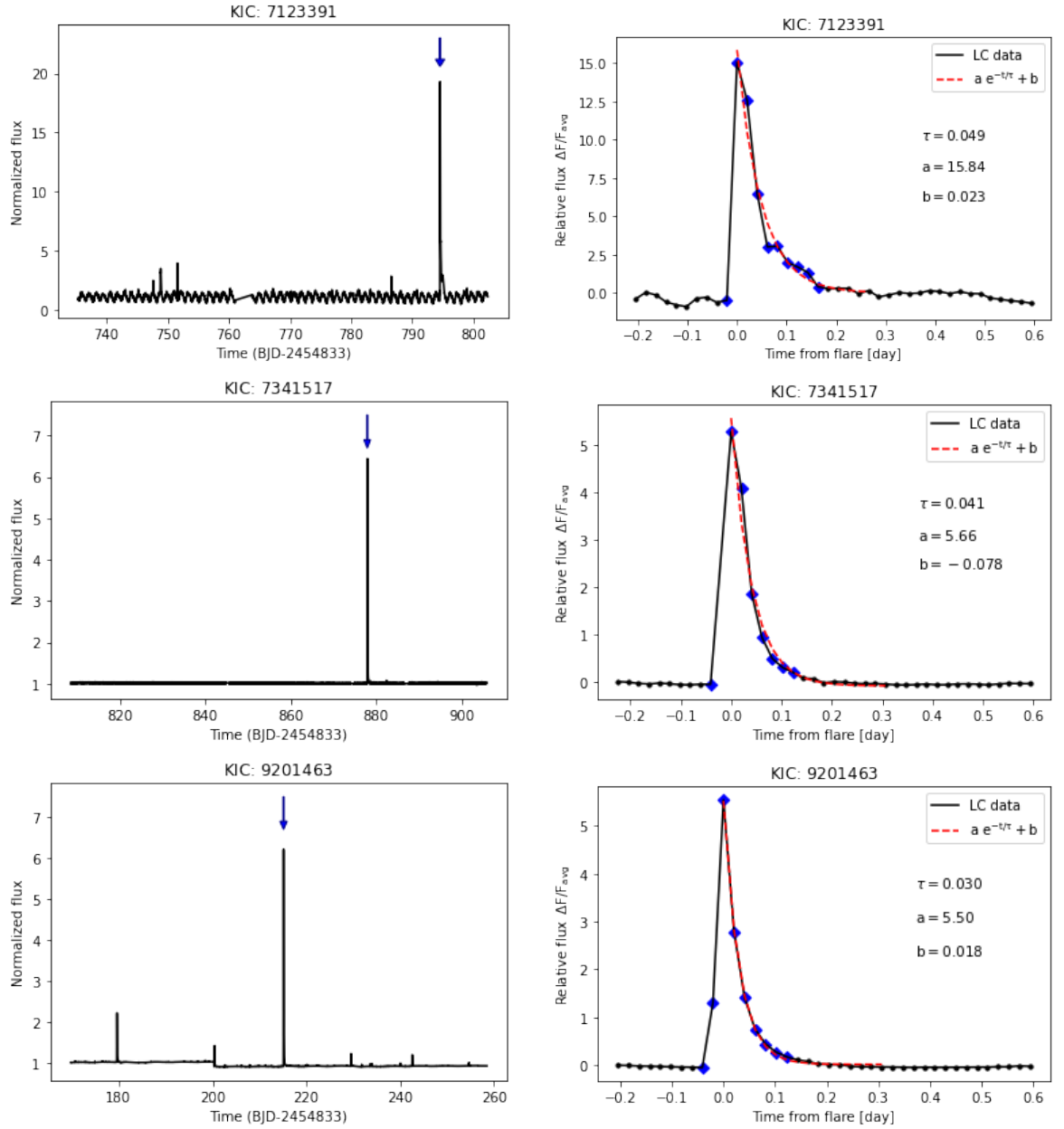
Figure 3.5: Same as Figures 3.2 and 3.4 but for large amplitude super-flares on M-type main-sequence stars.

Table 3.4: The Pearson correlation coefficient between τ vs. f_{amp} and τ vs. E_{flare}.

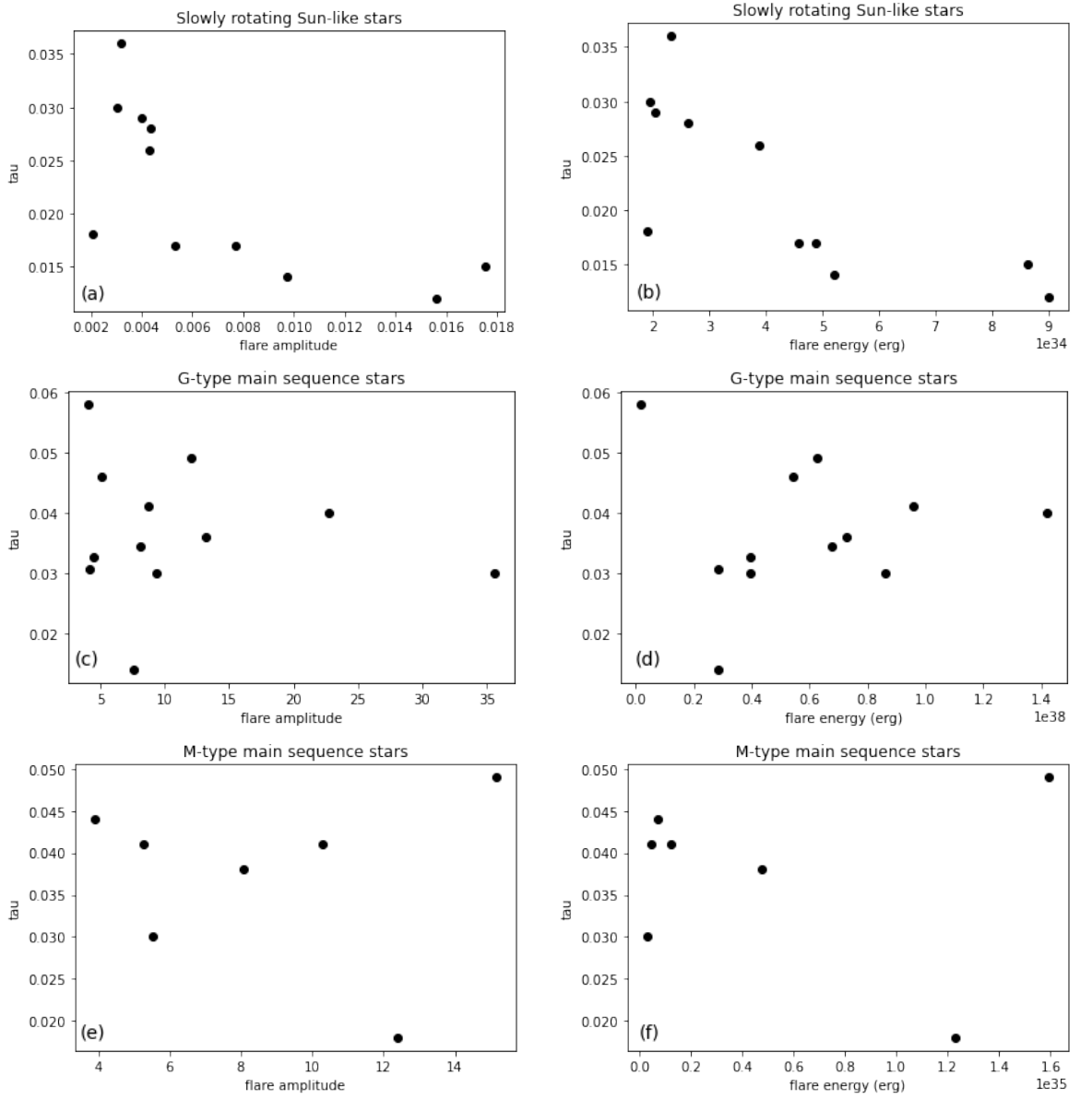| Sample	τ vs. f_{amp}	τ vs. E_{flare}
Slowly rotating sun like stars	-0.592	-0.691
G-type large amplitude flares	-0.149	0.141
M-type large amplitude flares	-0.046	-0.098

Figure 3.6: The left panels display a scatter plot showing the relation between τ values on the y-axis with the flare amplitude f_{amp} on the x-axis. While the right panels display a scatter plot showing the relation between τ values on the y-axis with the flare energy E_{flare} on the x-axis. For flares on slowly rotating Sun-like stars,(a) demonstrates that τ values are large for low flare amplitudes but consistently small for high flare amplitudes. Likewise,(b) demonstrates that high τ values correspond to low flare energies, whereas low τ values correspond to high flare energies. For large amplitude super-flares on G-type dwarfs (c,d) and M-type dwarfs (e,f), τ has no clear connection to the f_{amp} or E_{flare}.

turbulent magnetic dynamo mechanism. This is due to their deep convective zones, and this leads to very powerful flares, compared the G-type stars (Davenport et al., 2014). As for G-type stars, detection of strength of flares in such stars have been know for some time starting from Maehara et al. (2012). Therefore is not entirely surprising that that we detected large-amplitude flares in G- and M-type stars. As for A-, F-, K-type stars we remark that according to Pedersen et al. (2017) for the flare generation, stars must have: eaither a deep outer convection zone for F5-type and perhaps later-types; or strong, radiatively driven winds for B5-type and earlier types; or strong large-scale magnetic fields for A and B-type stars. Pedersen et al. (2017) and earlier works suggest that normal A-type stars have non such features and thus should not flare. However, flares and super-flares have previously been detected on such stars according to Bai & Esamdin (2020) and references therein. The situation with K-type stars is somewhat a 'gray area'. Stars less massive and cooler than our Sun are K dwarfs; and even fainter and cooler stars are the red-coloured M dwarfs. Thus K dwarfs are probably borderline case where large-amplitude flares can occur.

3.5 Conclusions

Using our Python script on long cadence data from Data Release 25 (DR 25), we searched for super-flares on main-sequence stars of types (A, F, G, K, and M) based on the entire Kepler data following the method of Maehara et al. (2012); Shibayama et al. (2013). The Kepler targets' parameters were retrieved from the Kepler Stellar interactive table in the NASA Exoplanet Archive. Using these data, we detected 14 super-flare on 13 Sun-like stars with a surface temperature of $5600K \leqslant T_{\mathrm{eff}} < 6000K$, and P_{rot} range from 24.5 to 44 days. In addition, we found 12 and 7 cases of large amplitude super-flares on six and four main-sequence G and M type stars, respectively. Main-sequence stars of other spectral types A, F, and K showed no signs of large-amplitude super-flares. To characterise the flares, we fit an exponential decay function to the flare light curve given by $f(t) = a\,e^{-t/\tau} + b$. We study the relation between the decay time of the flare after its peak τ vs. f_{amp} and τ vs. E_{flare}. For slowly rotating Sun-like stars, we find that τ is large for small flare amplitudes and τ is small for large flare amplitudes considered. Similarly, we find that large τ values correspond to small flare energies and small τ values correspond to high flare energies considered. However, for the main sequence stars of the G and M types, τ has no apparent relation to the f_{amp} or E_{flare}. We experimented with several different fit functions between τ vs. f_{amp} and τ vs. E_{flare} to better see the underlying pattern in the data. Since the R^2 is less than 0.5 in these cases, we could not identify a reliable fit

functional dependence between these parameters.

In conclusion, we believe that:

(i) the thirteen peculiar Kepler IDs that are Sun-like, slowly rotating with rotation periods of 24.5 to 44 days, and yet can produce a super-flare with energies in the range of $(2 - 9) \times 10^{34}$ erg; and

(ii) six G-type and four M-type Kepler IDs with exceptionally large amplitude super-flares, with the relative flux in the range $\Delta F/F_{\mathrm{avg}} = 4 - 35$;

defy our current understanding of stars and hence are worthy of further investigation.

4 Prediction of Short Stellar Activity Cycles using Derived and Established Empirical Relations between Activity and Rotation Periods

4.1 Summary of the Chapter

This chapter is based on the publication of Althukair & Tsiklauri (2023d). In chapter 2, we investigated the occurrence rate of super-flares on various types of stars and their statistical properties, with a particular focus on G-type dwarfs, using entire Kepler data. The said study also considered how the statistics change with stellar rotation period, which in turn, had to be determined. Using such new data, as a by-product, we found 138 Kepler IDs of F and G types main sequence stars with rotation periods less than a day ($P_{\rm rot} < 1$ d). On one hand, previous studies have revealed short activity cycles in F-type and G-type stars and the question investigated was whether or not short-term activity cycles are a common phenomenon in these stars. On the other hand, extensive studies exist which establish empirical connection between a star's activity cycle and rotation periods. In this chapter, we compile all available Kepler data with $P_{\rm rot} < 1$ d, derive and use, established empirical relation between $P_{\rm cyc}$ and $P_{\rm rot}$ with the aim to provide predictions for very short $5.09 \leq P_{\rm cyc} \leq 38.46$ d cases in a tabular form. We propose an observation to measure $P_{\rm cyc}$ using monitoring program of stellar activity (e.g. activity-related chromospheric emission S-index) or similar means for the Kepler IDs found in this study in order put to test the derived here empirical relations between $P_{\rm cyc}$ and $P_{\rm rot}$. We also propose an alternative method for measuring very short $P_{\rm cyc}$, using flare-detection algorithms applied to future space mission data.

4.2 Introduction

The 11-year cycle of solar activity discovered by Schwabe in 1844 (Schwabe, 1844), is a significant phenomenon in solar and stellar physics. The cycle is manifested by a periodic change in solar activity, including the appearance of sunspots and changes in the Sun's magnetic field on this time-scale. Smoothed sunspot numbers have been widely used as a proxy for solar activity over the past four centuries (Shepherd et al., 2014). The idea of the sunspot number was first introduced by Waldmeier (1961) in the mid-19th century, and it has since become a standard measure for quantifying solar activity. These numbers reveal that there are almost regular cycles of about 11 years, reflecting the Sun's magnetic activity.

During the course of a solar cycle, the Sun experiences alternating periods of strong and weak activity known as solar maximum and minimum (Hathaway et al., 2002; Shepherd et al., 2014; Reinhold et al., 2017). As the solar cycle progresses, the magnetic field becomes more complex and twisted. This results in the emergence of sunspots, which are dark areas on the surface of the Sun with intense magnetic fields, vary in size and can last from days to several months (Petrovay & van Driel-Gesztelyi, 1997), decaying into bright areas called faculae formed by smaller magnetic concentrations (Reinhold et al., 2017). During the active phase of the solar cycle (solar maximum), the sunspots number increases, and their size becomes larger on the surface of the Sun. At the same time, bright faculae also become more prominent. As the cycle progresses, the number of sunspots decreases, the overall brightness of the Sun reduces, and the Sun enters its least active phase of the solar cycle (solar minimum). These dark and bright features on the Sun's surface contribute to the variability in the total solar irradiance (TSI) (Marchenko et al., 2022). Therefore, the TSI data can capture the combined effects of the evolving dark and bright features during the solar cycle (Domingo et al., 2009; Reinhold et al., 2017).

Cyclic activity has been observed in stars other than the Sun through long-term brightness changes associated with increased occurrence of active regions on their surfaces or in their lower stellar atmospheres (Reinhold et al., 2017). The Mount Wilson HK program, which started in 1966 and lasted until the end of the 20th century, was the first to conduct a systematic search for activity cycles in main sequence stars (Wilson, 1978; Baliunas et al., 1995; Mittag et al., 2019a). By examining chromospheric emission within the Ca II H&K spectral lines, the magnetic field associated with active regions on stellar surfaces is vital in conveying energy to the chromosphere. This heightened influx of energy into the chromosphere results in amplified chromospheric emission, notably observable in the central regions of the Ca II H&K spectral lines, as indicated by Reinhold et al. (2017). The measure of the chromospheric emission strength is described by the Mount Wilson S-index

(Vaughan et al., 1978) or by the quantity R'_{HK} (Brandenburg et al., 2017). Vaughan & Preston (1980) investigated the chromospheric activity levels in main-sequence F-G-K-M stars by measuring the chromospheric CaII H&K emission fluxes. They noted that these stars display varying degrees of chromospheric activity and observed a noticeable lack in the number of F-G stars displaying intermediate activity compared to both highly active and less active stars. They suggested that the absence of such stars could be attributed to a decline in chromospheric activity as the stars age. Noyes et al. (1984a) examined the relationship between chromospheric activity, specifically the R'_{HK} activity index, and the Rossby number Ro = P_{rot}/τ_c for a sample of main-sequence stars of spectral type F or later, where P_{rot} is the rotational period of the star and τ_c is a theoretically derived convective turnover time. They found a strong correlation between the R'_{HK} activity index and the Rossby number. However, in contrast to the findings of Vaughan & Preston (1980), Noyes et al. (1984a) did not find any signs of the "Vaughan-Preston gap". Noyes et al. (1984b) investigated the empirical relation between rotation period P_{rot}, spectral type, and activity cycle period P_{cyc} for 13 slowly rotating main-sequence stars. They found that the cycle period is related to the rotation period by a power law: $P_{cyc} \propto P_{rot}^{1.25}$. This relationship can alternatively be expressed as $P_{cyc} \approx Ro^{1.25} \approx (P_{rot}/\tau_c)^{1.25}$ (Brandenburg et al., 2017; Mittag et al., 2023). For stars of spectral type G0-K5, Baliunas et al. (1995) observed a pattern of variation in the rotation period and the measure of chromospheric activity (S-index). Their research revealed that the chromospheric activity levels were high in young stars with fast rotation periods. Chromospheric activity and rotation rates of stars in the intermediate age range were average. Alternatively, the chromospheric activity levels were low in old stars with slow rotation periods. This observation supports the existence of the Vaughan-Preston gap, indicating that chromospheric activity and rotation change over time as the stars age. The relation between rotation periods and activity cycles of a sample of stars was investigated by Baliunas et al. (1996), who discovered a correlation between the two variables. In particular, they observed that stars with slower rotation periods exhibit longer activity cycles, while stars with faster rotation periods tend to have shorter activity cycles. According to Oláh & Strassmeier (2002), the relation between rotation periods and cycle lengths is more evident for stars with shorter activity cycles. However, the association becomes less clear for longer cycle lengths when considering more recent findings on the time variability of solar cycles.

In order to provide background of results in this field of research we now discuss previous literature. Vida et al. (2013) investigated the behaviour and activity cycles of four fast-rotating late-type stars with ($P_{rot} \leq 0.5$ days), highlighting the presence of 1-year cycles and the correlation between rotation rate and cycle length. Vida et al. (2014) used the short-term Fourier transform, a time-frequency analysis method, to examine the light

curves of 39 fast-rotating late-type active stars with rotation periods of less than one day. Nine of the selected stars showed indications of activity cycles with periods between 300 and 900 days. These cycles were inferred based on the observed variations in the typical latitude of the starspots. These variations, along with the differential rotation of the stellar surface, result in changes in the observed rotation period during the activity cycle. This variation in the rotation period was attributed to the movement and evolution of starspots at different latitudes of the star.

Reinhold et al. (2017) used four years of Kepler data to determine the cyclic variations in the amplitude of the light curve and the rotation period of stars by analysing a sample of active stars and calculating the rotation period and variability amplitude for each star in each Kepler quarter. Then they searched for periodic variations in these time series using Lomb-Scargle periodograms and employed a false alarm probability (FAP) criterion for selection. The study's findings indicate that amplitude periodicities, associated with underlying activity cycles, are detected in 3203 stars with cycle periods ranging from 0.5 to 6 years and rotation periods ranging from 1 to 40 days. According to Brandenburg et al. (2017) analysis of new observations and previous data, the longer and shorter cycle periods closely match expectations based on the average activity levels and rotation periods, which indicates a connection between stellar activity and stellar rotation.

Baliunas et al. (1995) reported an activity cycle of 11.6 years in the F-type star τ Boo (HD 120136). However, the authors assigned a FAP "poor" grade to this finding. Mittag et al. (2017b) detected an activity cycle with a duration of 122 days in their analysis of the S-index data of τ Boo. This short activity cycle periods suggest that τ Boo may exhibit variations on a relatively short timescale. Mittag et al. (2019a) focused on exploring the presence of short-term activity cycles in F-type stars, specifically using S-index time series data obtained with the TIGRE telescope. They utilized the generalized Lomb-Scargle periodogram method to analyze the data and search for periodic variations with a maximum length of 2 years. Their sample of F-type stars identified four stars that exhibited cyclic variations with periods of less than a year. However, compared to solar-type stars with well-developed cyclic activity, the amplitude of these short-term cyclic variations in F-type stars was smaller. Based on their findings, Mittag et al. (2019a) concluded that the activity behaviour among F-type stars differs from that of the Sun and cooler main sequence stars.

By studying 44 main-sequence stars with confirmed activity cycles, and rotation periods, Mittag et al. (2023) examined the relation between the length of the activity cycle and the Rossby number (Ro). They used empirical turnover periods based on the B-V colour index to calculate Rossby numbers, from which they deduced an empirical relationship between the Rossby number and the cycle duration. The study showed linear behaviour

in the double-logarithmic relationship between the Rossby number and cycle period. In addition, the relative convection zone depth was found to be correlated with cycle length and convective turnover time.

Besides the 11-year solar cycle, shorter cycles were discovered called the Rieger cycles. The original Rieger cycles were first identified in the Sun by Rieger et al. (1984) with a specific periodicity of approximately 154 days for flare occurrences. The Rieger-type cycles (RTCs) encompass cycles with periods (PRTC) ranging from 109 to 276 days. These RTCs were observed in various phenomena beyond solar flares, such as solar magnetic field and sunspot indexes, indicating their widespread nature. The underlying nature of RTCs remains unclear. The RTCs become more pronounced during the solar activity maximum. There is a potential connection between RTCs and the modulation of the solar magnetic dynamo process, as discussed in Arkhypov & Khodachenko (2021) and references therein. Possible reasons encompass the role of inertial g- and r-waves, also known as Rossby waves, as modulators of the emergence of magnetic flux in the Sun. Arkhypov & Khodachenko (2021) analyze photometric data from 1726 main-sequence stars with varying effective temperatures and rotation periods to study RTCs in other stars. Two types of RTCs are identified among the surveyed stars. The activity cycles with RTC periods (P_{RTC}) are independent of the stellar rotation period and are suggested to be driven by Kelvin waves. The second type are activity cycles with P_{RTC} proportional to the stellar rotation period and are suggested to be driven by Rossby waves.

The Parker (1955) model of the α–Ω dynamo introduced the concept of migratory dynamo waves, which play a crucial role in generating the observed solar cycle (Mittag et al., 2023). The α–effect, arising from the twisting of rising magnetic field tubes due to Coriolis forces, creates the poloidal magnetic field required for the next sunspot cycle. This effect is responsible for the reversal of magnetic polarities between successive cycles (Parker, 1955; Mittag et al., 2023). On the other hand, the Ω–effect, resulting from the differential rotation of the star, generates a toroidal magnetic field by stretching the magnetic field lines in a longitudinal direction. The combination of the α–effect and the Ω–effect leads to the formation of migratory dynamo waves, where the toroidal field is periodically regenerated and transformed into the poloidal field through the action of the α–effect. These migratory dynamo waves propagate and interact within the star's convective zone, causing the cyclic variations in the magnetic field (Mittag et al., 2023).

Now we describe existing theoretical knowledge about the possible relation between the magnetic cycle period and the rotation period of a star. In this context, according to Noyes et al. (1984b), the magnetic cycle period for G and K dwarfs, with convective turnover times (τ_{c}) between 11 and 26 days, is found to depend on the rotation period as

follows:

$$1/P_{\text{cyc}} \propto (\tau_{\text{c}}/P_{\text{rot}})^n, \tag{4.1}$$

where n is 1.25.

Simple dynamo models were discussed for understanding stellar magnetic activity and their implications for magnetic cycle periods in stars. Stix (1981) derived an equation to determine the critical dynamo number D_{crit} given by

$$D_{\text{crit}} \sim (\Omega\tau_c)^2 \times \left(\frac{R_\star}{l}\right)^3, \tag{4.2}$$

where $(\Omega\tau_c)^2$ is the inverse squared Rossby number and $R_\star/l$ is the relative depth of turbulence. suggesting that the occurrence of dynamo action is contingent upon the interplay between stellar rotation and stellar structure.

Parker (1955) provides relation for the magnetic cycle frequency, $\omega_{\text{mag\_cyc}}$, that involves the shear, H, and the α-effect. Stix (1976) presented an equivalent expression for the magnetic cycle frequency derived by Parker (1955), in terms of angular velocity gradient, Ω', given by

$$\omega_{\text{mag\_cyc}} = |\alpha\Omega'|^{\frac{1}{2}}, \tag{4.3}$$

indicating a proportional relationship between the cycle frequency and rotation frequency. Based on the model's assumptions equation 4.3 can be written as

$$P_{\text{mag\_cyc}} = 2P_{\text{cyc}} \approx \sqrt{\frac{R_\star}{l}}P_{\text{rot}}. \tag{4.4}$$

where l here is the length scale of turbulence and $R_\star$ is the stellar radius. This equation indicate the theoretical prediction of the relation between star's activity cycle and its rotation periods, which is equation (6) in Mittag et al. (2023).

According to the simple theoretical arguments quoted by Mittag et al. (2023), the magnetic cycle period $P_{\text{mag\_cyc}}$ is proportional to the rotation period P_{rot}. However, there is a modifying factor, $l/R_\star$ the relative depth of turbulence, which depends on the stellar structure, which itself may depend on the effective temperature or B-V color index of the star. This factor is expected to vary among different stars, especially those with different sizes, masses, and ages. The smallness of the inverse relative depth of the turbulence ensures that the period of the magnetic activity cycle $P_{\text{mag\_cyc}}$ is small. However, precisely what factors guarantee smallness of $R_\star/l$ in a particular star is poorly understood. That is why it is unclear why stars with very short activity cycles, studied in this paper, exist. All we can surmise is that the above theoretical arguments suggest $P_{\text{mag\_cyc}}$ should scale as $\propto \sqrt{R_\star/l}$.

Activity cycles, characterised by variations in magnetic activity over time, are essential for understanding the fundamental mechanisms that drive the magnetic fields of stars. A range of methodologies exist for the identification of activity cycles in stars. One such approach involves integrated flux measurements by continuously monitoring the total amount of energy emitted by a star, enabling the detection of variations in its magnetic activity (Kopp et al., 2016; Reinhold et al., 2020). Another approach is the analysis of chromospheric emission lines from the outer atmosphere of a star. Additionally, tracking of starspots by observing the movement and changes in starspots on a star's surface serves as an indicator for fluctuations in magnetic activity (Montet et al., 2017). Nevertheless, it is important to acknowledge that these techniques include limitations regarding photometric precision and the small sample size in spectroscopic observations (Scoggins et al., 2019). An alternative approach involves detecting flares. Flares are a frequently observed phenomenon resulting from magnetic activity and are easier to detect, even at significant distances from stars. Wide-field photometric surveys allow for simultaneous monitoring of stars, making it possible to survey them for flare activity (Scoggins et al., 2019). The Sun experiences variations in its flare rate by a factor of 10 between the solar maximum and minimum activity periods. Scoggins et al. (2019) focused on fluctuations in the frequency of flares from stars detected by the Kepler mission. The study examined a sample of 347 flare stars, which were selected based on having measured Kepler rotation periods, a minimum of 100 candidate flare events. Scoggins et al. (2019) aimed to identify coherent variations in flare activity among these stars by computing the fractional luminosity emitted in flares. One star, KIC 8507979, was identified as the best candidate for flare activity variation. This star has a rotation period of 1.2 days and emits an average of 0.82 flares per day with energies exceeding 10^{32} erg over the 18 Kepler quarters. The study observed a decline in flare activity from KIC 8507979 over time. Although the flare census derived from the Kepler light curve of this star did not provide definitive evidence for a stellar activity cycle, the observed variation of approximately 0.1 dex per year was consistent with cyclic behavior over ten years or more.

The motivation for the work in this chapter is as follows: In chapter 2, we looked for super-flares on different types of stars and focused on G-type dwarfs using entire Kepler data to study various aspects of statistical properties of the occurrence rate of super-flares. In chapter 3, as a by-product, we found thirteen peculiar Kepler IDs that are Sun-like, slowly rotating with rotation periods of 24.5 to 44 days, and yet can produce a super-flare and six G-type and four M-type Kepler IDs with exceptionally large amplitude super-flares. As noted previously, these detection defy our current understanding of stars and hence deserve a further investigation. In this chapter, we use the same data set as in chapter 2 in order to study empirical connection between a star's activity cycle and

rotation periods for a sample of F and G main sequence stars with rotation periods of less than one day. In this chapter, our aim is to provide predictions for very short activity cycle cases in a tabular form and to investigate in the future whether these short activity cycles are a common phenomenon in these stars or not.

Section 4.3 presents the method used in this work which includes the reproduction of Mittag et al. (2023) fit, the data representation and fit and the target selection method. The main findings of the study are presented in Section 4.4, and section 4.5 concludes this work with our main conclusions.

4.3 Methods

In our study, we adopt the terminology used by Brandenburg et al. (2017); Mittag et al. (2023) to categorize branches into two types: the "inactive" branch, referred to as the short-cycle branch P_{cyc}^S and the "active" branch, referred to as the long-cycle branch P_{cyc}^L. These terms were introduced first in Brandenburg et al. (2017). According to Mittag et al. (2023) this notation is more accurate and aligned with the actual characteristics of the branches. Therefore, they suggested that these terms should be used in future studies to refer to the two branches.

4.3.1 Reproduction of Mittag et al. (2023) P_{cyc}^S vs. P_{rot} Fit

In this subsection, we reproduced the fit between P_{cyc}^S and P_{rot} data from Mittag et al. (2023) to derive the fit parameters. First, we collected the data in Table 4.1, the first 32 rows are the observed activity cycle on the short-cycle branch P_{cyc}^S from Mittag et al. (2023) Table 1, along with the 32 corresponding rotation periods P_{rot}. These cycle lengths and rotation periods can be found in Table 1. Then we plotted in logarithmic scale the rotation periods on the x-axis versus the calculated cycle period on the y-axis as shown in Figure 4.1, using the empirical relation in Mittag et al. (2023) between the cycle periods and rotation periods in logarithmic terms that is given by:

$$\log P_{\mathrm{cyc}} \approx a + n \log P_{\mathrm{rot}}. \tag{4.5}$$

Since the theoretical relation, equation 4.4 implies a linear connection between P_{cyc} and P_{rot}, we fitted the data using Python *least-square* fit, a common technique for determining the best-fitting parameters for a given model, for two different slope adjustments as in Mittag et al. (2023). Also, we computed the R^2 *coefficient of determination* to measure how well the model fits the data. A R^2 value of 1 means that the predictions from the

regression fit the data perfectly. First, we set the slope n to be 1 and deduced the value of a parameter as $a = 1.918 \pm 0.027$ and the value of $R^2 = 0.87$. The red line in Figure 4.1 illustrates this trend. Then we repeated the fit by treating slope n as an independent variable to derive a and n values as equation 4.5 now becomes:

$$\log P_{\text{cyc}} \approx (1.488 \pm 0.092) + (1.324 \pm 0.067) \log P_{\text{rot}}. \tag{4.6}$$

and the value of $R^2 = 0.93$. The fit given by Equation 4.6 is identical to that of Mittag et al. (2023). The blue line in Figure 4.1 represents this fit. It is obvious that the $n = 1$ relation does not fit the short periods data, as Mittag et al. (2023) pointed out.
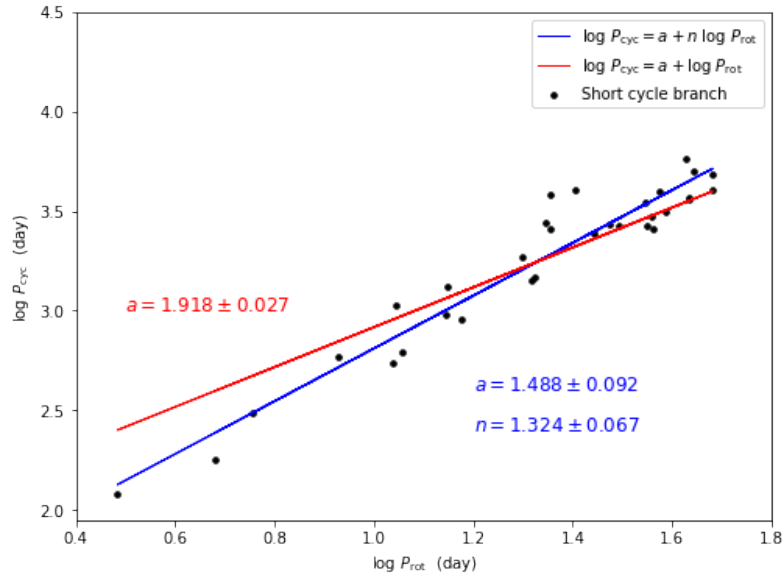

Figure 4.1: Log-scale of rotation period versus log-scale of observed activity cycle period (short cycle branch) for a sample of stars taken from Mittag et al. (2023). The deduced fit of P_{rot} vs. P_{cyc} relation are shown as solid lines. The blue line shows the fit when slope n is treated as an independent parameter while the red line shows the fit with a fixed slope of $n=1$.

4.3.2 Data representation and fit

In this subsection, we repeat the fit between P_{rot} and P_{cyc}^S using a larger data sample, taken from Mittag et al. (2023) and other previous studies.

This sample, shown in Table4.1, contains 92 P_{rot} and their 92 corresponding P_{cyc}^S. In addition to the 32 observed activity cycles in Mittag et al. (2023), we aggregated 32 activity cycles on the short-cycle branch P_{cyc}^S computed by Mittag et al. (2023) together with the corresponding 32 rotation periods P_{rot}. Furthermore, we included 28 activity

cycles and their corresponding rotation periods that were collected from various other studies. Thses P_{cyc}^S were taken from Ferreira Lopes et al. (2015); Egeland et al. (2015); Boro Saikia et al. (2016); Flores et al. (2016); Brandenburg et al. (2017); Mittag et al. (2019a) The star ID, effective temperature (T_{eff}), color index (B-V), P_{rot} and P_{cyc} are shown in Table4.1. Unavailable data is left blank in the table. It should be noted that we used in the fit two P_{cyc}^S values for each of the 32 stars IDs in Mittag et al. (2023), one was the observed P_{cyc}^S by a previous study, and the other was the calculated P_{cyc}^S by Mittag et al. (2023). Except for HD 16673 for which we collected three P_{cyc}^S due to the multiple sources, as shown in Table 4.1. References for each P_{rot} and P_{cyc}^S are shown in Table 4.1.

In the same way as in subsection 4.3.1, we used the empirical relation between P_{rot} and P_{cyc} in logarithmic scale given by equation 4.5 using the new data set in Table4.1 to produce the fit parameters a and n. We performed a *least-square* fit in Python to fit the data using two different slope adjustments again, one with a fixed slope n of 1 and another with the n treated as a free variable. This fit is shown in Figure 4.2. For the fit with a fixed slope of 1, we determined the value for the parameter a= 1.890 $\pm$ 0.024 and R^2= 0.83. This trend is shown by the red line in Figure 4.2. While for the fit with the slope n treated as a free variable, we deduced values for the parameters a and n as a=1.585 $\pm$ 0.064, n=1.256 $\pm$ 0.051 and R^2= 0.87. This fit is represented by the blue line in Figure 4.2. So that equation4.5 becomes now

$$\log P_{cyc} \approx (1.585 \pm 0.064) + (1.256 \pm 0.051) \log P_{rot}. \tag{4.7}$$

We note that our value of $n = 1.256 \pm 0.051$ with the extended dataset is closer to Noyes et al. (1984b)'s $n = 1.25$ than Mittag et al. (2023)'s $n = 1.324 \pm 0.067$.

Table 4.1: list of star IDs with their parameters, used in previous studies.

HD/KIC	T_{eff}	B-V	P_{rot}[d]	Ref	P_{cyc}^S[yr]	Ref
Sun	5777	0.642	25.4±1	1	11±2	1
HD 3651	5211	0.85	44	1	13.8±0.4	1
HD 4628	5120	0.89	38.5±2.1	1	8.6±0.1	1
HD 10476	5244	0.836	35.2±1.6	1	9.6±0.1	1
HD 10780	5321	0.804	22.14±0.55	2	7.53±0.16	2
HD 16160	5060	0.918	48±4.7	1	13.2±0.2	1
HD 16673	6183	0.524	5.7	3	0.847±0.006	5
HD 17051	6045	0.561	8.5±0.1	1	1.6	1
HD 22049	5140	0.881	11.1±0.1	1	2.9±0.1	1
Continued on next page						

Table 4.1 – continued from previous page

HD/KIC	T_{eff}	B-V	P_{rot}[d]	Ref	P_{cyc}^{S}[yr]	Ref
HD 26965	5282	0.82	43	1	10.1±0.1	1
HD 30495	5804	0.632	11.4±0.2	1	1.7±0.3	1
HD 32147	4801	1.049	48	1	11.1±0.2	1
HD 43587	5876	0.61	22.6±1.9	4	10.44±3.03	4
HD 75332	6089	0.549	4.8	5	0.493±0.003	5
HD 75732	5167	0.869	37.4±0.5	6	10.9	13
HD 76151	5714	0.661	15	1	2.5±0.1	1
HD 100180	6013	0.57	14	1	3.6±0.1	1
HD 103095	5449	0.754	31	1	7.3±0.1	1
HD 120136	6245	0.508	3.05±0.01	7	0.333±0.002	7
HD 128621	5098	0.9	36.2±1.4	1	8.1±0.2	1
HD 140538	5645	0.684	20.71±0.32	8	3.88±0.02	8
HD 146233	5741	0.652	22.7±0.5	1	7.1	1
HD 149661	5265	0.827	21.1±1.4	1	4±0.1	1
HD 160346	4975	0.959	36.4±1.2	1	7±0.1	1
HD 165341 A	5188	0.86	19.9	1	5.1±0.1	1
HD 166620	5151	0.876	42.4±3.7	1	15.8±0.3	1
HD 185144	5366	0.786	27.7±0.77	2	6.66±0.05	2
HD 190406	5910	0.6	13.9±1.5	1	2.6±0.1	1
HD 201091	4764	1.069	35.4±9.2	1	7.3±0.1	1
HD 219834 B	5055	0.92	43	1	10±0.2	1
KIC 8006161	5234	0.84	29.8±3.1	1	7.4±1.2	1
KIC 10644253	5943	0.59	10.9±0.9	1	1.5±0.1	1
Sun	5777	0.642	25.4±1	1	10.3	14
HD 3651	5211	0.85	44	1	11.7	14
HD 4628	5120	0.89	38.5±2.1	1	9.9	14
HD 10476	5244	0.836	35.2±1.6	1	9.2	14
HD 10780	5321	0.804	22.14±0.55	2	5.6	14
HD 16160	5060	0.918	48±4.7	1	12.4	14
HD 16673	6183	0.524	5.7	3	0.9	15
HD 17051	6045	0.561	8.5±0.1	1	1.4	14
HD 22049	5140	0.881	11.1±0.1	1	2.6	14
HD 26965	5282	0.82	43	1	11.5	15
Continued on next page						

Table 4.1 – continued from previous page

HD/KIC	$T_{\rm eff}$	B-V	$P_{\rm rot}$[d]	Ref	P_{cyc}^{S}[yr]	Ref
HD 30495	5804	0.632	11.4±0.2	1	1.6	14
HD 32147	4801	1.049	48	1	11.7	15
HD 43587	5876	0.61	22.6±1.9	4	10.4	14
HD 75332	6089	0.549	4.8	5	0.5	15
HD 75732	5167	0.869	37.4±0.5	6	9.7	14
HD 76151	5714	0.661	15	1	2.4	14
HD 100180	6013	0.57	14	1	3.4	14
HD 103095	5449	0.754	31	1	9.6	14
HD 120136	6245	0.508	3.05±0.01	7	0.3	14
HD 128621	5098	0.9	36.2±1.4	1	9.2	14
HD 140538	5645	0.684	20.71±0.32	8	4.5	14
HD 146233	5741	0.652	22.7±0.5	1	7.2	14
HD 149661	5265	0.827	21.1±1.4	1	5.3	14
HD 160346	4975	0.959	36.4±1.2	1	9	14
HD 165341 A	5188	0.86	19.9	1	4.9	14
HD 166620	5151	0.876	42.4±3.7	1	11.1	14
HD 185144	5366	0.786	27.7±0.77	2	7.3	14
HD 190406	5910	0.6	13.9±1.5	1	2.6	14
HD 201091	4764	1.069	35.4±9.2	1	8.3	14
HD 219834 B	5055	0.92	43	1	11	15
KIC 8006161	5234	0.84	29.8±3.1	1	7.7	14
KIC 10644253	5943	0.59	10.9±0.9	1	1.8	14
102712791		0.277	0.96±0.03	9	0.09±0.008	9
102720703		0.514	10.2±0.6	9	1.781±0.356	9
102721955		0.431	2.17±0.06	9	0.512±0.055	9
102723038		1.404	8.6±0.5	9	0.575±0.019	9
102726103		0.767	3.7±0.1	9	0.759±0.058	9
102738457		0.592	12.9±0.6	9	0.655±0.06	9
102749950		0.657	5.4±0.2	9	1.118±0.071	9
102750723		1.143	1.44±0.02	9	0.29±0.019	9
102754736		0.48	6.9±0.3	9	0.321±0.022	9
102758108		0.641	6.1±0.2	9	1.682±0.151	9
102770332		2.055	4.2±0.1	9	1.162±0.112	9

Continued on next page

Table 4.1 – continued from previous page

HD/KIC	T_{eff}	B-V	P_{rot}[d]	Ref	P_{cyc}^S[yr]	Ref
102770893		0.874	4.3±0.2	9	1.17±0.123	9
102777006		1.177	1.33±0.02	9	0.277±0.022	9
102778595		1.157	11.8±0.7	9	0.551±0.041	9
102780281		1.304	3±0.1	9	0.301±0.022	9
61 Cygni A (HD 201091)	4545	1.069	35.7±1.9	10	7.2±1.3	10
HD 100563			7.73	5	0.61	5
HD 114710	5970	0.58	12.3±1.1	1	9.6±0.3	1
HD 128620	5809	0.71	22.5±5.9	1	19.2±0.7	1
HD 16673	6183	0.524	7.4±0.07	5	0.85	5
HD 201092	4040	1.37	37.8±7.4	1	11.7±0.4	1
HD 219834 A	5461	0.8	42	1	21	1
HD 49933			3.45	5	0.58	5
HD 78366	5915	0.63	9.7±0.6	1	5.9±0.1	1
HD 81809	5623	0.8	40.2±3	1	8.2±0.1	1
solar analog HD 30495	5826	0.632	11.36±0.17	11	1.67±0.35	11
solar analog HD 45184	5871	0.62	19.98±0.02	12	5.14	12
τ Boo		0.48	3.5	5	0.33	5

Notes: The table illustrates a list of stars ID with their corresponding B–V values, effective temperature T_{eff}, the rotation period P_{rot} with the reference number and the short branch cycle period P_{cyc}^S with the reference number.

References: (1) Brandenburg et al. (2017), (2) Olspert et al. (2018), (3) Noyes et al. (1984b), (4) Ferreira et al. (2020), (5) Mittag et al. (2019a), (6) Mittag et al. (2017a), (7) Mittag et al. (2017b), (8) Mittag et al. (2019b), (9) Ferreira Lopes et al. (2015), (10) Boro Saikia et al. (2016), (11) Egeland et al. (2015), (12) Flores et al. (2016) , (13) Baum et al. (2022), (14) Mittag et al. (2023).

4.3.3 Data Samples

One of the main challenges in studying the relation between cycle length and rotation period is the lack number of well-known and accurately measured activity cycles. This limitation introduces uncertainties in the derived empirical relations Mittag et al. (2023). To overcome these challenges, it is crucial to obtain more reliable cycle periods, particularly for long-period cycles. Achieving this requires long-term time series observations of stars to gather comprehensive and accurate data on their activity cycles Mittag et al. (2023). Therefore, when looking for activity cycles, it is more efficient to monitor fast-
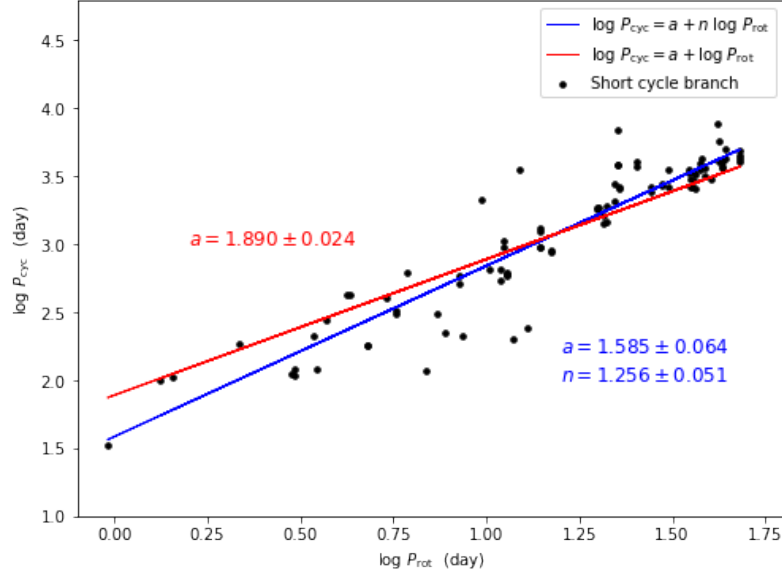
Figure 4.2: Log-scale of rotation period versus log-scale of cycle period (short cycle branch) for a 92 samples of stars taken from previous studies in Table 4.1. The deduced fit of P_{rot} vs. P_{cyc} relation are shown as solid lines. The blue line shows the fit where slope n is treated as an independent parameter while the red line shows the fit with a fixed slope of n=1.

rotating objects, as cycles can be discovered within a few years of observation, as opposed to stars with longer rotation periods Vida et al. (2013). For this reason, we chose our sample for this study to include fast-rotating main-sequence stars of type F and G from Kepler data with well-known rotation periods of less than one day. First, we collected all Kepler IDs which has well-known rotation periods. We then selected targets with rotation periods of less than a day. Using *Gaia* Data Release 2 (*Gaia*-DR2), we identified F- and G-type main sequence stars by their effective temperatures and radius based on the Harvard Spectral classification. The ranges of the effective temperature are 6000-7500 K and 5200-6000 K for F and G types, respectively. We thus obtained a total of 811 Kepler IDs of F- and G- type stars with less than one day rotation period. By using the radius restriction of the main-sequence stars as 1.15-1.4 $R_\odot$ and 0.96-1.15 $R_\odot$ for F and G types, respectively, the final data sample reduced to 138 Kepler targets with a number of 83 F-type and 55 G-type main-sequence stars. 71.74% of the rotation periods for these stars were taken from McQuillan et al. (2014). 15.94% from Santos et al. (2021), 5.07% from Reinhold & Gizon (2015), 4.35% from Chowdhury et al. (2018) and 2.90% from Yang & Liu (2019a). These 138 Kepler targets are listed in Table 4.2 with their effective temperature, radius, rotation period and the references for these rotation periods.

4.4 Results

Using a data set of 138 Kepler IDs with P_{rot} ranging from 0.202 d to 0.997 d, we provide a prediction for the corresponding value of their P_{cyc}^{S}, by applying the empirical relation between P_{cyc} and P_{rot} with the derived parameters in equation 4.7. Hence we obtained the predicted values of P_{cyc} from

$$P_{\mathrm{cyc}} \approx 10^{(1.585\pm0.064)+(1.256\pm0.051)\log P_{\mathrm{rot}}}. \tag{4.8}$$

From equation 4.8, we calculated 138 P_{cyc} for 83 F-type and 55 G-type main-sequence stars whose rotation period is less than a day. The shortest P_{cyc} is equal to 5.09 d while the longest P_{cyc} is equal to 38.46 d. All the 138 predicted P_{cyc} are listed in Table 4.2

Table 4.2: lists of the 138 Kepler IDs with their parameters and predicted P_{cyc}.

KIC	T_{eff}	$R_{\odot}$	P_{rot}[d]	Ref	P_{cyc}[d]	KIC	T_{eff}	$R_{\odot}$	P_{rot}[d]	Ref	P_{cyc}[d]
757099	5521	1.05	0.36	1	10.66	6877871	6508	1.40	0.54	2	17.74
1028018	5544	1.14	0.62	2	21.10	6948098	6095	1.29	0.57	3	18.98
1721795	6534	1.31	0.89	2	33.22	6961285	5802	0.98	0.45	2	14.11
1872192	5316	0.98	0.67	2	23.26	6962901	5601	0.97	0.98	2	37.50
2557335	5568	1.01	0.24	2	6.41	7199002	6381	1.24	0.57	2	18.98
2558273	6673	1.35	0.99	2	37.98	7199013	5286	0.96	0.57	2	18.98
2715228	6374	1.30	0.99	1	37.98	7199037	6024	1.36	0.57	2	18.98
2715410	5997	1.11	0.90	1	33.69	7354297	5481	1.05	0.95	2	36.06
2849645	5424	1.06	1.00	2	38.46	7461022	6168	1.28	0.59	2	19.82
2985825	6783	1.23	0.94	3	35.58	7678509	6644	1.22	0.96	2	36.54
3124412	6302	1.21	0.93	1	35.11	7707736	5644	1.09	0.76	2	27.25
3241517	6283	1.34	0.78	3	28.15	7816211	6050	1.32	0.29	2	8.12
3352959	6476	1.37	0.76	2	27.25	7909399	6574	1.40	0.82	2	29.97
3356577	6746	1.39	0.63	4	21.53	7915824	6231	1.39	0.74	2	26.35
3448722	5872	1.13	0.41	2	12.55	7973882	5512	1.06	0.35	2	10.29
3448817	6792	1.33	0.95	4	36.06	8016369	6734	1.34	0.77	1	27.70
3459311	5789	1.05	0.98	2	37.50	8043256	6680	1.27	0.93	2	35.11
3550386	6006	1.30	0.32	2	9.19	8144578	6639	1.32	0.59	2	19.82
3836772	6210	1.32	0.69	2	24.13	8197275	5604	1.14	0.44	2	13.71
3869099	5607	1.01	0.29	2	8.12	8264155	6738	1.33	0.91	4	34.16
4175618	5369	1.05	0.41	2	12.55	8264659	5417	1.12	0.97	1	37.02
4283120	6202	1.25	0.52	2	16.92	8285970	5639	1.14	0.57	2	18.98
4374659	5824	1.03	0.23	2	6.07	8313378	6624	1.31	0.54	2	17.74
4386947	5681	1.14	0.65	2	22.39	8382253	5695	1.01	0.63	3	21.53
4464528	6392	1.38	0.22	2	5.74	8393626	5893	1.15	0.43	2	13.32
4464530	6545	1.30	0.22	2	5.74	8420730	5770	1.08	0.25	2	6.74
4570231	5661	0.99	0.54	1	17.74	8651921	6473	1.29	0.95	2	36.06
4660562	5677	0.96	0.77	1	27.70	8687209	5650	1.00	0.77	1	27.70
4762130	6202	1.35	0.80	2	29.06	8804962	6586	1.23	0.90	2	33.69
4774370	6546	1.36	0.93	2	35.11	8892124	5263	1.01	0.72	2	25.46
4816098	6239	1.29	0.95	1	36.06	8916436	6566	1.35	0.87	1	32.29
4850965	5503	1.04	0.61	2	20.67	9146690	5387	1.11	0.72	2	25.46

Continued on next page

Table 4.2 – continued from previous page

KIC	T_{eff}	$R_\odot$	P_{rot}[d]	Ref	P_{cyc}[d]	KIC	T_{eff}	$R_\odot$	P_{rot}[d]	Ref	P_{cyc}[d]
4949214	6511	1.36	0.92	2	34.64	9206726	6876	1.31	0.46	4	14.50
4949350	6587	1.40	0.88	2	32.75	9306290	5571	1.04	0.82	2	29.97
4949766	6587	1.39	0.81	2	29.52	9393015	5877	1.01	0.24	2	6.41
5038288	5785	0.99	0.88	2	32.75	9456932	5875	0.97	0.53	2	17.33
5107198	6077	1.36	0.36	2	10.66	9474101	5945	1.10	0.21	2	5.42
5273178	6774	1.32	0.88	2	32.75	9594038	6694	1.31	0.94	4	35.58
5397765	6251	1.34	0.94	2	35.58	9640204	6620	1.33	0.53	2	17.33
5426665	6323	1.38	0.39	2	11.79	9640472	6076	1.34	0.34	2	9.92
5444276	6475	1.31	0.71	2	25.01	9710612	5867	1.08	0.39	2	11.79
5450307	6398	1.24	0.99	3	37.98	9730249	6479	1.34	0.91	2	34.16
5480545	6535	1.31	0.93	2	35.11	9896552	6279	1.26	0.87	1	32.29
5514866	5487	0.97	0.28	2	7.77	9897710	5840	1.08	0.43	2	13.32
5514871	5220	1.06	0.28	2	7.77	9965888	5589	1.13	0.31	2	8.83
5543840	6518	1.20	0.82	2	29.97	9970838	6429	1.25	0.96	2	36.54
5623538	6729	1.32	0.99	1	37.98	10023062	6469	1.38	0.89	2	33.22
5623852	5886	1.10	0.57	2	18.98	10134084	5926	1.00	0.55	5	18.15
5629449	6897	1.31	0.71	1	25.01	10490282	5504	1.05	0.79	2	28.60
5646176	6302	1.20	0.99	1	37.98	10614890	5283	1.06	1.00	2	38.46
5795235	6517	1.36	0.91	2	34.16	10809099	6051	1.31	0.91	2	34.16
5898014	6697	1.35	0.83	2	30.43	11017401	5648	1.09	0.80	2	29.06
5988566	6299	1.20	0.44	2	13.71	11018874	6454	1.30	0.99	2	37.98
6114118	6234	1.24	0.94	2	35.58	11247377	6184	1.38	0.40	2	12.17
6114140	6384	1.16	0.93	3	35.11	11349677	6076	1.23	0.84	1	30.90
6145032	6315	1.28	0.81	1	29.52	11400413	6781	1.34	0.76	4	27.25
6149358	6660	1.28	0.89	2	33.22	11498689	5464	1.10	0.31	2	8.83
6219870	5663	1.05	0.81	1	29.52	11653059	6160	1.26	0.29	2	8.12
6224148	6230	1.18	0.20	2	5.09	11924842	5494	1.13	0.84	5	30.90
6385867	5306	1.06	0.58	1	19.40	11969131	6444	1.23	0.63	1	21.53
6386598	6658	1.37	0.76	2	27.25	12067121	6211	1.33	0.43	5	13.32
6391602	5782	0.99	0.42	2	12.94	12108612	5695	1.09	0.71	2	25.01
6421219	6191	1.36	0.79	2	28.60	12119534	5296	0.98	0.64	2	21.96
6449077	6366	1.31	0.94	2	35.58	12121738	6134	1.31	0.73	2	25.90
6529902	6604	1.38	0.29	2	8.12	12157161	6513	1.26	0.78	2	28.15

Continued on next page

Table 4.2 – continued from previous page

KIC	T_{eff}	$R_{\odot}$	P_{rot}[d]	Ref	P_{cyc}[d]	KIC	T_{eff}	$R_{\odot}$	P_{rot}[d]	Ref	P_{cyc}[d]
6693864	6846	1.35	0.86	1	31.82	12157799	6117	1.17	0.89	5	33.22
6836589	5628	1.15	0.73	2	25.90	12354328	5251	0.97	0.81	2	29.52
6846595	6718	1.26	0.99	1	37.98	12356839	5605	1.14	0.35	2	10.29
6854461	6547	1.39	0.95	3	36.06	12418959	6427	1.36	0.78	2	28.15

Notes: Effective temperature T_{eff} and radius $R_{\odot}$ was taken from (*Gaia*-DR2).

References: (1) Santos et al. (2021), (2) McQuillan et al. (2014), (3) Reinhold & Gizon (2015), (4) Chowdhury et al. (2018), (5) Yang & Liu (2019a).

After predicting the values of the activity cycles for our extended, compared to Mittag et al. (2023), data sample, we wish to examine the theoretical prediction given by Equation 4.4 on short $P_{\text{cyc}} < 1$ yr. This is because the latter equation is a theoretical prediction, based on first physical principles, as opposed to empirical fit, which lacks any theoretical or conceptual justification. Therefore, we focused on the activity cycles derived from previous studies, as presented in Table 1. We chose 20 stars whose P_{cyc} is less than a year and plot the fit between P_{rot} and P_{cyc} as shown in Figure 4.3 using a simple linear regression without an intercept given by

$$P_{\text{cyc}} \, [\text{yr}] = n \, P_{\text{rot}} \, [\text{d}]. \tag{4.9}$$

We obtained the slope $n = 0.081 \pm 0.009$ and R^2 value is 0.997. Although the R^2 value for the fit is near unity, there is a large scatter indicating a poor quality fit. Note that P_{cyc} here is in years, as in Figure 14 from Mittag et al. (2019a). Therefore, for the lower and upper bounds of our 138 Kepler IDs with P_{rot} ranging from 0.202 d to 0.997 d, this simple theoretically justified equation predicts for $P_{\text{cyc}} = 0.081 \times 0.202 \times 365.25 = 5.98$ d and $0.081 \times 0.997 \times 365.25 = 29.50$ d, which are not very different from applying the more accurate powerlaw fit using equation 4.8 of 5.09 d and 38.46 d, respectively.

4.5 Conclusions

In chapter 4, we studied the empirical relation between star activity cycle and rotation period. First, we reproduced the fit between P_{rot} and P_{cyc} using Mittag et al. (2023) data and obtained the following fit parameters $\log P_{\text{cyc}} \approx (1.488 \pm 0.092) + (1.324 \pm 0.067) \log P_{\text{rot}}$, which are the same parameters as Mittag et al. (2023). Then, using a larger data set made up of P_{rot} and their associated P_{cyc} taken from prior studies, we
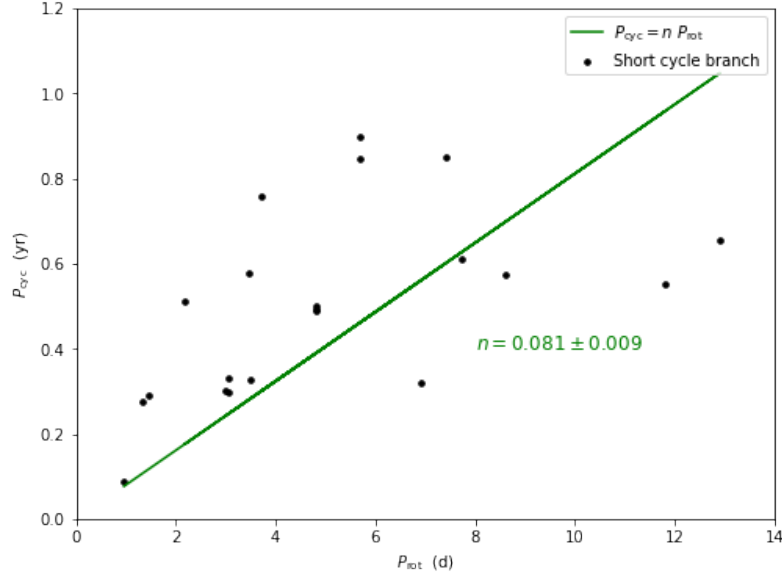
Figure 4.3: P_{rot} vs. P_{cyc} using a simple linear regression without an intercept for a sample of stars whose P_{cyc} is less than 1 year. The determined fit of P_{rot} vs. P_{cyc} relation are shown as a solid green line.

again re-examined the fit between P_{rot} and P_{cyc} and obtained the followinh fit parameters $\log P_{\text{cyc}} \approx (1.585 \pm 0.064) + (1.256 \pm 0.051) \log P_{\text{rot}}$. Using these new parameters, we applied this relation to a sample of 83 F-type and 55 G-type main sequence stars whose rotation periods of less than one day. The objective was to predict short activity cycles for these stars, aiming to ascertain in future studies if short activity cycles are a common occurrence in these stars or not. As a result we derived 138 predicted P_{cyc} ranging from 5.09 d to 38.46 d , which are listed in Table 4.2.

Usefulness of measuring short stellar activity cycles hinges on two main general difficulties:

(i) If monitoring program of stellar activity (e.g. activity-related chromospheric emission S-index or similar) is used as in references such as Mittag et al. (2019a); or Baum et al. (2022), then cadence time of observations is too long e.g. according to table 2 from the latter reference cadence could be 87 observations per year i.e. 365/87 = 4 days. Resolving activity cycles with $5.09 \leq P_{\text{cyc}} \leq 38.46$ d with such cadence would be nearly impossible.

(ii) If Kepler data light curves are used for e.g. plotting number of flares per day vs. time then large number of flare-detection would be necessary to have a reliable statistics. However, the problem is long cadence, 30 minutes, for the mainstream Kepler data. The photometer used by Kepler is sensitive to wavelengths ranging from 420 to 900 nm, covering the entire visible spectrum and a fraction of the infrared. The accuracy of the

photometer of Kepler is approximately 0.01% or 0.1 mmag, when 30-minute integration times are used while considering stars with a magnitude of 12. Kepler's 30-minute integration detected flare amplitudes less than 0.1% of the stellar value and energies of 2×10^{33} ergs. The duration of the flares ranged from one to three hours, with a rapid increase followed by a slow, exponential decline Maehara et al. (2012). When Kepler data is taken at a higher cadence or sampling rate of one minute, the accuracy of the measurements decreases. However, this higher cadence enables Kepler to detect flares that are too brief to be detected reliably using the main 30-minute integrations. With the one-minute cadence, Kepler can detect flares with energies as low as 10^{32} ergs Maehara et al. (2015).

It is worth noting that earlier studies exist using different observations where the energy involved in the observed transient brightening is estimated to range from 10^{25} to 10^{29} erg Shimizu (1995). Also, as far as the Sun is concerned, studies exist Mason et al. (2023) which consider flare frequency as a function of flare energy in the range 10^{27} to 10^{31} erg, but this is applicable to the Sun only.

In order to have a good statistics for Kepler IDs considered, we need to detect flares with energies 10^{27-32} ergs in order to see variation number of flares per day on a time scale of $5.09 \leq P_{\mathrm{cyc}} \leq 38.46$ d. To achieve this goal a new space mission is necessary with short time cadence (< 1 minutes) and photometric accuracy $< 0.01\%$.

A typical example of such a proposed hypothetical space mission would record data of the number of flares per day for each target. These data can be presented in bins of e.g. one-day width where the bin heights would show the number of flares detected in that bin. These bins would then show a periodic variation over time. Fitting a sinusoidal curve then would enable to deduce activity cycle period. Thus, through this periodic variation, we could potentially detect the target's magnetic activity cycle period. In some sense our approach is similar to Scoggins et al. (2019). However, their observation was so short in duration that only decrease in the flare activity was seen. A longer duration observations from a proposed new space mission would enable to see periodic variation and hence deduce the activity cycle period.

Alternative option could be making more short cadence ground-based s-index monitoring program of stellar activity with cadence ≈ 1 d or less. However it is unclear whether this is technically feasible. In any case, the present study provides predictions for $5.09 \leq P_{\mathrm{cyc}} \leq 38.46$ d and we hope that future either space or ground-based observational missions will put to test our predictions. Unitl such time the jury is still out.

5 Conclusions

Stellar flares are sudden and strong increases in brightness on the surface of a star, resulting from the release of magnetic energy during the reconnection of twisted magnetic fields in the outer atmospheres of stars. These events are known for their unpredictable and explosive nature. Stellar flares greatly affect the surrounding environment. Furthermore, the emission of flares can induce perturbations in the magnetic field of a star, resulting in the occurrence of stellar storms and coronal mass ejections. Super-flares represent extreme examples of stellar activity and magnetic energy release. By studying these events, we can gain a better understanding of the processes occurring within the Sun and other stars. Studying super-flares on stars of different ages and sizes, important information can be gained regarding the effects of magnetic activity and rotational speed on a star's evolution. Moreover, studying accelerated high-energy particles during a flare offers a significant understanding of astrophysical phenomena, such as magnetic reconnection and particle acceleration mechanisms.

In this thesis we conducted an automated search for super-flares on main-sequence stars of types A, F, G, K, and M in all of Kepler's long-cadence data of Data Release 25 from Q0 to Q17. This search was performed using a Python script that we wrote, following the technique described in the studies by Maehara et al. (2012); Shibayama et al. (2013). The Harvard Spectral classification was employed to ascertain the spectral type of each target by considering its effective temperature and radius. We investigated a total of 2,653, 10,898, 25,442, 10,307, and 2,222 main-sequence stars representing A, F, G, K, and M-type stars, respectively. As a result, during 1424 days of continual observation by Kepler, 4637 super-flares were detected on 1896 G-type dwarf stars. In this study, we analysed and compared the statistical characteristics of the occurrence frequency rate of super-flares using three different datasets: Q0-Q6, Q6-Q17, and Q0-Q17. The newly obtained data were utilised for this purpose. Based on our estimations on the Q0-Q17 dataset, it is determined that a super-flare, possessing an energy level of 10^{35} erg, occurs on G-type dwarfs approximately once every 4360 years. Upon conducting a comparative analysis of three distinct data sets, namely those ranging from 0-6, 7-17, and 0-17, it becomes evident that the statistical characteristics of flare occurrences exhibit a notable

resemblance. This observation suggests that the occurrence of flares remains consistent over a time range of 17 quarters. Furthermore, a comparative analysis was conducted between our findings with the data presented by Okamoto et al. (2021) in connection to the flare frequency distribution (FFD) and the power-law index (α). The findings of this thesis are in line with the previous research conducted by Okamoto et al. (2021). This indicates that the utilisation of a high-pass filter and the examination of sample biases in the analysis of super-flare occurrence rates, as conducted by Okamoto et al. (2021) while taking into account gyrochronology and the completeness of flare detection, did not significantly influence our ultimate findings. This serves as one of the driving factors behind our research. In addition, as shown in Table 2.7, we compared 183 analogous flare incidents to Okamoto et al. (2021), employing a case-by-case approach. In this thesis, the flare energy was overestimated when compared to Okamoto et al. (2021), with a correlation coefficient of 0.91 between the two energies. Despite employing a different catalogue of stellar parameters than Okamoto et al. (2021), the findings of this thesis broadly align with those of Okamoto et al. (2021). As seen in Table 2.7, the various star properties in the Gaia catalogue had no significant effect on the thesis findings. In addition, during the course of 1424 days of continuous monitoring, we found a total of 321, 1125, 4538, and 5445 super-flares on dwarfs of 136, 522, 770, and 312 A, F, K, and M type stars, respectively. We calculated the distributions of super-flare incidence rates as a function of superflare energy. We discovered that the flare frequency distribution as a function of flare energy follows a power-law relation with $dN/dE \propto E^{-\alpha}$ where α =2.0 to 2.1 for all spectral classes of stars, from F-type to M-type. This shows that the power-law index α has similarities to solar flare indices (α = -2) (Shibayama et al., 2013). The similarity of the power-law index values suggests that similar physical conditions, via the mechanism presumed to be magnetic reconnection, that cause the flares. The obtained value of alpha index 1.3 in the flare frequency distribution for A-type stars suggests that these stars' flare conditions are different from those of other stellar types. The observed similarity in power-law index values implies that flares are likely produced by similar physical conditions, specifically through the mechanism of magnetic reconnection. On the other hand, the calculated α index of 1.3 for the flare frequency distribution of A-type stars suggests that their flare conditions differ significantly from those observed in other types of stars. A notable increase in the occurrence rate of flares was recorded, ranging from 4.79 % to 14.04 % for F-type to M-type stars, respectively. Contrary to the theoretical expectation, the incidence rate of flares is higher in A-type stars (5.13 %) compared to F-type stars (4.79 %) (Yang & Liu, 2019a). The findings presented in this thesis exhibit a resemblance to the outcomes reported in previous research conducted by Balona (2015); Van Doorsselaere et al. (2017); Yang & Liu (2019a), but the difference is in that we used

significantly different flare detection algorithm and provided a useful for the community tool – an openly available Python script for super-flare detection.

Based on the available data, a total of 14 super-flares were found on 13 Sun-like stars with a surface temperature of $5600K \leqslant T_{\text{eff}} < 6000K$, and P_{rot} range from 24.5 to 44 days. Furthermore, our investigation yielded a total of 12 instances of large amplitude super-flares on six main-sequence stars of G type and seven instances on four main-sequence stars of M type. Main-sequence stars belonging to spectral classes A, F, and K exhibited no discernible indications of super-flares with large amplitudes. In order to characterise the flares, we employ a mathematical model that involves fitting an exponential decay function to the flare light curve. This function is represented by the equation $f(t) = a\, e^{-t/\tau} + b$. In this study, we investigate the correlation between the decay time of a flare following its peak, denoted as τ, and two variables: f_{amp} and E_{flare}. Specifically, we examine the relationship between τ and f_{amp}, as well as the relationship between τ and E_{flare}. In the case of Sun-like stars with slow rotation, it has been observed that there is a negative correlation between the amplitude of flares and the corresponding value of τ. Specifically, smaller flare amplitudes tend to be associated with larger values of τ, while larger flare amplitudes tend to be associated with smaller values of τ. In a similar manner, it can be observed that higher values of τ are indicative of lower flare energy, whereas lower values of τ are associated with higher flare energies. In the case of main sequence stars belonging to the G and M spectral types, there seems to be no discernible correlation between the parameter τ and the variables f_{amp} or E_{flare}. We conducted a series of experiments with various fit functions to analyse the relationship between τ and f_{amp}, as well as τ and E_{flare}. The purpose of these experiments was to gain a clearer understanding of the underlying pattern present in the data. Given that the coefficient of determination (R^2) is below 0.5 in these instances, it is not possible to establish a dependable functional relationship between these parameters. We believe that the thirteen slowly rotating Sun-like stars, with rotation periods ranging from 24.5 to 44 days, and yet being capable of producing super-flares with energies ranging from $(2 - 9) \times 10^{34}$ erg, along with the six G-type and four M-type Kepler IDs displaying exceptionally large amplitude super-flares with relative flux in the range of $\Delta F/F_{\text{avg}} = 4 - 35$, challenge our existing knowledge of stars. Therefore, we propose that these phenomena warrant further investigation.
There are several avenues for advancing the study of superflares using existing or forthcoming data. For example, Fig 3.4 shows short-duration flares, which seem to have a shape decay, which is probably a consequence of using 30 min cadence. Using higher cadence data with, e.g. TESS (2 min cadence) on these objects will give a much-improved flare light curve.

We studied the empirical relation between star activity cycle and rotation period. In this thesis, we reproduced the correlation between the rotation period (P_{rot}) and the period of the activity cycle (P_{cyc}) using the data provided by Mittag et al. (2023). The resulting fit parameters were determined to be

$\log P_{\mathrm{cyc}} \approx (1.488 \pm 0.092) + (1.324 \pm 0.067) \log P_{\mathrm{rot}}$.

Subsequently, a more extensive data set comprising of 92 instances of the rotational period (P_{rot}) and their corresponding 92 values of the period of the activity cycle (P_{cyc}), sourced from previous investigations, was utilised to reproduce the correlation between P_{rot} and P_{cyc}. The resulting fit parameters were determined as follows:

$\log P_{\mathrm{cyc}} \approx (1.585 \pm 0.064) + (1.256 \pm 0.051) \log P_{\mathrm{rot}}$.

We use these new parameters to examine the correlation between rotation periods and activity cycles in a sample of 83 F-type and 55 G-type main sequence stars. Specifically, we focused on stars with rotation periods of less than one day. This analysis aimed to generate tabular predictions for instances characterised by extremely short activity cycles. This would enable future investigations to ascertain the prevalence of such short activity cycles in these particular stars. We obtained a total of 138 estimated values for the period of the activity cycle (P_{cyc}) ranging from 5.09 days to 38.46 days. These values are presented in Table 4.2.

The usefulness of quantifying short-term stellar activity cycles is contingent upon two primary overarching challenges:

(i) If a monitoring programme for stellar activity, such as the activity-related chromospheric emission S-index or similar methods mentioned in previous studies Mittag et al. (2019a); Baum et al. (2022), is employed, it is observed that the cadence time for observations is relatively long. For instance, based on the information provided in Table 2 of the latter reference, the cadence could be approximately 87 observations per year, resulting in an interval of approximately 4 days between consecutive observations (365/87 = 4 days). It would be exceedingly challenging to resolve activity cycles within the range of $5.09 \leq P_{\mathrm{cyc}} \leq 38.46$ days using the given cadence.

(ii) If one were to utilise Kepler data light curves to create a plot depicting the number of flares per day as a function of time, a substantial quantity of flare detections would be required to obtain statistically significant results. Nevertheless, a significant issue arises in relation to the long cadence of Kepler data, which is equal to 30 minutes. The photometer employed by the Kepler mission exhibits sensitivity to wavelengths spanning from 420 to 900 nm, including the entirety of the visible spectrum and a portion of the infrared region. The photometer of Kepler has a precision of around 0.01% or 0.1 mmag, when employing 30-minute integration periods taking into account stars with 12 magnitudes.

The integration conducted by Kepler, which lasted for a duration of 30 minutes, successfully identified flare amplitudes that were less than 0.1% of the stellar value. Additionally, the discovered flares exhibited energy amounting to 2×10^{33} ergs. According to Maehara et al. (2012), the flares exhibited a length spanning from one to three hours, characterised by a rapid increase followed by gradual, exponential decay. When the Kepler data is obtained with a higher cadence or sampling rate of one minute, there is a drop in the precision of the measurements. Nevertheless, the higher cadence of Kepler allows for detecting flares that are too short in duration to be successfully identified using the 30-minute cadence. According to Maehara et al. (2015), Kepler has the capability to identify flares with energies as low as 10^{32} ergs, using one minute cadence.

It is noteworthy to mention that previous studies have been conducted using various observations, estimating the energy associated with the observed transient brightening to be within the range of 10^{25} to 10^{29} erg (Shimizu, 1995). Furthermore, there have been scholarly investigations conducted by Mason et al. (2023) that the flare frequency as a function of flare energy within the range of 10^{27} to 10^{31} erg, but this applies to the Sun only. To ensure the inclusion of reliable statistics for Kepler IDs, it is necessary to identify flares with energy levels ranging from 10^{27-32} ergs. This will enable the observation of the fluctuation in the number of flares every day within a time frame of $5.09 \leq P_{\mathrm{cyc}} \leq 38.46$ days. In order to accomplish this objective, it is imperative to undertake a novel space mission characterised by a short time cadence (< 1 minute) and a high level of precision in photometric measurements ($< 0.01\%$).

An illustrative instance of such a suggested hypothetical space mission would gather data on the frequency of flares per day for each designated objective. The data can be organised into bins with a width of one day, where the height of each bin represents the number of detected flares within that time period. Subsequently, these bins would exhibit a cyclical fluctuation throughout the duration. By fitting a sinusoidal curve, it would be possible to determine the period of the activity cycle. Hence, by observing this recurring fluctuation, we may potentially ascertain the duration of the target's magnetic activity cycle. Our technique resembles the methodology employed by Scoggins et al. (2019) to a certain extent. Nevertheless, their observation was of such brief length that just a reduction in the flare activity was observed. Extending the duration of observations from a proposed new space mission would allow for the detection of periodic variations and the determination of the duration of the activity cycle.

The choice of filters and wavelength bands can affect the detection sensitivity to certain types of flares, especially those with lower energy levels. Therefore, we require a space-based instrument capable of detecting low-energy flares. TESS observes stars in the red and near-infrared wavelengths using a susceptible red filter. However, this red filter may

limit TESS's sensitivity to short-duration and lower-energy flares that emit predominantly in the ultraviolet and blue parts of the spectrum. Flares with such features might be more easily observed in observations conducted with instruments designed for shorter wavelengths. Therefore, instrument manufacturers should consider the inclusion of multi-filters that cover the range of wavelengths from blue to red. Furthermore, estimating the black-body temperature of flares becomes more accurate when observed across a range of wavelengths. This can provide diversity of flare temperatures. Currently, we assume that all flares have the same temperature.

One potential alternative could involve the implementation of a ground-based s-index monitoring programme focused on shorter cadences, approximately ≤ 1 day, to see and track stellar activity. Nevertheless, there remains a lack of clarity regarding the technological feasibility of this matter. The thesis offers predictions within the range of $5.09 \leq P_{\mathrm{cyc}} \leq 38.46$ days. It is anticipated that forthcoming observational missions, whether conducted in space or on the ground, will assess the validity of these predictions. Until such time, the verdict remains uncertain.

Current and future space missions dedicated to exploring the Sun and stars are expected to collect unprecedented data and observations. Solar missions like the Solar Dynamics Observatory (SDO), the Parker Solar Probe (PSP), the Solar Orbiter and the Solar Terrestrial Relations Observatory (STEREO) provide valuable data to study solar flares, including the potential for super-flares on the Sun. Stellar missions such as the James Webb Space Telescope (JWST), the Swift Gamma-Ray Burst Mission, the Fermi Gamma-ray Space Telescope and the Nancy Grace Roman Space Telescope (WFIRST) will help to observe the high-energy emissions from stellar flares expand our understanding of stars, and the wider universe. Current and future observational space missions are essential to scientific research for testing hypotheses and predictions. Many hypotheses and predictions from studies presented in this thesis will be tested by possibly current and or, more likely future observational space missions. Observational space missions offer valuable opportunities to collect data and evidence that can either support or refute the claims made in the thesis. New telescopes and instruments are continuously being developed, each with unique capabilities for studying stellar flares and other astrophysical phenomena. The future of solar and stellar research is exciting and will offer many unseen discoveries and unravel yet unknown new observational findings.

Bibliography

Abed, A. K., Qahwaji, R., & Abed, A. 2021, Advances in Space Research, 67, 2544, doi: `10.1016/j.asr.2021.01.042`

Althukair, A., & Tsiklauri, D. 2023a, Main-sequence star super-flare frequency based on entire Kepler data, 1.0.0, Zenodo, doi: `10.5281/zenodo.7755912`

Althukair, A. K., & Tsiklauri, D. 2023b, Research in Astronomy and Astrophysics, 23, 085017, doi: `10.1088/1674-4527/acdc09`

—. 2023c, Research in Astronomy and Astrophysics, 23, 105010, doi: `10.1088/1674-4527/acee51`

—. 2023d, Research in Astronomy and Astrophysics, 23, 115015, doi: `10.1088/1674-4527/acf6b2`

Arkhypov, O. V., & Khodachenko, M. L. 2021, A&A, 651, A28, doi: `10.1051/0004-6361/202140629`

Aschwanden, M. J. 2005, Physics of the Solar Corona. An Introduction with Problems and Solutions (2nd edition)

Bai, J.-Y., & Esamdin, A. 2020, The Astrophysical Journal, 905, 110, doi: `10.3847/1538-4357/abc479`

Bak-Steślicka, U., Kołomański, S., & Mrozek, T. 2013, , 283, 505, doi: `10.1007/s11207-013-0251-6`

Baliunas, S. L., Nesme-Ribes, E., Sokoloff, D., & Soon, W. H. 1996, ApJ, 460, 848, doi: `10.1086/177014`

Baliunas, S. L., Donahue, R. A., Soon, W. H., et al. 1995, ApJ, 438, 269, doi: `10.1086/175072`

Balona, L. A. 2012, MNRAS, 423, 3420, doi: `10.1111/j.1365-2966.2012.21135.x`

—. 2013, MNRAS, 431, 2240, doi: `10.1093/mnras/stt322`

—. 2015, MNRAS, 447, 2714, doi: `10.1093/mnras/stu2651`

Basu, S., & Antia, H. 2008, Physics Reports, 457, 217, doi: `https://doi.org/10.1016/j.physrep.2007.12.002`

Bibliography

Baum, A. C., Wright, J. T., Luhn, J. K., & Isaacson, H. 2022, AJ, 163, 183, doi: `10.3847/1538-3881/ac5683`

Benz, A. 2002, Plasma Astrophysics, second edition, Vol. 279, doi: `10.1007/0-306-47719-X`

Benz, A. O. 2017, Living Reviews in Solar Physics, 14, 2, doi: `10.1007/s41116-016-0004-3`

Berger, T. A., Huber, D., Gaidos, E., & van Saders, J. L. 2018, ApJ, 866, 99, doi: `10.3847/1538-4357/aada83`

Bhatia, S. 2014, Advanced renewable energy systems,(Part 1 and 2) (CRC Press)

Bogdan, T. J., Gilman, P. A., Lerche, I., & Howard, R. 1988, ApJ, 327, 451, doi: `10.1086/166206`

Bonanno, A., Schlattl, H., & Paternò, L. 2002, A&A, 390, 1115, doi: `10.1051/0004-6361:20020749`

Borexino Collaboration, Agostini, M., Altenmüller, K., et al. 2018, Nature, 562, 505, doi: `10.1038/s41586-018-0624-y`

Borexino Collaboration, Agostini, M., Altenmüller, K., Appel, S., et al. 2020, Nature, 587, 577, doi: `10.1038/s41586-020-2934-0`

Boro Saikia, S., Jeffers, S. V., Morin, J., et al. 2016, A&A, 594, A29, doi: `10.1051/0004-6361/201628262`

Brandenburg, A., Mathur, S., & Metcalfe, T. S. 2017, ApJ, 845, 79, doi: `10.3847/1538-4357/aa7cfa`

Breton, S. N., Santos, A. R. G., Bugnet, L., et al. 2021, A&A, 647, A125, doi: `10.1051/0004-6361/202039947`

Broggini, C. 2003, in Physics in Collision, ed. I. Antoniou, V. A. Sadovnichy, & H. Walther, 21, doi: `10.48550/arXiv.astro-ph/0308537`

Browning, P. K., Gerrard, C., Hood, A. W., Kevis, R., & van der Linden, R. A. M. 2008, A&A, 485, 837, doi: `10.1051/0004-6361:20079192`

Browning, P. K., & Priest, E. R. 1984, A&A, 131, 283

Bryson, S. T., Jenkins, J. M., Klaus, T. C., et al. 2010, in Society of Photo-Optical Instrumentation Engineers (SPIE) Conference Series, Vol. 7740, Software and Cyberinfrastructure for Astronomy, ed. N. M. Radziwill & A. Bridger, 77401D, doi: `10.1117/12.857625`

Caldwell, D. A., Van Cleve, J. E., Jenkins, J. M., et al. 2010, in Space Telescopes and Instrumentation 2010: Optical, Infrared, and Millimeter Wave, Vol. 7731, SPIE, 343–353

Bibliography

Cameron, R. H., Dikpati, M., & Brandenburg, A. 2017, , 210, 367, doi: 10.1007/s11214-015-0230-3

Candelaresi, S., Hillier, A., Maehara, H., Brandenburg, A., & Shibata, K. 2014, ApJ, 792, 67, doi: 10.1088/0004-637X/792/1/67

Carmichael, H. 1964, in NASA Special Publication, Vol. 50, 451

Carrington, R. C. 1859, MNRAS, 20, 13, doi: 10.1093/mnras/20.1.13

Carroll, B. W., & Ostlie, D. A. 2017, An introduction to modern astrophysics, Second Edition

Chang, H.-Y., Lin, C.-L., Ip, W.-H., et al. 2018, The Astrophysical Journal, 867, 78, doi: 10.3847/1538-4357/aae2bc

Charbonneau, P. 2014, ARAA, 52, 251, doi: 10.1146/annurev-astro-081913-040012

Chen, H., Tian, H., Li, H., et al. 2022, ApJ, 933, 92, doi: 10.3847/1538-4357/ac739b

Chen, P. 2011, Living Reviews in Solar Physics, 8, 1

Chowdhury, S., Joshi, S., Engelbrecht, C. A., et al. 2018, , 363, 260, doi: 10.1007/s10509-018-3480-1

Cliver, E. W., Schrijver, C. J., Shibata, K., & Usoskin, I. G. 2022, Living Reviews in Solar Physics, 19, 2, doi: 10.1007/s41116-022-00033-8

Connelly, J. N., Bizzarro, M., Krot, A. N., et al. 2012, Science, 338, 651, doi: 10.1126/science.1226919

Curto, J. J. 2020, Journal of Space Weather and Space Climate, 10, 27, doi: 10.1051/swsc/2020027

Davenport, J. R. A. 2016, ApJ, 829, 23, doi: 10.3847/0004-637X/829/1/23

Davenport, J. R. A., Hawley, S. L., Hebb, L., et al. 2014, ApJ, 797, 122, doi: 10.1088/0004-637X/797/2/122

de Pontieu, B., McIntosh, S., Hansteen, V. H., et al. 2007, PASJ, 59, S655, doi: 10.1093/pasj/59.sp3.S655

Dennis, B. R. 1985, , 100, 465, doi: 10.1007/BF00158441

Ding, M. D., Fang, C., & Yun, H. S. 1999, ApJ, 512, 454, doi: 10.1086/306776

Domingo, V., Ermolli, I., Fox, P., et al. 2009, , 145, 337, doi: 10.1007/s11214-009-9562-1

Doyle, J. G., Irawati, P., Kolotkov, D. Y., et al. 2022, MNRAS, 514, 5178, doi: `10.1093/mnras/stac1695`

Doyle, L., Ramsay, G., & Doyle, J. G. 2020, MNRAS, 494, 3596, doi: `10.1093/mnras/staa923`

Doyle, L., Ramsay, G., Doyle, J. G., & Wu, K. 2019, MNRAS, 489, 437, doi: `10.1093/mnras/stz2205`

Eastwood, J. P., Biffis, E., Hapgood, M. A., et al. 2017, Risk Analysis, 37, 206, doi: `10.1111/risa.12765`

Egeland, R., Metcalfe, T. S., Hall, J. C., & Henry, G. W. 2015, ApJ, 812, 12, doi: `10.1088/0004-637X/812/1/12`

Erdélyi, R., & Ballai, I. 2007, Astronomische Nachrichten, 328, 726, doi: `10.1002/asna.200710803`

Fang, C., Chen, P.-F., Li, Z., et al. 2013, Research in Astronomy and Astrophysics, 13, 1509, doi: `10.1088/1674-4527/13/12/011`

Ferreira, R. R., Barbosa, R., Castro, M., et al. 2020, A&A, 640, A46, doi: `10.1051/0004-6361/201937219`

Ferreira Lopes, C. E., Leão, I. C., de Freitas, D. B., et al. 2015, A&A, 583, A134, doi: `10.1051/0004-6361/201424900`

Flores, M., González, J. F., Jaque Arancibia, M., Buccino, A., & Saffe, C. 2016, A&A, 589, A135, doi: `10.1051/0004-6361/201628145`

Forbes, T. G. 2000, , 105, 23153, doi: `10.1029/2000JA000005`

Gao, D.-Y., Liu, H.-G., Yang, M., & Zhou, J.-L. 2022, AJ, 164, 213, doi: `10.3847/1538-3881/ac937e`

García, R. A., Turck-Chièze, S., Jiménez-Reyes, S. J., et al. 2007, Science, 316, 1591, doi: `10.1126/science.1140598`

Genestreti, K., Kistler, L., & Mouikis, C. 2012, PhD thesis, doi: `10.13140/2.1.4788.2882`

Getman, K. V., Feigelson, E. D., Broos, P. S., Micela, G., & Garmire, G. P. 2008, ApJ, 688, 418, doi: `10.1086/592033`

Gilman, P. A. 2005, Astronomische Nachrichten, 326, 208, doi: `10.1002/asna.200410378`

Gopalswamy, N., Shimojo, M., Lu, W., et al. 2003, ApJ, 586, 562, doi: `10.1086/367614`

Gopalswamy, N., & Webb, D. F. 2009, Universal Heliophysical Processes (IAU S257)

Bibliography

Green, S. F., & Jones, M. H. 2015, An Introduction to the Sun and Stars (Cambridge University Press)

Grieder, P. K. F. 2001, Cosmic Rays at Earth, doi: 10.1016/B978-0-444-50710-5.X5000-3

Güdel, M., Audard, M., Reale, F., Skinner, S. L., & Linsky, J. L. 2004, A&A, 416, 713, doi: 10.1051/0004-6361:20031471

Gunár, S., Labrosse, N., Luna, M., et al. 2023, , 219, 33, doi: 10.1007/s11214-023-00976-w

Günther, M. N., Zhan, Z., Seager, S., et al. 2020, The Astronomical Journal, 159, 60

Hao, Q., Yang, K., Cheng, X., et al. 2017, Nature Communications, 8, 2202, doi: 10.1038/s41467-017-02343-0

Hathaway, D. H. 2015, Living Reviews in Solar Physics, 12, 4, doi: 10.1007/lrsp-2015-4

Hathaway, D. H., Wilson, R. M., & Reichmann, E. J. 2002, , 211, 357, doi: 10.1023/A:1022425402664

Hawley, S. 2000, Coordinated Observations of Stellar Flares on AD Leo, HST Proposal ID 8613. Cycle 9

Hawley, S. L., & Fisher, G. H. 1992, ApJS, 78, 565, doi: 10.1086/191640

Hawley, S. L., Allred, J. C., Johns-Krull, C. M., et al. 2003, ApJ, 597, 535, doi: 10.1086/378351

He, H., Wang, H., & Yun, D. 2015, ApJS, 221, 18, doi: 10.1088/0067-0049/221/1/18

He, H., Wang, H., Zhang, M., et al. 2018, ApJS, 236, 7, doi: 10.3847/1538-4365/aab779

Heinzel, P., Kleint, L., Kašparová, J., & Krucker, S. 2017, ApJ, 847, 48, doi: 10.3847/1538-4357/aa86ef

Heise, J., Brinkman, A. C., Schrijver, J., et al. 1975, ApJL, 202, L73, doi: 10.1086/181984

Heyvaerts, J., & Priest, E. R. 1983, A&A, 117, 220

Hirayama, T. 1974, , 34, 323, doi: 10.1007/BF00153671

Hodgson, R. 1859, MNRAS, 20, 15, doi: 10.1093/mnras/20.1.15

Howell, S. B., Sobeck, C., Haas, M., et al. 2014, PASP, 126, 398, doi: 10.1086/676406

Bibliography

Hoyng, P., Duijveman, A., Machado, M. E., et al. 1981, ApJL, 246, L155, doi: 10.1086/183574

Ilin, E., Poppenhaeger, K., Schmidt, S. J., et al. 2021, MNRAS, 507, 1723, doi: 10.1093/mnras/stab2159

Iwai, K., Shimojo, M., Asayama, S., et al. 2017, , 292, 22, doi: 10.1007/s11207-016-1044-5

Jackman, J. A. G., Wheatley, P. J., Bayliss, D., et al. 2019, MNRAS, 485, L136, doi: 10.1093/mnrasl/slz039

Jess, D. B., Morton, R. J., Verth, G., et al. 2015, , 190, 103, doi: 10.1007/s11214-015-0141-3

Jiang, Y., Zheng, R., Yang, J., et al. 2012, ApJ, 744, 50, doi: 10.1088/0004-637X/744/1/50

Karak, B. B., Käpylä, P. J., Käpylä, M. J., et al. 2015, A&A, 576, A26, doi: 10.1051/0004-6361/201424521

Karak, B. B., Tomar, A., & Vashishth, V. 2020, MNRAS, 491, 3155, doi: 10.1093/mnras/stz3220

Katsova, M. M., Kitchatinov, L. L., Livshits, M. A., et al. 2018, Astron. Rep., 62, 72

Kippenhahn, R., Weigert, A., & Weiss, A. 2013, Stellar Structure and Evolution, doi: 10.1007/978-3-642-30304-3

Kirkpatrick, J. D. 2005, Annu. Rev. Astron. Astrophys., 43, 195

Kirkpatrick, J. D., Gelino, C. R., Cushing, M. C., et al. 2012, ApJ, 753, 156, doi: 10.1088/0004-637X/753/2/156

Kitchatinov, L. L., Mordvinov, A. V., & Nepomnyashchikh, A. A. 2018, Astron. Astrophys., 615, A38, doi: 10.1051/0004-6361/201732549

Kitchatinov, L. L., & Olemskoy, S. 2016, Mon. Not. R. Astron. Soc., 459, 4353

Koch, D. G., Borucki, W. J., Basri, G., et al. 2010, The Astrophysical Journal Letters, 713, L79

Kopp, G., Krivova, N., Wu, C. J., & Lean, J. 2016, , 291, 2951, doi: 10.1007/s11207-016-0853-x

Kopp, R. A., & Pneuman, G. W. 1976, , 50, 85, doi: 10.1007/BF00206193

Koupelis, T. 2012, In quest of the universe (Jones & Bartlett Publishers)

Kretzschmar, M. 2011, A&A, 530, A84, doi: 10.1051/0004-6361/201015930

Lu, H.-p., Zhang, L.-y., Shi, J., et al. 2019, ApJS, 243, 28, doi: `10.3847/1538-4365/ab2f8f`

Machado, M. E., Avrett, E. H., Falciani, R., et al. 1986, in The Lower Atmosphere of Solar Flares, ed. D. F. Neidig & M. E. Machado, 483–488

Maehara, H., Notsu, Y., Notsu, S., et al. 2017, PASJ, 69, 41, doi: `10.1093/pasj/psx013`

Maehara, H., Shibayama, T., Notsu, Y., et al. 2015, Earth, Planets and Space, 67, 59, doi: `10.1186/s40623-015-0217-z`

Maehara, H., Shibayama, T., Notsu, S., et al. 2012, Nature, 485, 478, doi: `10.1038/nature11063`

Marchenko, S. V., Lean, J. L., & DeLand, M. T. 2022, ApJ, 936, 158, doi: `10.3847/1538-4357/ac8a98`

Mason, J. P., Werth, A., West, C. G., et al. 2023, ApJ, 948, 71, doi: `10.3847/1538-4357/accc89`

Masuda, S., Kosugi, T., Hara, H., Tsuneta, S., & Ogawara, Y. 1994, Nature, 371, 495, doi: `10.1038/371495a0`

Mathew, S. K., Lagg, A., Solanki, S. K., et al. 2003, A&A, 410, 695, doi: `10.1051/0004-6361:20031282`

Mathioudakis, M., Bloomfield, D. S., Jess, D. B., Dhillon, V. S., & Marsh, T. R. 2006, A&A, 456, 323, doi: `10.1051/0004-6361:20054752`

Mathioudakis, M., Seiradakis, J. H., Williams, D. R., et al. 2003, A&A, 403, 1101, doi: `10.1051/0004-6361:20030394`

McIntosh, P. S., & Donnelly, R. F. 1972, , 23, 444, doi: `10.1007/BF00148107`

McQuillan, A., Mazeh, T., & Aigrain, S. 2014, ApJS, 211, 24, doi: `10.1088/0067-0049/211/2/24`

Mittag, M., Hempelmann, A., Schmitt, J. H. M. M., et al. 2017a, A&A, 607, A87, doi: `10.1051/0004-6361/201630262`

Mittag, M., Robrade, J., Schmitt, J. H. M. M., et al. 2017b, A&A, 600, A119, doi: `10.1051/0004-6361/201629156`

Mittag, M., Schmitt, J. H. M. M., Hempelmann, A., & Schröder, K. P. 2019a, A&A, 621, A136, doi: `10.1051/0004-6361/201834319`

Mittag, M., Schmitt, J. H. M. M., Metcalfe, T. S., Hempelmann, A., & Schröder, K. P. 2019b, A&A, 628, A107, doi: `10.1051/0004-6361/201935654`

Bibliography

Mittag, M., Schmitt, J. H. M. M., & Schröder, K. P. 2023, A&A, 674, A116, doi: 10.1051/0004-6361/202245060

Montet, B. T., Tovar, G., & Foreman-Mackey, D. 2017, ApJ, 851, 116, doi: 10.3847/1538-4357/aa9e00

Nakariakov, V. M., Ofman, L., Deluca, E. E., Roberts, B., & Davila, J. M. 1999, Science, 285, 862, doi: 10.1126/science.285.5429.862

Namekata, K., Sakaue, T., Watanabe, K., et al. 2017, ApJ, 851, 91, doi: 10.3847/1538-4357/aa9b34

Neidig, D. F. 1989, , 121, 261, doi: 10.1007/BF00161699

Neidig, D. F., & Cliver, E. W. 1983, , 88, 275, doi: 10.1007/BF00196192

Nielsen, M. B., Gizon, L., Schunker, H., & Karoff, C. 2013, A&A, 557, L10, doi: 10.1051/0004-6361/201321912

Nogami, D., Notsu, Y., Honda, S. Maehara, H., et al. 2014, Publ. Astron. Soc. Jap., 66, L4, doi: 10.1093/pasj/psu012

Notsu, Y., Maehara, H., Shibayama, T., et al. 2016, in 19th Cambridge Workshop on Cool Stars, Stellar Systems, and the Sun (CS19), Cambridge Workshop on Cool Stars, Stellar Systems, and the Sun, 119, doi: 10.5281/zenodo.59138

Notsu, Y., Shibayama, T., Maehara, H., et al. 2013, ApJ, 771, 127, doi: 10.1088/0004-637X/771/2/127

Notsu, Y., Maehara, H., Honda, S., et al. 2019, ApJ, 876, 58, doi: 10.3847/1538-4357/ab14e6

Noyes, R. W., Hartmann, L. W., Baliunas, S. L., Duncan, D. K., & Vaughan, A. H. 1984a, ApJ, 279, 763, doi: 10.1086/161945

Noyes, R. W., Weiss, N. O., & Vaughan, A. H. 1984b, ApJ, 287, 769, doi: 10.1086/162735

Ofman, L., Averbuch, A., Shliselberg, A., et al. 2022, New Astronomy, 91, 101693, doi: 10.1016/j.newast.2021.101693

Okamoto, S., Notsu, Y., Maehara, H., et al. 2021, ApJ, 906, 72, doi: 10.3847/1538-4357/abc8f5

Oláh, K., & Strassmeier, K. G. 2002, Astronomische Nachrichten, 323, 361, doi: 10.1002/1521-3994(200208)323:3/4<361::AID-ASNA361>3.0.CO;2-1

Olspert, N., Lehtinen, J. J., Käpylä, M. J., Pelt, J., & Grigorievskiy, A. 2018, A&A, 619, A6, doi: 10.1051/0004-6361/201732525

Pallé, E. 2010, in JENAM 2010, Joint European and National Astronomy Meeting, 63

Bibliography

Parker, E. N. 1955, ApJ, 122, 293, doi: `10.1086/146087`

Pedersen, M. G., Antoci, V., Korhonen, H., et al. 2017, MNRAS, 466, 3060, doi: `10.1093/mnras/stw3226`

Petrovay, K., & van Driel-Gesztelyi, L. 1997, , 176, 249, doi: `10.1023/A:1004988123265`

Petschek, H. E. 1964, in NASA Special Publication, Vol. 50, 425

Pettersen, B. R. 1989, , 121, 299, doi: `10.1007/BF00161702`

Pevtsov, A. A., Fisher, G. H., Acton, L. W., et al. 2003, ApJ, 598, 1387, doi: `10.1086/378944`

Pitkin, M., Williams, D., Fletcher, L., & Grant, S. D. T. 2014, MNRAS, 445, 2268, doi: `10.1093/mnras/stu1889`

Reep, J. W., & Knizhnik, K. J. 2019, ApJ, 874, 157, doi: `10.3847/1538-4357/ab0ae7`

Reinhold, T., Cameron, R. H., & Gizon, L. 2017, A&A, 603, A52, doi: `10.1051/0004-6361/201730599`

Reinhold, T., & Gizon, L. 2015, A&A, 583, A65, doi: `10.1051/0004-6361/201526216`

Reinhold, T., Shapiro, A. I., Solanki, S. K., et al. 2020, Science, 368, 518, doi: `10.1126/science.aay3821`

Ricker, G. R. 2015, in AAS/Division for Extreme Solar Systems Abstracts, Vol. 47, AAS/Division for Extreme Solar Systems Abstracts, 503.01

Rieger, E., Share, G. H., Forrest, D. J., et al. 1984, Nature, 312, 623, doi: `10.1038/312623a0`

Robinson, R. D., Linsky, J. L., Woodgate, B., Carkner, L., & Timothy, G. 1998, in American Astronomical Society Meeting Abstracts, Vol. 193, American Astronomical Society Meeting Abstracts, 99.06

Russell, H. 1914, Popular Astronomy, 22, 275

Salaris, M., & Cassisi, S. 2005, Evolution of Stars and Stellar Populations

Salpeter, E. E. 1952, ApJ, 116, 649, doi: `10.1086/145656`

Santos, A. R. G., Breton, S. N., Mathur, S., & García, R. A. 2021, ApJS, 255, 17, doi: `10.3847/1538-4365/ac033f`

Santos, A. R. G., García, R. A., Mathur, S., et al. 2019, ApJS, 244, 21, doi: `10.3847/1538-4365/ab3b56`

Schaefer, B. E., King, J. R., & Deliyannis, C. P. 2000, ApJ, 529, 1026, doi: `10.1086/308325`

Schlichenmaier, R., Rezaei, R., Bello González, N., & Waldmann, T. A. 2010, A&A, 512, L1, doi: `10.1051/0004-6361/201014112`

Schmidt, S. J., Shappee, B. J., Gagné, J., et al. 2016, ApJL, 828, L22, doi: `10.3847/2041-8205/828/2/L22`

Schmitt, D. 1987, A&A, 174, 281

Schulte in den Bäumen, H., Moran, D., Lenzen, M., Cairns, I., & Steenge, A. 2014, Natural Hazards and Earth System Sciences, 14, 2749, doi: `10.5194/nhess-14-2749-2014`

Schüssler, M., & Solanki, S. 1992, Astronomy and Astrophysics, 264, L13

Schwabe, H. 1844, Astronomische Nachrichten, 21, 233

Scoggins, M. T., Davenport, J. R. A., & Covey, K. R. 2019, Research Notes of the AAS, 3, 137, doi: `10.3847/2515-5172/ab45a0`

Scullion, E., Popescu, M. D., Banerjee, D., Doyle, J. G., & Erdélyi, R. 2009, ApJ, 704, 1385, doi: `10.1088/0004-637X/704/2/1385`

Severino, G. 2017, The structure and evolution of the Sun (Springer Cham), doi: `10.1007/978-3-319-64961-0`

Shepherd, S. J., Zharkov, S. I., & Zharkova, V. V. 2014, ApJ, 795, 46, doi: `10.1088/0004-637X/795/1/46`

Shibata, K., & Magara, T. 2011, Living Reviews in Solar Physics, 8, 6, doi: `10.12942/lrsp-2011-6`

Shibata, K., Masuda, S., Shimojo, M., et al. 1995, The Astrophysical Journal, 451, doi: `10.1086/309688`

Shibata, K., & Yokoyama, T. 2002, ApJ, 577, 422, doi: `10.1086/342141`

Shibata, K., Isobe, H., Hillier, A., et al. 2013, PASJ, 65, 49, doi: `10.1093/pasj/65.3.49`

Shibayama, T., Maehara, H., Notsu, S., et al. 2013, The Astrophysical Journal Supplement Series, 209, 5, doi: `10.1088/0067-0049/209/1/5`

Shimizu, T. 1995, PASJ, 47, 251

Song, Y. L., Tian, H., Zhang, M., & Ding, M. D. 2018, A&A, 613, A69, doi: `10.1051/0004-6361/201731817`

Stix, M. 1976, in Basic Mechanisms of Solar Activity, ed. V. Bumba & J. Kleczek, Vol. 71, 367

Bibliography

Stix, M. 1981, , 74, 79, doi: 10.1007/BF00151277

—. 2002, The sun: an introduction (Springer Science & Business Media)

Sturrock, P. A. 1966, Nature, 211, 695, doi: 10.1038/211695a0

Sweet, P. A. 1958, in Electromagnetic Phenomena in Cosmical Physics, ed. B. Lehnert, Vol. 6, 123

Thompson, S. E., Fraquelli, D., Van Cleve, J. E., & Caldwell, D. A. 2016, Kepler Archive Manual, Kepler Science Document KDMC-10008-006, id. 9. Edited by Faith Abney, Dwight Sanderfer, Michael R. Haas, and Steve B. Howell

Tobias, S. 2005, Fluid dynamics and dynamos in astrophysics and geophysics, 1, 193

Torres, G., Andersen, J., & Giménez, A. 2010, The Astronomy and Astrophysics Review, 18, 67

Tsurutani, B. T., & Lakhina, G. S. 2014, Geophysical Research Letters, 41, 287

Tu, Z.-L., Yang, M., Zhang, Z. J., & Wang, F. Y. 2020, ApJ, 890, 46, doi: 10.3847/1538-4357/ab6606

Van Cleve, J., & Caldwell, D. 2009, Kepler Instrument Handbook (KSCI-19033-001), Tech. rep., KSCI-19033-001. pdf

Van Doorsselaere, T., Shariati, H., & Debosscher, J. 2017, ApJS, 232, 26, doi: 10.3847/1538-4365/aa8f9a

VanderPlas, J. T. 2018, ApJS, 236, 16, doi: 10.3847/1538-4365/aab766

Vasilyev, V., Reinhold, T., Shapiro, A. I., et al. 2022, A&A, 668, A167, doi: 10.1051/0004-6361/202244422

Vaughan, A. H., & Preston, G. W. 1980, PASP, 92, 385, doi: 10.1086/130683

Vaughan, A. H., Preston, G. W., & Wilson, O. C. 1978, PASP, 90, 267, doi: 10.1086/130324

Vida, K., Kriskovics, L., & Oláh, K. 2013, Astronomische Nachrichten, 334, 972, doi: 10.1002/asna.201211973

Vida, K., Oláh, K., & Szabó, R. 2014, MNRAS, 441, 2744, doi: 10.1093/mnras/stu760

Vida, K., & Roettenbacher, R. M. 2018, A&A, 616, A163, doi: 10.1051/0004-6361/201833194

Waldmeier, M. 1961, The sunspot-activity in the years 1610-1960 (Zurich: Schulthess)

Walkowicz, L. M., Basri, G., Batalha, N., et al. 2011, AJ, 141, 50, doi: 10.1088/0004-6256/141/2/50

Bibliography

Watanabe, K., Shimizu, T., Masuda, S., Ichimoto, K., & Ohno, M. 2013, ApJ, 776, 123, doi: `10.1088/0004-637X/776/2/123`

Wilson, O. C. 1978, ApJ, 226, 379, doi: `10.1086/156618`

Worden, S. 1983, Byrne PB, Rodono M.(Holland: D. Reidel Publ. Co.), 207

Wu, C.-J., Ip, W.-H., & Huang, L.-C. 2015, ApJ, 798, 92, doi: `10.1088/0004-637X/798/2/92`

Wu, Y., Chen, H., Tian, H., et al. 2022, ApJ, 928, 180, doi: `10.3847/1538-4357/ac5897`

Yamada, M., Kulsrud, R., & Ji, H. 2010, Reviews of Modern Physics, 82, 603, doi: `10.1103/RevModPhys.82.603`

Yang, H., & Liu, J. 2019a, ApJS, 241, 29, doi: `10.3847/1538-4365/ab0d28`

—. 2019b, VizieR Online Data Catalog, J/ApJS/241/29

Yang, H., Liu, J., Gao, Q., et al. 2017, The Astrophysical Journal, 849, 36

Yang, Z., Zhang, L., Meng, G., et al. 2023, A&A, 669, A15, doi: `10.1051/0004-6361/202142710`